SYNTHESIS AND CHARACTERIZATION OF NANOPOROUS SILICON DIOXIDE PARTICULATE FOR LOW DEFECTIVITY IN LOW-K DIELECTRIC CHEMICAL MECHANICAL POLISHING

By

KYO-SE CHOI

A DISSERTATION PRESENTED TO THE GRADUATE SCHOOL
OF THE UNIVERSITY OF FLORIDA IN PARTIAL FULFILLMENT
OF THE REQUIREMENTS FOR THE DEGREE OF
DOCTOR OF PHILOSOPHY

UNIVERSITY OF FLORIDA

2002

This work is dedicated to my family

ACKNOWLEDGMENTS

I would like to express my sincere thanks to my advisor, Dr. Rajiv K. Singh, for his guidance, trust, and encouragement during the course of the study. Without his guidance I would be still floundering to find the way; without his trust and encouragement I could not obtain the maximum freedom a student could get to indulge myself in what interests me. I am also grateful to Dr. Hassan El-Shall, Dr. Stephen J. Pearton, Dr. Abbas A. Zaman and Dr. Dinesh O. Shah for serving as committee members and supervising my study.

I would like to acknowledge Dr. Robert Vacassy, who gave me tremendous help and shared his valuable knowledge with me during my studies and research. I would also like to thank Dr. Kevin Powers and all faculty members of the Engineering Research Center for Particle Science and Technology, who were of great help in teaching me to use several ERC instruments, and also at troubleshooting various problems along the way.

I would also like to acknowledge Dr. T. S. Sudarshan, Mr. Raja Raman, Mr. Sang-Hyun Yoo and many of the staffs of Material Modification Incorporation for tremendous help and practical training for the particle synthesis and characterization during my internship.

It is always a pleasure to mention the people in our group with whom I shared warm friendship and memorable life. Special thanks go to Dr. Valentin Cracium, Dr. Don Gilbert, Dr. Kyu-Gong Cho, Dr. Uday Mahazan, Dr. Zhan Chen, Dr. Srinivas

Pietambaram, Anu, Anupam, Hui, Frank, Joshua, Michael, Nabil, Seung-Mahn, Won-Seok, Sang-Hyun, Won-Seop, Jaeyoung, Joodong, Jeremiah, and secretary Margaret.

Financial support of this work by the National Science Foundation is greatly appreciated.

Finally, I wish to convey my sincere gratitude to my parents for encouraging me to pursue graduate study overseas. I would also like to express my deepest appreciation to Sug and Dyne, whose love and encouragement have enabled me to achieve all my accomplishments in life.

TABLE OF CONTENTS

Page

ACKNOWLEDGMENTS iii

LIST OF TABLES vii

LIST OF FIGURES viii

ABSTRACT xv

CHAPTER

1 INTRODUCTION 1

2 LITERATURE REVIEW 5

Chemical Mechanical Polishing 5
Problems of Low-k Dielectric CMP 6
Slurry Stability 8
Hydrolysis Reaction 10
Advantages of Nanoporous Silica 15
CMP Defects 17

3 SYNTHESIS OF NANOPOROUS SILICON DIOXIDE PARTICULATES ... 28

Introduction 28
Experimental 31
Results and Discussion 32
Summary 50

4 DETERMINATION OF HAMAKER CONSTANT OF NANOPOROUS SILICON DIOXIDE PARTICLES 73

Introduction 73
Experimental 79
Results and Discussion 80
Summary 91

5 DIRECT FORCE MEASUREMENTS 111

Introduction 111
Experimental 118
Results and Discussion 122
Summary 129

6 SURFACE CHEMISTRY OF ABRASIVE SLURRY PARTICLES AND THEIR INTERACTIONS WITH WAFER SURFACES..... 149

Introduction 149
Experimental 157
Results and Discussion 158
Summary 165

7 MECHANICAL PROPERTIES OF NANOPOROUS SILICA PARTICLES . 187

Introduction 187
Experimental 195
Results and Discussion 196
Summary 203

8 INSPECTION OF THE SURFACE DEFECTS OF CMP SUBSTRATES POLISHED IN NANOPOROUS SILICA PARTICLE BASED SLURRY. ... 225

Introduction 225
Experimental 233
Results and Discussion 235
Summary 243

9 CONCLUSIONS..... 261

APPENDIX: EFFECTS OF SURFACE POROSITY OF SILICA PARTICLE ON OXIDE COATING PROCESS..... 267

REFERENCES 273

BIOGRAPHICAL SKETCH 280

LIST OF TABLES

Table Page

2.1 Characteristics of silica particles 13

3.1 Characteristics of as-syntheiszed and calcined silica particles 37

3.2 Comparative adsorption on silica powders from BET and α_s methods 40

3.3 Characteristics of silica particles from BET and SF methods 50

4.1 Refractive index, dielectric constant, and Hamaker constant of silica particles..... 87

6.1 Zeta potentials of the slurry particles and wafers.....159

6.2 Hamaker constants of the slurry particles and wafers..... 160

8.1 Classification of CMP defects.....231

LIST OF FIGURES

Figure Page

2.1 Schematic diagram of Chemical Mechanical Polishing (CMP) process.....19

2.2 Examples of CMP of silica wafers.....20

2.3 Dielectric configuration used for low-k interconnect systems.....21

2.4 Examples of the defects of polished surfaces of scratches and particle adhesion.....22

2.5 Schematic diagram of dishing and erosion of STI CMP.....23

2.6 Examples of the dent and bump of polished surfaces.....24

2.7 Two-dimensional representation of the difference between gel and precipitate.....25

2.8 TEOS, H_2O, Synasol (95% EtOH, 5% water) ternary phase diagram at 25 °C.....26

2.9 Five types of oxide CMP defects.....27

3.1 SEM micrographs of nonporous SiO_2 nanoparticles after 24 h reaction time.....52

3.2 Evolution of the particle size and particle size distribution of nonporous silica.....53

3.3 SEM micrographs of nonporous SiO_2 nanoparticles after 4 h reaction time.....54

3.4 Particle size distribution of nonporous SiO_2 nanoparticles.....55

3.5 Effect of chemical concentration on evolution of the particle size and particle size distribution of nonporous silica particles.....56

3.6 TEM micrographs of nonporous SiO_2 nanoparticles.....57

3.7 SEM micrographs of nanoporous SiO_2 particles.....58

3.8 Evolution of the particle size and particle size distribution of nanoporous silica.....59

3.9 Particle size distribution of SiO_2 nanoparticles.....60

3.10 Conductivity evolution during the synthesis of silica nanoparticles 61

3.11 SiO_2 zeta potential evolution during the synthesis of nanoparticles 62

3.12 Total particle interaction energy of two particles of the same size.....63

3.13 Total particle interaction energy of two particles of the different size.....64

3.14 Evolution of the maximum of the total particle interaction energy 65

3.15 Schematic diagram of isotherm adsorption and desorption 66

3.16 N_2 gas isotherm adsorption and desorption of silica nanoparticles 67

3.17 Pore size of nanoporous silica particles as a function of concentration of glycerol.....68

3.18 Pore volume of nanoporous silica particles 69

3.19 Surface area of nanoporous silica particles 70

3.20 Density of nanoporous silica particles 71

3.21 Porosity of nanoporous silica particles 72

4.1 Index of refraction, dielectric constant, and Hamaker constant of 2.8% porous silica particles 93

4.2 Index of refraction, dielectric constant, and Hamaker constant of 4.6% porous silica particles 94

4.3 Index of refraction, dielectric constant, and Hamaker constant of 6.9% porous silica particles 95

4.4 Index of refraction, dielectric constant, and Hamaker constant of 13.9% porous silica particles 96

4.5 Index of refraction, dielectric constant, and Hamaker constant of 22.2% porous silica particles 97

4.6 Index of refraction, dielectric constant, and Hamaker constant of 32.3% porous silica particles 98

4.7 Index of refraction, dielectric constant, and Hamaker constant of 36.1% porous silica.....99

4.8 Index of refraction, dielectric constant, and Hamaker constant of 57.6% porous silica

particles 100

4.9 Effect of the surface porosity on index of refraction of silica nanoparticles..... 101

4.10 Effect of the surface porosity on dielectric constant of silica nanoparticles 102

4.11 Effect of the surface porosity on Hamaker constant of silica nanoparticles 103

4.12 Effect of the surface porosity on Hamaker constant of silica nanoparticles in high wavelength range..... 104

4.13 Hamaker constant of silica nanoparticles as a function of the surface porosity..... 105

4.14 van der Waals force between porous silica particle surface and TEOS..... 106

4.15 Total DLVO energy constant charge between porous silica particle surface and TEOS..... 107

4.16 Total DLVO energy constant potential between porous silica particle surface and TEOS 108

4.17 Total DLVO force constant charge between porous silica particle surface and TEOS.... 109

4.18 Total DLVO force constant potential between porous silica particle surface and TEOS..... 110

5.1 Schematic diagram of the AFM force measurement setup..... 131

5.2 Cantilever deflection-distance curves..... 132

5.3 Schematic diagram of the nanoporous silica sample for the direct force measurement in liquid cell..... 133

5.4 Micrograph of the silica particle probe of 5 μm size attached on silicon nitride tip..... 134

5.5 Silica probe-TEOS surface interaction in deionized water at pH 3..... 135

5.6 Silica probe-2.8% porous silica surface interaction 136

5.7 Silica probe-22.2% porous silica surface interaction 137

5.8 Silica probe-36.1% porous silica surface interaction 138

5.9 Silica probe-57.6% porous silica surface interaction 139

5.10 Approaching curve of silica-silica interaction....140

5.11 Retracting curve of silica-silica interaction....141

5.12 Silicon nitride probe-TEOS surface interaction in deionized water at pH 3....142

5.13 Silicon nitride probe-2.8% porous silica surface interaction....143

5.14 Silicon nitride probe-22.2% porous silica surface interaction....144

5.15 Silicon nitride probe-36.1% porous silica surface interaction....145

5.16 Silicon nitride probe-57.6% porous silica surface interaction....146

5.17: Approaching curve of silicon nitride-silica interaction....147

5.18 Retracting curve of silicon nitride-silica interaction....148

6.1 A schematic diagram of electrochemical double layer around particle surface in an applied electric field....167

6.2 A schematic diagram of the setup of Electrophoresis measurement of the particles....168

6.3 A schematic diagram of the setup of Streaming potential measurement....169

6.4 Zeta potentials of nonporous and 36.1% porous silica particles....170

6.5 Zeta potentials of silicon, TEOS and silicon nitride wafers....171

6.6 Total DLVO energy constant potential between nonporous silica particle surface and silicon wafer surface....172

6.7 The electrostatic force between nonporous silica particle surface and silicon wafer surface....173

6.8 Total DLVO energy constant potential between 57% porous silica particle surface and silicon wafer surface....174

6.9 The electrostatic force between 57% porous silica particle surface and silicon wafer surface....175

6.10 Total DLVO energy constant potential between nonporous silica particle surface and TEOS surface....176

6.11 The electrostatic force between nonporous silica particle surface and TEOS surface....177

6.12 Total DLVO energy constant potential between nanoporous silica particle surface and TEOS surface 178

6.13 The electrostatic force between nanoporous silica particle surface and TEOS surface 179

6.14 Total DLVO energy constant potential between nonporous silica particle surface and silicon nitride wafer surface 180

6.15 The electrostatic force between nonporous silica particle surface and silicon nitride wafer surface 181

6.16 Total DLVO energy constant potential between nanoporous silica particle surface and silicon nitride wafer surface 182

6.17 The electrostatic force between nanoporous silica particle surface and silicon nitride wafer surface 183

6.18 The electrostatic forces between nanoporous silica particle surface and the wafer surfaces of silicon, TEOS, and silicon nitride 184

6.19 The electrostatic forces between 57% porous silica particle surface and the wafer surfaces of silicon, TEOS, and silicon nitride 185

6.20 The comparison of the electrostatic forces between nonporous silica and 57% porous silica particles interacting with the wafer surfaces of silicon, TEOS, and silicon nitride ...186

7.1 Schematics of load – displacement curve....205

7.2 Schematics of stress-strain curves 206

7.3 SEM micrographs of polished silica nanoparticle surface embedded into cold mounting polymer materials....207

7.4 Micrographs of Berkovich indent tip....208

7.5 Plots of calibration of nanoindentation....209

7.6 Plots of load versus depth in nanoindentation of 2.8% porous silica....210

7.7 Plots of load versus depth in nanoindentation of 4.6% porous silica 211

7.8 Plots of load versus depth in nanoindentation of 6.9% porous silica 212

7.9 Plots of load versus depth in nanoindentation of 13.9% porous silica 213

7.10 Plots of load versus depth in nanoindentation of 22.2% porous silica 214

7.11 Plots of load versus depth in nanoindentation of 32.3% porous silica 215

7.12 Plots of load versus depth in nanoindentation of 36.1% porous silica 216

7.13 Plots of load versus depth in nanoindentation of 57.6% porous silica 217

7.14 Plots of load versus depth in nanoindentation measurements of silica nanoparticle with different surface porosity at load of 25 μN.....218

7.15 Plots of load versus depth in nanoindentation measurements of silica nanoparticle with different surface porosity at load of 50 μN.....219

7.16 Contact depth of indented silica particles as a function of surface porosity.....220

7.17 Contact stiffness of indented silica particles as a function of surface porosity.....221

7.18 Elastic modulus of indented silica particles as a function of surface porosity.....222

7.19 Contact area of indented silica particles as a function of surface porosity.....223

7.20 Hardness of indented silica particles as a function of surface porosity.....224

8.1 Removal rate of three wafers polished in the nonporous silica slurry 245

8.2 Removal rate of three wafers polished in the 0.5 μm nonporous silica, alumina, and silicon nitride slurries 246

8.3 Removal rate of three wafers polished in the 0.2 μm porous silica 247

8.4 Scratches of the black diamond wafer surfaces polished in the nonporous silica slurry as a function of particle size.....248

8.5 Number of scratches of the black diamond wafer surfaces polished in the nonporous silica slurry as a function of particle size.....249

8.6 Scratches of the black diamond wafer surfaces polished in the 0.5 μm nonporous (a)SiO_2, (b) Al_2O_3, and (c)Si_3N_4 slurries.....250

8.7 Number of scratches of the black diamond wafer surfaces polished in the 0.5 μm nonporous (a)SiO_2, (b) Al_2O_3, and (c)Si_3N_4 slurries 251

8.8 Scratches of the black diamond wafer surfaces polished in the 0.2 μm nonporous silica slurry as a function of porosity.....252

8.9 Number of scratches of the black diamond wafer surfaces polished in the 0.2 μm nonporous silica slurry as a function of porosity....253

8.10 The surface roughness of the silica wafer polished in the nonporous silica slurry as a function of particle size....254

8.11 RMS of the silica wafer polished in the nonporous silica slurry as a function of particle size....255

8.12 The surface roughness of the silica wafer polished in the 0.5 μm nonporous (a)SiO_2, (b) Al_2O_3, and (c)Si_3N_4 slurries....256

8.13 RMS of the silica wafer polished in the 0.5 μm nonporous (a)SiO_2, (b) Al_2O_3, and (c)Si_3N_4 slurries....257

8.14 The surface roughness of the silica wafer polished in the 0.2 μm nonporous silica slurry as a function of porosity....258

8.15 RMS of the silica wafer polished in the 0.2 μm nonporous silica slurry as a function of porosity....259

8.16 The residual particles of the silica wafer surfaces polished in the 0.2 μm nonporous silica slurry of 5 wt.% loading at pH 3 as a function of the surface porosity of the particle: (a)2.8%, (b) 13.9%, and (c)36.1%, and (d) 57.6%....260

A.1 Zeta-potentials of 200 nm porous silica of 36% and 20 nm ceria particles and of ceria coated silica particle....269

A.2 Evolution of the coating process of ceria particles onto porous silica particle varied by the type and concentration of the precursors and pH....270

A.3 XPS of ceria coated silica particles with (a) $Ce(NO_3)_36H_2O$ system resulting in thick coated layer and (b) $Ce(SO_4)_34H_2O$ system resulting in thin coated layer....271

A.4 TEM micrographs of coated materials....272

Abstract of Dissertation Presented to the Graduate School
of the University of Florida in Partial Fulfillment of the
Requirements for the Degree of Doctor of Philosophy

SYNTHESIS AND CHARACTERIZATION OF NANOPOROUS SILICON DIOXIDE PARTICULATE FOR LOW DEFECTIVITY IN LOW-K DIELECTRIC CHEMICAL MECHANICAL POLISHING

By

Kyo-Se Choi

December 2002

Chairperson: Dr. Rajiv K. Singh
Major Department: Materials Science and Engineering

The abrasive particles in the chemical mechanical polishing (CMP) slurries play a critical role in controlling the yield of semiconductor devices. The state-of-the-art of CMP slurries typically employs hard abrasives such as alumina or silica which can lead to the significant surface defects during polishing. These surface defects during CMP are serious problems for the integration in interconnect structures. To reduce the surface defects, a new slurry design is required.

We have studied the nanoporous silica particles which are expected to reduce surface defects in low-k dielectric CMP process. By controlling the particle size and porosity, the surface properties of the particles can be suitably modified. Using these particles in the CMP slurries, we can reduce defectivity in low-k dielectric polishing. For this work, the spherical nanoporous silica particles with controlled particle size and surface porosity have been prepared by a precipitation technique and characterized in

terms of optical, electrical, and mechanical properties. We also have inspected the surface defects of wafers polished in nanoporous silica particle based slurry systems under AFM and SEM, which has proven that the nanoporous silica particles enable a reduction of the surface defects in the CMP process.

CHAPTER 1
INTRODUCTION

Chemical mechanical polishing (CMP) has now emerged as the most effective method for achieving global planarization in multilevel circuits with feature sizes less than 0.5 μm [Ste97]. The continuous effort for the miniaturization of device dimensions and increased density of devices combined with the development of new interconnect technologies such as copper and low-k dielectrics has led to the introduction and rapid development of chemical mechanical planarization technology in semiconductor manufacturing [Ste97, Rya95, Sho00, Mur00]. The success of CMP operations depends on the rate of material removal and the quality of the surface finish. Optimal removal rate and smooth surface finish are required to be achieved by the synergistic effect of the chemical and mechanical forces encountered in the CMP process.

However, as devices shrink more and more, the requirements for improved planarity and reduced defect density are becoming the stringent driver for development of the new CMP process. The surface damage of low-k dielectrics during CMP is a serious problem for low-k integration in interconnect structures. The traditional dielectric material for the interconnect circuits has been silica, which has excellent mechanical properties and can be easily integrated in semiconductor manufacturing. However, the poor mechanical adhesion and thermal properties of potential low-k dielectrics make the integration of these materials a lot more challenging [Mai01, Fur99, Mur96, Ste97].

Low-k dielectrics such as porous silica or polymers are relatively very soft and they adhere poorly. Thus, the standard abrasives used in CMP slurries such as silica or alumina can lead to significant scratching and delamination of the soft surface. These problems are expected to further amplify as the device dimensions decrease to less than 100 nm [Fur99]. Therefore, the development of new types of CMP slurries for polishing low-k dielectric materials, which can improve CMP performance with reduction of surface defects, is required.

The nanoporous silica particles are expected to have tunable mechanical properties, which are expected to reduce surface damages in low-k dielectric films. The chemical and mechanical properties of abrasive particles which are used for CMP slurries can be changed by controlling the particle size and the surface porosity. The synthesis of silica nanoporous spheres with a narrow size distribution, by varying particle size and surface porosity, can yield a wide range of aqueous silica slurries for particular CMP applications. Using these particles in the CMP slurries, the defectivity can be reduced and the nanoporous silica based slurries can lead to effective chemical mechanical polishing of low-k dielectric materials since the increased surface area may improve polishing rate and small particle sizes may reduce surface damages such as scratches and film delamination because of reduced stresses.

One aspect of this study is to develop a new slurry system based on nanoporous silica particles with well-controlled particle size and surface porosity and to characterize them in terms of optical, electrical, and mechanical properties. Chapter 3 includes the synthesis of spherical nanosized silica particles with a narrow size distribution and a variation of surface porosity, which can be prepared by a precipitation technique involving the hydrolysis reaction of a silicon alkoxide in ethanol. The effects of the

concentrations between chemical precursors and solvents and of the organic compound which presents porogen function are investigated to control the particle size and the surface porosity during synthesis process, respectively. The studies of nucleation and growth mechanism of primary particles also are included in this chapter.

It has been reported that nanosized particles have a compressed electrical double layer compared to a flat surface and thus are susceptible to adhesion with the wafer [Hie97]. To reduce the adhesion, the van der Waals attractive forces denoted by the Hamaker constant have to be decreased. The porous particle has lower density compared to the nonporous one and it is related to Hamaker constant which is a function of London dispersion force and number of atoms per unit volume in the two bodies. In chapter 4, the optical properties of nanoporous silica particles are studied. The index of refraction and dielectric constant of nonporous and nanoporous silica particles as a function of wavelength are measured using optical instruments and the Hamaker constants are calculated using Tabor-Winterton approximation. DLVO total energies and van der Waals forces between the flat substrates and nanoporous silica particles also are calculated.

In chapter 5, the interaction between a silica particle probe or silicon nitride tip and nanoporous silica particles embedded flat surfaces is studied in detail with the atomic force microscope (AFM). The direct force measurements reveal that the van der Waals force decreases with increasing the surface porosity of silica particles and the repulsive force between silica surfaces is much stronger than that between silica surface and silicon nitride surface. This is agreed with the result of the calculations of Hamaker constants and van der Waals force studied in chapter 4.

The zeta-potentials of silica particles and wafer surfaces as a function of pH using the

electrophoresis method are measured in chapter 6. The interaction force between silica particles and flat wafer surfaces is calculated with Overbeek's approximation. This result may confirm that the nanoporous silica particles lead to a very weak van der Waals attraction force to the wafer surfaces compared to a nonporous one, especially at higher pH ranges.

The large difference in the hardness of slurry abrasive and wafer could accentuate the specific types of the surface defects such as dishing, impregnation, dent and bump depending on CMP conditions. Chapter 7 presents the mechanical properties of nanoporous silica particles, as measured by the nanoindentation technique. The hardness and elastic modulus of nanoporous silica particles as a function of the surface porosity are presented in detail.

The other aspect of this study is the inspection of defects of wafer surfaces polished in nanoporous silica particle based slurry system. Successful yield management of CMP requires detection of all critical defects. Chapter 8 deals with the detection of the surface defects of polished wafers in terms of defect type. This work reveals that the nanoporous silica particle based slurry results in lower defectivity in low-k dielectric CMP processes.

Chapter 9 gives a summary of the whole study. An appendix in which the effect of the surface porosity of silica particle on coating of oxide particles is included.

CHAPTER 2
LITERATURE REVIEW

Chemical Mechanical Polishing

The process of CMP of thin films is a manufacturing step that forms a critical component in the development of numerous advanced technologies including very large scale integrated (VLSI) circuits, flat panel display technologies and ultra-high precision machining. The objective of the CMP process is to rapidly remove the top surface layer, while at the same time planarizing the surface over large length scales. Other specific characteristics of the CMP process include its polish selectivity and surface defectivity which is characterized by the number of microscratches, adhering particles and roughness of the surface [Mai01]. CMP incorporates the use of chemical and mechanical forces to planarize surfaces of wafer after etching or deposition to remove any unwanted material from the wafer surface. It is highly dependent on chemical slurries, platen and pad rotation, and the downforce that is applied to the polishing pad [Bie99]. If the mixture of downforce, rotation speed, and chemical slurry quality is not correct, wafer defects may result. The slurry, typically containing chemicals and submicron sized abrasive particles, is fed into the CMP machine, which subjects the wafer to a specific downforce and angular velocity. Every material to be polished has its own specific chemistry such as type of abrasive and chemicals to achieve optimized characteristics [Pal00].

Figure 2.1 shows a schematic diagram of chemical mechanical polishing (CMP)

process. In a typical CMP process, a wafer is pressed and rotated against a polishing pad, which also rotates eccentrically. Slurry is supplied into the gap between the wafer and the pad. The chemical and mechanical action of the slurry changes the surface topography of the wafer achieving planarization as shown in Figure 2.2. Abrasive particles in the slurry cause mechanical change on the sample surface, loosening the material for enhanced chemical attack or fracturing off the pieces of surface into the slurry, where they dissolve or are swept away. The process is tailored to provide enhanced material removal rate from high points on surfaces, thus affecting planarization. CMP is the combination of mechanical action from the force applied by the abrasive particles and chemical action from the chemical reagents in the slurry. The combination of chemical and mechanical effects is essential because chemistry alone cannot provide planarization due to the isotropic nature of chemical forces. Also, mechanical grinding alone is not desirable because of the extensive damage to the material surface.

Problems of Low-k Dielectric CMP

Figure 2.3 shows the dielectric configuration used for low-k interconnect systems. The need for interlayer dielectric (ILD) materials arises from the high dielectric constant, k, of SiO_2. Lower-k values are sought to reduce the capacitive component of the RC delay in interconnects. Several materials are under consideration, including doped SiO_2, spin-on glasses, polymers and sol-gel materials (xerogels/aerogels). The main issues with these materials are their mechanical properties, moisture intake, adhesion to the underlying layer and long-term reliability [Mur96]. Thus, the planarization of potential low-k dielectrics represents the greatest challenge to the CMP industries.

Low-k materials are typically much softer than traditional silica based dielectrics being presently used in the interconnect CMP technology. The traditional abrasives used

in the CMP of low-k dielectrics are fumed and colloidal silica. It has been known that silica based slurries have a typical pH that ranges between 10 and 12 and is used for oxide CMP application, which tends to be more of a mechanical process due to the method of planarizing the wafer surface [Cop00]. However, since silica is harder than the dielectric materials, it tends to scratch the surfaces. For example, the microhardness of copper is about 80 kg/mm^2 (Mohs scale 2.5), which is much less than silica (1200 kg/mm^2, Mohs scale 6-7) or alumina (2000 kg/mm^2, Mohs scale 9). Thus, the CMP of soft surfaces using silica and alumina based slurries results in a high degree of surface scratches on the metal or dielectric film. Figure 2.4(a) shows an example of the surface scratch of wafer polished. Pits and craters may also be observed on the soft film surface [Bro81].

Maier reported a different type of the surface defect, which can be caused by conventional slurries in the low-k CMP. The large differences in the hardness of the metal and the slurry abrasive could accentuate a special type of defect known as dishing [Mai01]. The formation of the trough shaped dish has been attributed to the low hardness of the soft media and the distortion of the pad. Besides pad parameters, the dishing effect has been found to increase using particles of high hardness such as alumina and silica in the slurries. This dishing effect is characterized by higher polishing rates in the softer media when located beside a harder media such as silica [Hur99]. Figure 2.5 represents a schematic diagram of the dishing and erosion.

It was also reported that the hard particles used in conventional slurries could dent and impregnate into the soft surface leading to additional bumps on the polished surface as shown in Figure 2.6 [Bou98, Hie97]. Bourgeat suggested that one method to reduce the mechanical effects of the particles is to reduce its size to nanometric dimension [Bou98]. The presence of large particles in the polishing slurry that contact the wafer

during polishing has been determined to cause defects in the wafers. However, the surface defects during CMP are reduced as the size of the particle decreases [Hie97]. Typically the particle size of the slurry particles used in the CMP process is less than 300 nm. Thus, the particles used in the CMP slurry usually having a mean particle size of less than 300 nm is too small to cause the scratches observed on defective wafers and can be used to reduce the surface defects. However, Hiemez reported that nanosized particles have a compressed electrical double layer compared to a flat surface, and thus are susceptible to adhesion with the wafer as shown in Figure 2.4(b). To reduce the adhesion, the van der Waals attractive forces denoted by the Hamaker constant have to be decreased. For instance the electrostatic effects and the extent of the electric double layer are significantly reduced when the particle dimensions are less than 50 nm [Hie97]. The silica-based particles tend to get embedded because of the high degree of plastic deformation of the surface. Thus, smaller particles are more difficult to remove from the surface. In addition, these particles have high normal stresses, which can collapse the network of pores on the surface if porous dielectric materials are used as low-k dielectrics. This is due to the fact that directed forces are very difficult to apply when the particle size decreases.

Another problem in the CMP of low-k dielectrics is also reported by Peter [Pet98]. Normally, CMP introduces the high frictional and shear forces on the surface. The poor adhesion of low-k films leads to delamination under standard CMP conditions if the magnitude of the shear forces is higher than the adhesion forces [Pet98].

Slurry Stability

One of the most important factors in the CMP process is the slurry system based on abrasive particles. The polishing slurry provides the means by which both chemical

and mechanical action is used to remove and subsequently planarize the wafer surface [Pet98]. The chemical components which may be present include oxidizing agents, stabilizing agents, dissolution enhancing agents, corrosion inhibitors and buffering agents. It can also have detrimental effects on the particles used in the slurry [Cha87]. The mechanical component of the slurry must be present to preferentially abrade material at the asperities, or high point on the surface, thus providing the driving force for planarization.

The most critical parameter in the slurry formulation is the stability of colloidal dispersions [Esu98, Pal00, Pet98]. Esumi reported that particle settling is often caused by the shielding of surface charges on the particles which otherwise would prevent coagulation and subsequent settling [Esu98]. This slurry settling is particularly a problem in high ionic strength dispersions, where large amounts of ions serve to enhance the charge shielding and compression of the electrical double layer around the particles. However, Palla observed the stabilization of colloidal dispersion of the slurry in the mixed surfactant system. It can be explained in terms of adsorption of ionic surfactant on particle surfaces and nonionic surfactant molecules penetrating the film of the ionic surfactant due to hydrocarbon chain interactions [Pal00]. The enhanced adsorption of nonionic surfactant in this mechanism brings about steric stabilization of the slurry. He also mentioned that the use of a relatively hydrophobic nonionic surfactant in the mixture yields optimal stability, with increasing hydrophobicity originating from either an increase in the hydrocarbon chain length or a decrease in the length of the ethoxylated chain. The increased stability with hydrophobicity of nonionic surfactant suggests that the partitioning of nonionic surfactant out of aqueous solution is a more important factor than the enhanced steric stabilization brought about by increasing the length of the polymeric

polar group. On the other hand, it was mentioned that the addition of ions to a particle slurry decreases the electrostatic repulsion between the charged particles by shielding the charges [Pet98]. This decreased electrostatic repulsion, if significant enough, can bring about agglomeration of the particles.

Hydrolysis Reaction

Small particles can be formed by the hydrolysis of metal salts or metal-organic compounds. The term hydrolysis is applied to reactions in which a substance is split or decomposed by water, or to a reaction involving the splitting of water into its ions and the formation of a weak acid or base or both. In inorganic chemistry, hydrolysis is usually applied to solutions of salts and the reactions by which they are converted to new ionic species or to precipitates-oxides, hydroxides, or basic salts. The hydrolysis of salt can involve either the cation, the anion, or both [Bae76]. In aqueous solutions metal cations (and anions) are hydrolyzed:

$$M^{z+} + nH_2O \rightarrow M\left(H_2O\right)_n^{z+} \qquad 2.1$$

Due to hydrolytic reactions, aqueous solutions of hydrated metal cations are often acidic:

$$M\left(H_2O\right)_n^{z+} + H_2O \rightarrow M\left(H_2O\right)_{n-1}\left(OH\right)^{(z-1)+} + H_3O^+ \qquad 2.2$$

In this context hydrolysis thus means that the metal cations act as acids by donating protons from coordinated water molecules in the solvation shell around the cations. Metal cations of higher valency are more readily hydrolyzed, i.e., the hydrolysis equilibrium in Equation 2.2 is shifted more to the right than cations of lower valency. The hydrolysis may proceed in several steps and not necessarily stop after one step as in Equation 2.2. In many cases poly-nuclear complexes are formed during the course of

hydrolysis and such complexes are precursors of small particles, which may eventually form as a result of various condensation reactions between the precursors. A general hydrolysis reaction can be written as follows:

$$xM^{z+} + yH_2O = M_x(OH)_y^{(xz-y)+} + yH^+ \qquad 2.3$$

with the formation quotient

$$Q_{xy} = \frac{\left[M_x(OH)_y^{(xz-y)+}\right]\left[H^+\right]^y}{\left[M^{z+}\right]^x} \qquad 2.4$$

and the formation constant

$$K_{xy} = Q_{xy}\frac{g_{xy}\left(g_{H^+}\right)^y}{\left(g_{M^{z+}}\right)^x\left(a_{H_2O}\right)^y} \qquad 2.5$$

where K_{xy} equals the equilibrium constant Q_{xy} multiplied by the activity coefficients of the species in Equation 2.5 In many investigations of hydrolysis reactions and products the concentrations of metal ions have been so low that the deviation of the activity coefficient from unity can be neglected with the result that $Q_{xy} = K_{xy}$.

Hydrolysis and Condensation of Silicon Alkoxides

Sols and gels of metal oxides with very special properties can be prepared by hydrolysis and condensation of metal alkoxides according to the sol-gel method, which is a very important technique for making so-called high-tech ceramics. Monodisperse spheres of silica can be prepared by this method.

Silica sols and gels can be synthesized by hydrolysis of monomeric tetrafunctional alkoxide precursors using a base, e.g. NH_3, in the case of sols, or an acid, e.g. HCl, in the case of gels, as catalyst. Using the functional groups, the sol-gel method is generally described by the following three equations [Ott98].

$$\equiv Si - OG + H_2O \leftrightarrow \equiv Si - OH + ROH \qquad 2.6$$

$$\equiv Si - OR + HO - Si \equiv \leftrightarrow \equiv Si - O - Si \equiv + ROH \qquad 2.7$$

$$Si - OH + HO - Si \leftrightarrow \equiv Si - O - Si \equiv + H_2O \qquad 2.8$$

where R is an alkyl group, C_nH_{2n+1}. The hydrolysis reaction, Equation 2.6, substitutes hydroxyl groups, OH, for alkoxide groups, OR. Subsequent condensation reactions, comparing silanol groups, from siloxane bonds, Si-O-Si, and the byproducts, alcohol, ROH, or water, according to Equation 2.7 or 2.8, respectively. Under most conditions, condensation will begin before hydrolysis has been completed. Since water and alkoxysilanes are immiscible a co-solvent such as an alcohol is commonly used as an homogenizing substance. The alcohol, however, is not only a solvent. According to Equations 2.7 and 2.8, it can participate in the esterification and alcoholysis reactions.

In studies of the hydrolysis and condensation of silicon alkoxides, depending on the particular final product, the H_2O:Si molar ratio has been varied from less than 0.01M to 7M, and it is possible to discern some consistent trends [Coe88]. Acid-catalyzed hydrolysis at low H_2O:Si ratios yields weakly-branched polymeric sols, whereas base-catalyzed hydrolysis at high H_2O:Si ratios gives highly condensed particulate sols. Intermediate conditions produce structures between these two extremes. Monodisperse silica sols can be prepared by using a base, e.g. NH_3, as catalysis and H_2O:Si ratio of

about 50.

Precipitated Silica

Precipitated silica is a material, which at a first glance resembles silica gel in several respects. Both materials are made by wet processes and consist of agglomerated small particles of silica. As prepared, their surface is fully hydroxylated and contains about 5 silanol groups per nm^2. However, the fact that precipitated silica is made at alkaline pH, whereas silica gel is prepared at acid pH, imparts several important differences in properties between the two silica materials. Table 2.1 lists the characteristics of different types of silica particles [Ott98].

Table 2.1 Characteristics of silica particles.

Property	Fumed or Pyrogenic Silica	Precipitated Silica	Silica Gel	
			Xerogel	Aerogel
BET surface area (m^2/g)	50 - 600	30 - 800	250 - 1000	250 - 400
Average primary particle size (nm)	5 - 50	5 - 100	3 - 20	3 - 20
Size of agglomerates or aggregates	N/A	1 - 40	1 - 20	3 - 20
Density (g/cm^3)	2.2	1.9 to 2.1	2.0	2.0
Tamped volume ($cm^3/100g$)	1000 - 5000	200 - 2000	100 - 200	800 - 2000
Loss on drying (2 h at 105 °C)	2.5	3 - 7	3 - 6	3 - 5
Loss on ignition (2 h at 1000°C, %)	1 - 3	3 - 7	3 - 6	3 - 5
PH	4	5 - 9	3 - 8	2 – 5
Dibutyl phthalate adsorption ($cm^3/100g$)	250 - 300	175 - 320	100 - 350	200 – 350
Pore size distribution	N/A	very wide	narrow	narrow
Fraction of internal surface area	0	small	very high	high
Structure of aggregates and agglomerates	chain-like aggregates	moderately aggregates almost spherical particles	very strongly agglomerated particles	clearly agglomerated porous particles
Thickening effect	very pronounced	exists	definitely exists	exists

Generally, precipitated silica is made by adding an acid, usually H_2SO_4, or HCl, to a sodium silicate solution, as a rule of SiO_2:Na_2O ratio 3.3, whereas silica gel is made by adding the silicate solution to the acid. We have defined gel as structures that consist of branched chains of particles that fill the whole volume of the sol. Precipitated silica, on the other hand, consists of relatively close-packed clumps of particles. Figure 2.7 shows the difference between a gel and a precipitate.

Preparation of Monodisperse Silica Spheres

Stöber, Fink, and Bohn, called "SFB", developed a widely used method for preparing monodisperse silica spheres [Stö68]. They hydrolyzed a tetraalkylorthosilicate, e.g. tetraethylorthosilicate (TEOS), in a basic solution of water and alcohol. The reactions for hydrolysis and condensation are:

$$Si(OC_2H_5)_4 + 4H_2O \rightarrow Si(OH)_4 + C_2H_5OH \qquad 2.9$$

$$Si(OH)_4 \rightarrow SiO_2 + 2H_2O \qquad 2.10$$

The hydrolysis and condensation occur simultaneously and would like to bring attention to the fact that the stoichiometric amount of water needed for hydrolysis is four moles of water for each mole of silicon alkoxide, or two moles if the condensation goes to completion. In order to prepare silicon particles, the ratio of water to TEOS, however, is typically higher than 20:1 and pH is very high. These two factors promote condensation, which aids the formation of compact structures rather than widely-branched networks. According to SFB-method, alcohol, ammonia, and water are first mixed. The TEOS is then added and a visible-opalescence can be observed in less than ten minutes. The resulting particles are very monodisperse that is typically less than 5% of the particles

deviate by more than 8% from the average particle size. With TEOS as the silica source the largest average particle size with a narrow particle size distribution is about 0.7 mm. The width of the distribution increases and the particles become less spherical as the concentration of TEOS exceeds about 0.2 M. Stöber also studied alkoxides with smaller and large alkoxy groups than TEOS and also used mixtures of alcohols as solvents. In general, lower alcohols as solvent yielded smaller particles and faster reactions. Particles with diameters up to 2 mm can be prepared by using tetrapenthylorthosilicate, or by either adding more alkoxide after the particles have been formed, or by carrying out the reaction at low temperatures [Hsu93]. Smaller particles, with diameter 20-35 nm, of uniform size can be prepared by either various ratios of concentrations between TEOS, ammonia, and water, or well-controlled reaction time. *TEOS*, H_2O, Synasol (95% *EtOH*, 5% water) ternary phase diagram at 25 °C is shown in Figure 2.8 representing the miscibility line.

Advantages of Nanoporous Silica

In several studies, the possibility of the use of microporous silica nanoparticle (nanoporous SiO_2) with size of less than 100 nm, which the scratching effects can be minimized significantly, was discussed [Hie97, Tom97, Vac00]. The reduced scratching on low-k dielectrics can be related to the penetration depth, *d*, which is given by

$$d = \frac{3}{4}\phi\left(\frac{P}{2KE}\right)^{2/3} \qquad 2.11$$

where ϕ is the particle size, *P* corresponds to the nominal pressure and *E* is the harmonic average of the Young's modulus of the film and the particle [Tom97]. As seen from this equation, the penetration depth varies linearly with the particle size and inversely with the Young's modulus of the impacting particle. Thus, to reduce the depth of the particle

indent and resulting scratches, the particle size as well as the Young's Modulus of the particle should be reduced [Hie97]. By using nanoporous silica slurries, the scratching effects can be minimized significantly.

Tomozawa reported that typically, the nanoporous silica particle has the lower normal stress than the nonporous particle. This lower normal stress can lead to lower shear stresses in the film and at the low-k substrate interface. Thus, this is expected to significantly reduce the changes of film delamination [Tom97]. It also was found that as the hardness of the nanoporous particle is considerably less than nonporous silica, issues related to particle impregnation can be prevented. In addition, the van der Waals attraction force between two surfaces is linearly proportional to the Hamaker constant [Hie97]. As porous particles have a reduced density due to pore formation, thus its Hamaker constant is considerably reduced, which leads to reduced particle adhesion on surfaces. Furthermore, as traditional slurry formulation contains silica at alkaline pH, the replacement of silica with nanoporous silica particles will not alter the slurry chemistry [Bro81]. By modifying the surface morphology of abrasive particles and decreasing particle size, it is possible to enhance both planarization and surface finish in dielectric material CMP.

Kelsall and Tomozawa have mentioned that the use of the Stöber method ensures a monosized distribution of silica nanoporous particles [Kel98, Tom97]. Silica particle can be suitable candidate for application in CMP because silica can be directly precipitated as monodispersed spheres, their narrow size distribution being an important requirement in CMP applications. They also mentioned that the synthesis of a wide range of monodispersed nanoporous silica particles with various mean particle sizes can be helpful for the modern polishing manufacturers for producing series of polish grades

optimized to a particular application.

CMP Defects

While it is a radical departure from the typical clean technologies that make up most of the semiconductor manufacturing process, CMP using multipart abrasive slurries has become a key technique in enabling the development and production of sub-quarter-micron devices. First used primarily for polishing interlayer dielectrics and then for treating tungsten plugs, CMP is being used in additional process segments, in particular in shallow trench isolation (STI). Because CMP inevitably creates substantial amounts of surface contaminants and can introduce many defects that are major treats to final yields, the processes must be closely monitored using sophisticated wafer inspection tools. Most common CMP process applications such as ILD and STI can introduce yield limiting defects, but the type of defects produced varies from application to application.

When CMP is used for oxide polishing, a distinction is often made between premetal oxides and ILD oxides used at the back end of the line to separate the metal layers. Oxide is being polished in both applications, but the underlying structures are different, which must be taken into consideration when inspecting for defects.

Whether it is used for ILD or STI, oxide CMP can introduce several types of yield limiting defects, including residual slurry, surface voids and surface particles. Residual slurry is caused by an inadequate post CMP cleaning step, while surface voids may be caused by an embedded particle or a weak point in the oxide being ripped out or dislodged during processing. Surface particles can also result from inadequate post CMP cleaning or from airborne contaminants. Other critical oxide CMP defects that require close monitoring are microscratches and embedded particles. Microscratches are created when a small particle or other debries is caught between the polishing pad and the oxide

surface during polishing, while an embedded particle is one trapped in the oxide during metal deposition prior to CMP. Each of these defect types is illustrated in Figure 2.9.

Detecting these different types of defects can pose serious challenges for wafer inspection systems, primarily because of the film thickness variation caused by the CMP process. During CMP process optimization, film thickness-both across a wafer and between wafers- may be varied and even a well-optimized process can show film thickness variation.

There is no single method of defect review that can fully characterize every defect; each defect classification method has its own strengths. For example, SEM review is very powerful for identifying surface contamination and defects. In fact, it is an absolute requirement for the classification of defect ≤ 0.25 μm in size at which defects can be resolved using white-light technique. However, SEM review is less able to detect subsurface damage. Simple optical microscopy is very effective at finding and characterizing subsurface defects (particularly in dielectric layers) but cannot always differentiate them from surface defects, whereas neither SEM nor optical microscopy analysis can adequately quantify the depth of a subsurface defect, such as a fine razor scratch, AFM review can provide such information in detail. But even when automated, all of these methods lengthen the inspection process and thus limit throughput.

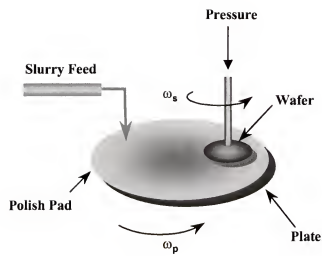

Figure 2-1 Schematic diagram of chemical mechanical polishing (CMP) process [Mah00].

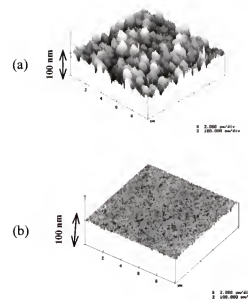

Figure 2-2 Examples of CMP of silica wafers, (a) before polishing with RMS value of 13.75 nm and (b) after polishing with RMS value of 0.88 nm [Bie99].

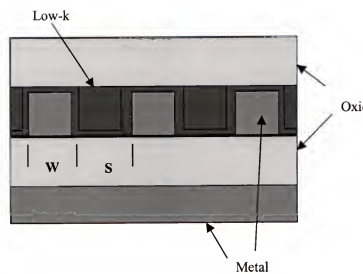

Figure 2-3 Dielectric configuration used for low-k interconnect systems [Ste97].

(a)

(b)

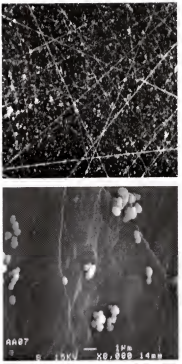

Figure 2-4 Examples of the defects of polished surfaces: (a) scratches and (b) particle adhesion [Bie99].

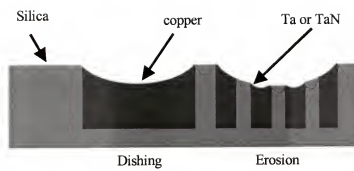

Figure 2-5 Schematic diagram of dishing and erosion [Dej96].

(a)

(b)

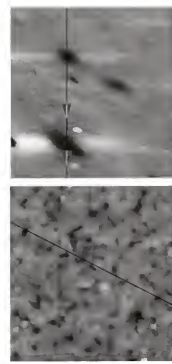

Figure 2-6 Examples of (a) dent and (b) bump of polished surfaces [Bie99].

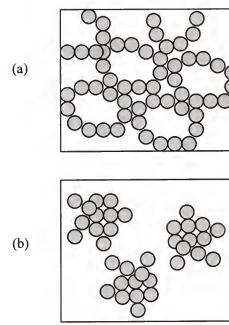

Figure 2-7 Two-dimensional representation of the difference between (a) gel and (b) precipitate [Ile65].

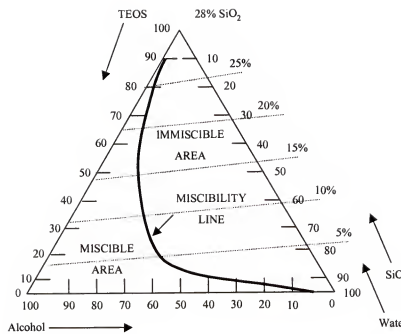

Figure 2-8 TEOS, H_2O, Synasol (95% EtOH, 5% water) ternary phase diagram at 25°C. For pure ethanol the miscibility line is shifted slightly to the right [Cog47].

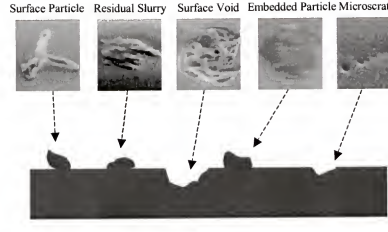

Figure 2-9 Five types of oxide CMP defects [Hea97].

CHAPTER 3
SYNTHESIS OF NANOPOROUS SILICON DIOXIDE PARTICULATES

Introduction

The hydrolysis reaction of silicon alkoxide allows the preparation of uniform non-porous silica powders of spherical morphology showing a narrow size distribution as reported in the literature [Kol56, Stö68]. The formation of uniform particles of narrow size distribution has been explained at the earlier stage by the La Mer model which involves a short nucleation time in the precipitation process [Mer50, Mer52]. After reaching a critical supersaturation by introducing reactants in the solution, the nucleation takes place, followed by particle growth via molecular addition that decreases the supersaturation level. Below the critical level, nucleation stops whereas particles continue to growth by molecular addition until an equilibrium concentration of the precipitating species is reached. This model has been the starting point for the development of many precipitation methods of particles with an uniform size. In the La Mer model, the uniformity is explained when a short nucleation period during which all the primary particles are generated is achieved [Mer52]. The growth mechanism is self-sharpening by considering the diameter growth of small particles being more rapid than the one of large particles. In the precipitation of SiO_2, the rate and extend of the hydrolysis reaction of TEOS were found to be greatly influenced by reacting conditions [Bla92, Bog91a, Fle86]. By working at a soluble silica concentration below that required for nucleation in the

presence of silica particles, particle growth was still observed indicating that the self-sharpening growth mechanism of La Mer necessary for the precipitation of uniform particles is not adequate for this system. Considering the rate of condensation faster than hydrolysis, it was found that TEOS hydrolysis was the rate limiting step. Diffusivities of reacting species were measured by Bogush and Zukoski in a kinetic study of the uniform silica particle precipitation [Bog91a]. They found that the diffusivities were too small to be attributed to molecular species, giving doubts on the validity of the growth by monomer addition. This model has been competed with the primary particle aggregation concept. Indeed, growth does not appear to be limited by diffusion of monomers to the particle surface since during the precipitation reaction, hydrolyzed TEOS concentration is independent of the presence of particles. The rate limiting step must therefore be the formation of the primary particles [Bog91b]. Nucleation can be followed by aggregation and colloidal properties of primary particles play a critical role in the development of precipitate size distributions. Thus, unless stabilized by a repulsive force substantially stronger than dispersive force, small primary particles are expected to aggregate. Nucleation proceeds throughout much of the precipitation reaction and particle growth occurs through aggregation until forming uniform precipitate where particle interaction potentials result in a suspension that is stable to irreversible Brownian aggregation. It was not accepted by Van Blaaderen [Bla92] that the rate determining step is the formation of primary particles, since using ^{13}C NMR they found that the production of hydrolyzed monomer is rate limiting, the significant induction time observed in growth experiment being due to condensation even though condensation kinetics are faster than hydrolysis [Bla92]. Bogush and Zukoski have developed an aggregative growth model in which uniformity in final particle size distribution is determined by size dependent aggregation

rates [Bog91b]. If the physical chemistry governing particle interaction potentials is such that larger particles stop aggregating with one another and grow by catching small particles, then a narrow final particle size distribution will be generated. Using the colloidal stability theory, it has been demonstrated that the formation of particles is the result of the aggregation of colloidally unstable nuclei which grow to a more stable size where aggregation no longer occurs [Fee84, Kim90]. This aggregative growth model has been confirmed for other metal oxides and metal sulfur precipitation system [Mat81, Vac98].

Tailored microporous silica nanoparticles (nanoporous SiO_2) were developed for various applications such as membrane technology or furtive materials [Bec92, Kre92]. Ordered microporous silica layers with uniform pore sizes less than 28 nm sized range were prepared by template-silicate-assemblies. The concept of this template method consists in introducing organic molecules in the bulk of silica via the polymerization of alkoxide precursor and removing it after the material is synthesized to generate the pore structure. The removal is generally made by calcination. The ordering of porous network depends directly on the micellar organization of the templating agent in the bulk. Büchel has transferred this concept to the formation of controlled microporous silica nanoparticles [Büc88]. As these porous particles were highly mechanically and thermally stable, silica slurries made of such porous silica spheres should become of great interest for CMP applications. Due to the porosity, the surface to volume ratio of the SiO_2 abrasive will be increased resulting in a more efficient contacting the wafer surface. As a result polishing rate should increase and the low stresses induced by the fine silica particles should be kept constant. The use of microporous silica nanospheres would even be much better since the increased surface area may improve cooling and small particle sizes may reduce

indentation because of reduced stresses. The purpose of the present study is to investigate the way to prepare microporous silica nanoparticles. Based on the synthesis of microporous silica nanoparticles, the effects of the porogen addition on the precipitation mechanism will be theoretically explained and discussed.

Experimental

Silica powders were prepared by precipitation in ethanol according to the Stöber method which is a precipitation technique based on a controlled hydrolysis of a silicon alkoxide (tetraethylorthosilicate, TEOS, 98%, Aldrich) in a mixture of ethanol, ammonia (21%, Aldrich) and water [Bou98, Stö68]. For each experiment, ethanol, ammonium hydroxide and water were mixed separately in a 1 liter flask. Since we were interested in fine particles, the ammonia and water concentrations were fixed at 0.2 M and 3.2 M, respectively, which nanometer-sized particles could be obtained. The TEOS concentration was fixed at 0.2 M and was added quickly to the previously prepared mixture. This system was named "standard" for investigating the effect of different ratios of concentrations between TEOS, ammonia, and water on the particle size.

On the other hand, the various concentrations of glycerol between 0.02 M and 5 M were used as a porogen to investigate the surface porosity of submicron-sized silica particles since this organic compound is known to adsorb very well to cations and oxide surfaces under basic conditions. The total alkoxide concentration was kept constant and equal to 0.2 M. The concentrations of water and ammonia were maintained at 3.2 M and 0.2 M, respectively. Glycerol was added directly to the water/ammonia/ethanol mixture prior to the addition of TEOS. The resulting solutions were shaken to ensure homogeneity. The reaction was operated during 24 hours at room temperature without stirring. As precipitated SiO_2 particles were centrifuged at 10000 rpm and washed twice with ethanol.

The cleaned particles were dried at 110 °C overnight and then calcined in air at 400 °C during 24 hours. The dried particles were easily redispersed in ethanol after an ultrasonic treatment, the resulting suspensions being used for characterizations.

Results and Discussion

Size Control of SiO_2 Nanoparticles

The precipitation of silica nanoparticles is based on the hydrolysis reaction of silicon alkoxide where the resulting particle size and morphology depend strongly on the hydrolysis kinetics. In the selected constituent concentrations, spherical, nanometer-sized silica particles could be obtained. Depending on the concentration ratios between TEOS, ammonia, and water, the particle size could be tailored from 60 to 280 nm. The silica particles were amorphous according to X-ray diffractometry. Figure 3.1 shows SEM micrographs of spherical SiO_2 nanoparticles of around 80 nm and with a narrow particle size distribution (standard deviation $s_{d_v50} = 40\%$) which was obtained for a water concentration of 3.2 M in the reacting mixture for 24 hours of reaction time. To investigate the possibility of tailoring the particle size and particle size distribution, a kinetic study regarding the particle size evolution as a function of reaction time was carried out. The particle size of silica was measured periodically during the synthesis using UPA-150 based on dynamic light scattering. The results of this experiment conducted on a reacting mixture with 3.2 M water are presented in Figure 3.2. The particle size and size distribution are evolving in the early stages of the synthesis. The mean particle size and standard deviation remain constant after 4 hour reaction indicating that no or only little particle growth occurs and that the reaction is probably over. When looking carefully at the distribution, a bimodal particle size distribution is founded with two maximums centered on 80 and 100 nm. In the early stage of the synthesis, particles

become visually detectable after 30 min. reaction, the mean particle diameter of which being 45 nm as shown in Figure 3.2. The growth mechanism occurs until 4 hour reaction time after which the colloidal dispersion stabilizes and the growth mechanism stops or progresses very slowly. Figure 3.3 presents SEM micrographs showing the silica particles at an intermediate stage of the precipitation process. When looking at the particles obtained after 4 hour reaction a larger particle size distribution is observed from the electron micrographs as compared with particles reacted for 24 hours. The coexistence of large spheres with rough surface and smaller growing particles can be observed by SEM, as it was also shown by Bogush and Zukoski [Bog88]. According to a recent work, it has been shown that the growth rate of silica particles was independent of their size, indicating that this is a surface reaction limited growth where mass transfer to the particle surface is limited by the diffusion of reactive species [Bog91b]. As a result, smaller particles are growing faster than the larger ones due to their larger surface to volume ratio yielding to uniform particle size at the end of the reaction. It was stated that water hydrolyzes TEOS to silisic acid. The condensation of these species creates oligomers forming primary particles which then agglomerates to the final silica spheres [Bog91a, Mat91]. Although the condensation step can be the cause of significant induction time before nucleation, it can be stated that most of the growth process is rate limited by the formation of hydrolyzed monomers [Bla92].

To confirm this result, the same synthesis has been carried out during 24 hour reaction time, after which particles were removed from the supernatant. The supernatant was let in a flask at room temperature for 24 hours more. As a result a suspension consisting of 80 nanometer-sized silica particles was formed from the supernatant. Figure 3.4 shows the particle size distribution of such "secondary" precipitation in comparison

with silica particles removed from the reacting mixture. In the second precipitation, the mean particle size and the particle size distribution remain similar to as-prepared silica nanoparticles indicating that the system is evolving the same way. The little difference observed can be assigned to the change in silicon alkoxide concentration in the suspension. Consequently, a change in the colloidal stability of the system is induced as well as a modification of the growing mechanism due to the decreasing formation rate of hydrolyzed monomers in the reacting mixture. Removing the particles from the reacting mixture results in a "secondary" nucleation in the system proving that silica precipitation follows a mechanism in which a permanent nucleation is occurring, the number of nuclei and the final particle size being governed by the colloidal stability of the system and a rate limiting step relative to primary particle formation.

To investigate the effect of the concentration ratios between TEOS, ammonia, and water on the particle size evolution, three more experiments were carried out based on "standard concentration" which is composed of TEOS of 0.2 M, H_2O of 3.2 M, and NH_4OH of 0.2 M. The first change of the concentration ratio was conducted by water of 6.4 M with the same concentrations of other constituents. Next changes were done by ammonia of 2.0 M and then by TEOS of 0.4 M with the same conditions of standard solution. Figure 3.5 shows the comparison of the particle size and size distribution of silica particles synthesized in different ratios of the concentrations from standard solution. Increasing the concentrations of both water and ammonia results in larger particle size, while increasing the concentration of TEOS leads to reaching the upper limit in a short time. The higher the concentrations of water and ammonia, the higher the number of OH^- ions which increase hydrolysis and nucleation rates since OH^- ion catalyze hydrolysis and condensation reactions and it has a tendency for siloxane bonds to break in highly alkaline

solution. This increase in particle size may be due to base catalyzed depolymerization which decreases the number of stable nuclei. At high concentration of TEOS, all OH^- ions are consumed resulting in smaller size of particles, which are quickly formed due to stabilization of OH^- ions. The excess of TEOS may not affect the significant change in particle size. Figure 3.6 shows TEM micrographs of nonporous silica particles with different sizes from 55 to 200 nm which were controlled by different concentration ratios between TEOS, ammonia, and water.

Effect of the Porogen on the Precipitation

Based on the Stöber method the synthesis of spherical silica particles results in dense or quasi-dense spheres. It was claimed by Jelinek and Kováts that silica particles prepared by such method are microporous, which is defined as the pore size less than 20 Å [Jel94]. This point of view will be verified and discussed in the following section (microporosity formation). To generate microporosity or more microporosity inside these spheres, molecules which can easily be removed by a simple process have to be incorporated into them during the synthesis. To ensure the microporosity formation, small organic molecules in the 0.5-2 nanometer-sized range have to be used. This processing also called "template" method has been investigated for silica nanoparticles. This template synthesis investigated is the incorporation of an organic species by adsorption during the precipitation which the organic molecule can be easily removed by calcination to create the microporosity.

The glycerol was used as the porogen and was directly introduced in the reacting mixture before the addition of TEOS. As this organic molecule is known to form strong complexes with cationic species in basic conditions, a certain incorporation of this was expected in the silica particles. The synthesis of SiO_2 particles in this system resulted in

the formation of non-agglomerated spheres. As shown in Figure 3.7, particles present a larger mean particle size of around 210 nm as compared with particles obtained under the same conditions without glycerol. The particle size distribution is still very narrow with a standard deviation, S_{d_v50}= 50%, comparable with the one of silica nanoparticles (S_{d_v50}= 40%) obtained without glycerol. Figure 3.8 shows the particle size and size distribution of silica particles during the synthesis measured periodically using UPA-150. Such as the formation of nonporous silica nanoparticles (NP-SiO_2), the evolution takes place in the early stages of the synthesis. The mean particle size and standard deviation (s) remain also constant after 4 hour reaction indicating that no or only little particle growth occurs.

In this synthesis routes, the porogen has been added at the beginning of the silica precipitation. This compound has significant effects on the precipitation mechanism. It results in a larger mean particle size of the silica particles with a narrow particle size distribution, comparable to NP-SiO_2 nanoparticles, being obtained when using glycerol. The hydrolysis of such alkoxide combined with TEOS allows the formation of oligomers different than those obtained using pure TEOS, modifying then the nuclei size and/or shape and as a result the entire nucleation step. Further agglomeration is also disturbed due to the presence of the amine function at the nucleus surface which cannot condense with other silanol functions. This results in a larger particle size distribution and also a larger mean particle size, increasingly with the porogen content. The achievement of bigger particles can be explained by change of the colloidal stability of the system due to the adsorption of glycerol at the SiO_2 surface and may be the complexing of silicon which could be also a condensation reaction of silicon ethoxide or silanol species with glycerol. As a result the particle charge at the silica surface may be completely different in this system affecting its colloidal stability and then the size. The complexing behavior or

condensation of glycerol with silicon is not yet proven but it is a possible interaction that may influence the precipitation mechanism by a destabilization of the colloidal stability of the system.

Microporosity Formation

After the synthesis of silica particles in the presence of porogen with various concentration from 0.02 to 5.0 M, microporous silica particles were obtained. The comparison of d_{BET} and the mean particle size determined from the particle size distribution presented in Table 3.1, shows that d_{BET} is always much lower except for silica nanoparticles synthesized without additive (NP-SiO_2) and for silica prepared in the presence of glycerol (P-SiO_2). This indicates that agglomeration is favored when adding glycerol. Figure 3.9 shows the effect of porogen content on the particle size of P-SiO_2 determined using UPA-150. This result presents a little higher values of the mean particle size than that of d_{BET} shown in Table 3.1.

Table 3.1 Characteristics of as-synthesized and calcined silica particles.

Treatment	Calculation	Porogen Concentration (M)				
		0	0.5	1.0	2.0	5.0
As-synthesized	S_{BET} (m^2/g)	29.1	24.3	20.7	13.4	12.9
	d_{BET} (nm)	92	116	152	214	212
	d_v50 (nm)	74	97	185	229	310
Calcined at 400 °C	S_{BET} (m^2/g)	37.4	83.2	162.6	297.7	584.5
	d_{BET} (nm)	91	73	48	35	18
	d_v50 (nm)	71	96	174	212	318

To generate the particle microporosity, the porogen part has to be removed. According to thermogravimetric measurements, a calcination at 400 °C during 10 hours is necessary for the removal of all organics in this system. Such calcination was carried out on all samples containing glycerol (P-SiO_2) and also on pure silica (NP-SiO_2). Microporosity is generated increasingly with the glycerol content. However this method

shows a major disadvantage because calcination favors particle agglomeration; the more the glycerol content, the more the agglomeration of the particles.

From this observation, it is possible that the silica particles remain similar after the heat treatment in air and that a calcination at such lower temperature may not alter very much the powder characteristics. The specific surface area of silica particles prepared in the glycerol of 5.0 M system is very high after calcination and equals to 584 m^2/g. The particles are microporous and the intraparticle microporosity, which is the main porosity contribution, can roughly be estimated at 57% if we consider the relation:

$$Porosity(\%) = \frac{V_{Tot}}{V_{Tot} + \frac{1}{d}} \qquad 3.1$$

where V_{Tot} is the total pore volume and d the silica density.

The formation of dense silica particles using the Stöber synthesis has been much debated by Jelinek and Kováts [Jel94]. Using the a_s method, where the quantity of adsorbate retained in micropores can be estimated, they found a residual microporosity, estimated up to 57 vol.%, in calcined silica spheres synthesized using the Stöber method. As a consequence, the a_s method was applied to nitrogen adsorption measurements of both as-prepared NP-SiO_2 and P-SiO_2 spheres. Since water or glycerol could fill micropores, nitrogen adsorption was carried out on calcined silica particles. As presented in Tables 1, the calcination of NP-SiO_2 induced an increase in *BET* surface area indicative of the appearance of some residual microporosity within the spheres. The a_s method

which is a linear regression on points in the relative pressure range 0.02-0.45 of the a_s isotherm gives

$$V_{ads}^{NTP} = \beta_0 + \beta_1 \alpha_s \qquad 3.2$$

where $V_{ads}{}^{NTP}$ is the quantity of N_2 adsorbed per unit adsorbent mass at normal temperature and pressure (0 °C and 1 atm). The slope, b_1, divided by $V_s{}^{NTP}$, the adsorbed quantity on unit surface area at a relative pressure of 0.4 ($V_s{}^{NTP}$= 0.414 cm^3/m^2 for hydrated silica surface) permits the calculation of S_a, the "outer surface area"

$$S_a = \frac{\beta_1}{V_s^{NTP}(0.4)} \qquad 3.3$$

The intercept of the linear regression, b_0, is a direct measure of the adsorbate retained in the micropores. An outlet surface area, S_a = 30.1 m^2/g, was found for the calcined NP-SiO_2 sample and a little amount of adsorbate blocked in the microporosity was measured (b_0 = 0.468 cm^3/g). As a result 2.7 % microporosity or ultramicroporosity (if pore sizes are lower than 20 nm or 0.5 nm, respectively) was evaluated using this method as listed in Table 3.2, which reinforces the claim established by Jelinek and Kováts. Using the a_s method for the calcined P-SiO_2 with glycerol of 5.0 M, an outlet surface area, S_a = 135.7 m^2/g, was found and the residual adsorbate quantity retained in micropores was calculated to be b_0 = 65.1 cm^3/g. A large contribution of microporosity (57%) was estimated from this method.

This results show that the glycerol method is well-adapted and suitable for

generating important intraparticle microporosity without affecting the morphology, particle size and size distribution. As a result homogeneous porous spheres are obtained which can be easily redispersed by ultrasonic treatment in water or ethanol. A slurry consisting of microporous silica particles dispersed in water containing a polyphosphate as dispersant could be prepared for chemical mechanical polishing experiments.

Table 3.2 Comparative adsorption on silica powders from BET and a_s methods.

Glycerol (M)	S_{BET} (m^2/g)	b_1 (cm^3/g)	S_o (m^2/g)	S_{BET}/S_o	b_o (cm^3/g)	*Porosity* (%)
0	15	12.4	30.1	0.49	0.468	2.76
5	584	56.1	135.7	4.31	65.1	57.57

Nucleation and Primary Particle Formation

The suggested mechanism for the formation of silica particles considers four major steps during the precipitation. The precipitation reaction starts with the hydrolysis of the alkoxide precursor followed by the formation of nuclei (oligomers). Also called nucleation, this second step results from the condensation of at least two hydrolyzed monomers and is governed by the physico-chemistry of the reacting solution. The third step of the precipitation consists of oligomer agglomeration that forms primary particles. The size and the shape of oligomers and/or primary particles depends mainly on the surface tension and viscosity of the environment but can also be influenced by the specific adsorption of molecular species such as glycerol. The primary particle formation is the main objective of this study and we have principally focused on the further agglomeration of these primary particles, also called primary agglomeration, which is the fourth step of the precipitation and results in the formation of nanometer-sized particles. At the end of the precipitation, the concentration of silisic species becomes below the critical supersaturation and nucleation stops. Under this condition, the silica particle may grow by

monomer addition to the particle surface as it was observed by several authors for systems operating at low TEOS concentration [Bla92, Jel92, Mat91].

Before starting any calculations, the measurements of the conductivity and zeta potential were carried out directly during the synthesis of pure silica (NP-SiO_2) and silica particles in the glycerol of 2.0 M system (P-SiO_2). Figures 3.10 and 3.11 show evolutions of conductivity and zeta potential of NP-SiO_2 and P-SiO_2, respectively. The baseline was adjusted to the conductivity of corresponding reacting mixture before the TEOS addition in order to subtract the signal from the solution itself. Then the alkoxide was dropped and mixed at every 10 minutes. For both studied systems, an increase in conductivity is occurring just after the addition of the alkoxide. Conductivity remains constant until 5 hours in the case of NP-SiO_2, whereas it decreases with time in P-SiO_2 system. Due to low dielectric constant of the ethanol-water mixture, ionic activities are less than unity, and ammonia is unprotonated. Since conductivity is a direct measurement of the net number of ionized species, it becomes an indicative measure of the silisic acid group deprotonation or hydrolyzed TEOS concentration. Conductivity increases can be associated with the formation of hydrolyzed TEOS and decreases in conductivity with the formation of siloxane bonds even in the glycerol system where the baseline has been adjusted for the reaction mixture containing glycerol. The conductivity in P-SiO_2 system becomes higher than for NP-SiO_2 synthesis, indicating that hydrolyzed TEOS concentration is much higher. The rapid decrease in conductivity observed in the glycerol system is a direct evidence of condensation which generates oligomer or primary particles. Because of a higher concentration of silisic species, nucleation results in the formation of much more nuclei, due to surface tension effects, which should be at the end smaller in size as compared with the system without glycerol. The decrease in conductivity may also be

interpreted as a decrease in glycerol concentration in solution due to the incorporation of these molecules into growing silica spheres. However, when looking at Figure 3.10, the high conductivity values measured after 5 hours (25 μS/cm for NP-SiO_2 and 35 μS/cm for P-SiO_2) indicates that sufficient silica is present until very late in the reaction for ensuring nucleation.

The zeta-potential evolution of the silica particles is also indicative of the behavior of the system during precipitation. After the addition of TEOS, a small increase in zeta potential is occurring followed by a significant decrease to negative values just after the first primary particles are generated. Without glycerol, the zeta potential of SiO_2 then quickly reaches a constant value of -5 mV during the synthesis as shown in Figure 3.11. Therefore, the precipitation is carried out at constant zeta potential and conductivity. On the contrary, the zeta potential of SiO_2 as well as conductivity in the presence of glycerol decrease with reaction time (from -47 to -32 mV and from 70 to 35 μS/cm, respectively). These progressive decreases, even observed after corrections due to particle density variations (glycerol incorporation), are indicative of a destabilization of the colloidal suspension formed during the synthesis. This phenomenon is probably responsible of an increased agglomeration when aging.

Colloidal Stability Calculations

To confirm the hypothesis by which the complexing behavior of glycerol could destabilize the colloidal stability of the system, some colloidal stability calculations were carried out considering an aggregation model in which the physical chemistry induces large interaction potential to large particles. The aggregation between large particles is stopped and the growth process is only due to the aggregation of small particles (primary particles) with larger one. Furthermore, this model assumes that the production of primary

particles is completely independent of the presence of the particles in the reacting system and the growth by molecular addition at the particle surface is negligible. The total pair interaction energy, V, for particles of masses, i and j, and for the center to center separation, R, is the sum of van der Waals, V_A, electrostatic, V_E, and solvation, V_S, interactions. For spherical particles of different radius, r_i and r_j, V_A can be written according to Hiemez and Rajagopalan [Hie97]

$$V_A = -\frac{A_H}{6} \times \left[\frac{2r_i r_j}{R^2 - \left(r_i + r_j\right)^2} + \frac{2r_i r_j}{R^2 - \left(r_i - r_j\right)^2} + \ln\left[\frac{R^2 - \left(r_i + r_j\right)^2}{R^2 - \left(r_i - r_j\right)^2} \right] \right] \qquad 3.4$$

where A_H is the Hamaker constant reported as 1×10^{-20} J for two silica surfaces in water [Rus91, Isr97]. The electrostatic repulsive interaction can be approximated for dense spherical particles at low ionic strength by [Hie97, Rus91]

$$V_E = 4\pi\varepsilon\varepsilon_0\psi_0^2 \left(\frac{2r_i r_j}{r_i + r_j} \right)^2 \times \frac{\exp\left[-k(R - r_i - r_j)\right]}{R} \qquad 3.5$$

where y_0 is the zeta potential measured on-line during the synthesis, k is the Debye-Hückel parameter and can be estimated as [Bog91b]

$$k^2 = \frac{\sigma}{D\varepsilon\varepsilon_0} \qquad 3.6$$

where s is the medium conductivity which is also measured on-line during the synthesis and D the average ionic diffusivity calculated to be 6.3×10^{-9} m^2/s for the ethanol/water/ammonia/silica system and at 1.4×10^{-9} m^2/s for the glycerol system [Isr97, Lev89]. Using the Derjaguin approximation, the solvation interaction for two spheres can be written as [Rus91]

$$V_s = \pi A_s l \left(\frac{2 r_i r_j}{r_i + r_j} \right) \times \exp\left(- \frac{R - r_i - r_j}{l} \right) \qquad 3.7$$

A_s is a pre-exponential factor which can be estimated at 1.5×10^{-3} J/m^2 for two silica surfaces in water and l is a decay length equal to 1×10^{-9} m for silica. For the estimation of the total pair interaction energy, V, a value of 35 was used for the dielectric constant of the water/ethanol mixture, the viscosity of water/ethanol/ammonia was taken as 1.3×10^{-3} $Pa.s$ whereas the viscosity of the solvent in the glycerol system was measured at 2.9×10^{-3} $Pa.s$ [Bog91b].

When applying the aggregative growth model to our two silica systems, some interesting behaviors can be predicted. The results of the total particle interaction energy calculations are presented in Figures 3.12 and 3.13 for both particles of the same size and particles of different sizes, respectively. Figure 3.12 shows the total particle interaction energy of two particles of the same size in NP-SiO_2 and 2.0 M glycerol systems after 24 hour reaction. It is shown that for both systems the total particle interaction energy, which is also the barrier energy against aggregation, increases with increasing particle diameter. Small primary particles with radii on the order of 0.5 nm are expected to aggregate with

particles of the same diameter. When particles or primary particles reach a critical size, which could be between 5 and 10 nm, they stop aggregating with particles of the same size because the barrier energy or colloidal stability becomes too high for the system energy which becomes not sufficient to bridge the gap. Furthermore, for a given particle size, the colloidal stability of P-SiO_2 system is much better than for NP-SiO_2 indicating that aggregation rate should be decreased when adding glycerol. However, the aggregative model shows that primary particles larger than 1 nm diameter aggregate with larger particles more rapidly than they do with themselves and larger particles aggregate slowly with particles of similar size. As a result, this provides a mechanism for the formation of a uniform particle size distribution.

Growth by Agglomeration

Continuous primary particle production and aggregation can provide a plausible mechanism for the formation of the silica particles with primary particle production or monomer hydrolysis being a rate limiting step. This indicates that even after a long reaction time, particles continue to grow. Primary particle size is expected to depend on the critical molecular weight or cross linking density where growing silica polymers become insoluble and phase separate. Increasing ionic strength can give rise to smaller primary particles. It was also shown in a recent work that at constant particle growth rates and constant rates of loss of TEOS, the final particle was altered through changes in suspending medium ionic strength [Bog91a]. Thus when adding glycerol there is a balance between the drive to precipitate smaller primary particles due to increases in k and the drive to precipitate larger primary particles due to enhanced solvent/polymer interactions as evidenced by the increase in conductivity. The primary particles of microporous silica particles precipitated in the glycerol system could be estimated at

18 *nm* from d_{BET} of the calcined powder (Table 3.1). Concerning NP-SiO_2 , the d_{BET} of the calcined powder (d_{BET} = 91 nm) is not representative of the primary particle size because in this system the aggregation leads to little amount of microporosity or ultramicroporosity. As the aggregation model predicts that the particles should be more porous, the smoothness and apparent density of such silica particles may result from molecular addition at the end of the reaction (i.e. when the silisic species concentration is below the critical nucleation concentration) and form a rearrangement and deformation of primary particles in the growing sphere as observed by Kim [Kim81]. Using the aggregative growth model, a primary particle with a diameter d_i = 18.9 *nm* could be calculated for NP-SiO_2 [Bog91a]. The difference in primary particle size for the two systems studied shows that the primary particle formation is controlled by the physical environment of the large molecular weight soluble silica.

The reactions resulting in primary particle formation proceed independently of the presence of particles and the particle size distribution is determined by particle interaction potentials. The absolute size of the final particle is determined not only by reaction rates but also by the size and colloidal stability of the primary particle. Increasing ionic strength decreases colloidal stability and decreases primary particle size as it is observed experimentally in the silica system when adding glycerol. The real situation after 24 hour reaction has been represented in Figure 3.13 for the two systems investigated considering the interaction of two silica particles of different sizes, corresponding to primary particle and final particle diameters. Applying the aggregative growth model, it is clearly shown that the potential energy barrier is much greater in the case of NP-SiO_2 as compared with the P-SiO_2 particles precipitated in the glycerol system. As a result aggregation is favored in the glycerol system due to the formation of smaller primary particles. The evolution of

the maximum of the total particle interaction energy, considering the interaction between primary and growing particles, has been calculated during the early stage of the synthesis by taking into account the changes in conductivity and zeta potential observed previously from Figures 3.10 and 3.11. The results are presented in Figure 3.14 where the potential barrier against aggregation is presented as a function of reaction time. The barrier potential remains constant all along the precipitation process in NP-SiO_2 system where no conductivity and zeta potential variations were observed. For the glycerol system, a little decrease of the barrier potential is visible even after corrections due to particle density variations. This indicates that aggregation between primary particles and larger one is more favored with increasing reaction time yielding to a destabilization of the colloidal stability of the system traduced by an increased aggregation rate. However, V_{max} may is always greater during NP-SiO_2 synthesis as compared with the glycerol system indicating that agglomeration is less favored during all the synthesis.

To predict at what size the particle will stop growing depending on the colloidal stability, further measurements have to be done to both identify the kinetic limiting step and evaluate its influence on the growing process. At the moment it is only possible to predict the tendency for which small or large particles are precipitated. During all along the precipitation process, aggregation between primary particles is proceeding. This aggregative process is self-sharpening because in a given system the diameter growth of small particles is more rapid than for larger one. The final particle size obtained in the two silica systems studied can only be a combined effect of both a rate-limiting kinetic factor and the limited aggregation rate involved by the colloidal stability of the system. The rate-limiting kinetic factor could either be monomer hydrolysis as claimed by Van Blaaderen [Bla92] or the formation of primary particles as predicted by Bogush [Bog91a].

Characterizing Pores by Adsorption Isotherms

Sing has presented an exceptionally clear and concise description of adsorption isotherms and methods for their interpretation in terms of pore size distribution. The adsorbate vapor such as nitrogen or water is adsorbed in a porous gel or powder in increasing amounts as the relative vapor pressure, P/P_0, is increased, P_0 being the saturated vapor pressure of the liquid. Figure 3.15 shows the schematic diagram of stages in adsorption of N_2 gas isotherm. Starting at zero pressure (A) a typical adsorption isotherm exhibits several stages: first, an increasing fraction of the surface is covered by adsorbed molecules (B). At a certain point around (C) the surface becomes covered with a single layer of molecules. At this stage those pores with diameters only two or three times the diameter of the adsorbate molecules will also be filled. At higher vapor pressure (D) larger pores begin to be filled. When P near P_0 (E), liquid fills all pores and gives a measure of the pore volume. At first it was thought that pore diameter could be calculated from the Kelvin equation based on the theory that liquid remains in pores even when the vapor pressure is lower than that of the massive liquid phase, since the vapor pressure of the liquid in the pores is lowered because of surface-tension effects in small capillaries. Kelvin equation relates the vapor pressure, P, at which vapor will condense in a cylinderical capillary, to radius r_k:

$$r_k = \frac{-2\sigma V \cos\theta}{RT(2.303)\log P/P_0} \qquad 3.8$$

where σ is the surface tension of liquid nitrogen at its boiling point, θ is an angle of wetting, taken as zero so that $cos\theta = 1$, V is the molar volume of liquid nitrogen, R is the gas constant, and T is the absolute temperature (77 K).

N_2 gas isotherm adsorption and desorption of silica particles with various concentrations of glycerol were conducted to obtain the pore size, cumulative pore volume, and isotherm adsorption/desorption of each silica particles synthesized. Figure 3.16 shows the isotherm adsorption and desorption of all samples synthesized in various concentrations of glycerol indicating that highly porous particles over 35% porosity can be produced in excess of 2.0 M glycerol. The pore size of each system is independent of the concentration of glycerol resulting in almost same values of less than 20 Å except for NP-SiO_2 system as shown in Figure 3.17. Figures 3.18 and 3.19 show the pore volumes and surface areas of each system determined by SF method as a function of porogen content, respectively. The pore volume and surface area of porous silica particles are proportional to the porogen content. Highly porous silica particles with the porogen content over 2.0 M resulted in very large pore volume and surface area, whereas other silica particles with the porogen content less than 2.0 M showed lower values of pore volume and surface area. Densities of nanoporous silica particles synthesized in these systems were measured by ultrapycnometer *He* gas adsorption system employing Archimedes' principle of fluid displacement and Boyle's law to determine the volume. Figure 3.20 shows the density of silica particles as a function of porogen content. As a result, highly porous silica particles showed low density value of close to 2.0, while nonporous silica revealed high value of density closed to 2.6. This result indicates that glycerol has a significant effect on the density of silica particles leading to lower Hamaker constant, which will be discussed in later chapters. The surface porosity of as-synthesized silica particles in various porogen contents was calculated based on total pore volume and density of each particle using Equation 3.1. Figure 3.21 shows the variation of the surface porosity as a function of porogen content. Table 3.3 also lists the characteristics of silica particles with variation of

the porogen content obtained from BET and SF methods in isotherm N_2 gas adsorption measurements.

Table 3.3 Characteristics of silica particles from BET and SF methods.

Porogen (M)	Pore Diameter (nm)	Pore Volume (cm^3/g)	Surface Area (m^2/g)	Density (g/cm^3)	Porosity (%)
0	18.66	0.00543	15.340	2.5807	2.76
0.02	19.34	0.00992	43.240	2.3642	4.58
0.2	18.70	0.01537	46.620	2.1814	6.48
0.5	17.68	0.03537	83.240	2.1108	13.89
1.0	17.22	0.05923	162.67	2.1074	22.18
1.5	17.20	0.09227	242.47	2.0904	32.34
2.0	17.10	0.10582	297.78	2.0846	36.14
5.0	15.93	0.20780	584.65	1.9450	57.57

In general, every particle has the surface defects including pores around 10% porosity regardless of particle shape and size. Thus, this calculation of the surface porosity indicates that to produce porous silica particles it needs to include porogen content over 0.5 M. The maximum surface porosity obtained in 5.0 M glycerol was 57%, whereas the particles synthesized in lower glycerol content showed the surface porosity less than 10%, which may be shown in any type of nonporous particle.

Summary

Spherical silica particles with a very narrow particle size distribution have been synthesized by the hydrolysis reaction of tetraethoxysilane in ethanol containing water and ammonia. The size and size distribution of silica nanoparticle were dependent of the ratio of the concentrations between water, ammonia, and TEOS. Spherical nonporous nanosized powders could be prepared with a perfect spherical morphology and a very narrow particle size distribution. The microporosity in these particles could be generated by the condensation of silanol species and the molecular adsorption of the incorporation of a porogen alkoxide. A simple calcination was sufficient to eliminate the organic porogen

and created around 60% microporosity neither altering particle morphology nor favoring silica particle agglomeration. This method was suitable for the preparation of uniform microporous silica particles with a very narrow particle size distribution and allowed the possibility of controlling the intraparticle porosity by varying the porogen content during the synthesis. Using glycerol, a larger mean particle size has been obtained as compared with silica spheres synthesized in the absence of any additive, indicating that particle growth is favored in this system. The particle formation was found to proceed via a particle aggregation process.

Using the aggregative growth model, the total particle interaction energy could be calculated showing that aggregation is favored in the presence of glycerol resulting in a larger mean particle size. The system is even destabilized when aging due to the incorporation of glycerol within particles. The final particle sizes obtained in this system were correlated to both the calculated barrier potential intensities and kinetics of the rate-limiting step (monomer hydrolysis or primary particle formation).

Following this study, we were able to tailor particle size and porosity of silica particles by playing with the chemistry of the reaction and adding chemical additives, respectively. This possible tailoring of silica particles is of great interest for CMP manufacturers since series of silica slurries for CMP may be produced and optimized depending on silica powder physical characteristics. The effect of particle size combined with porosity on glass polishing efficiency has been investigated and discussed in chapter 8.

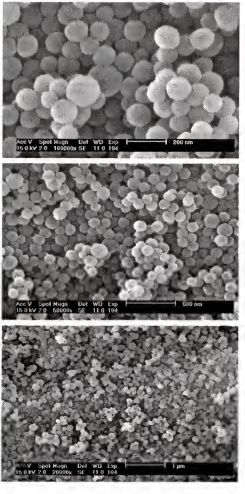

Figure 3-1 SEM micrographs of nonporous SiO_2 nanoparticles formed by the hydrolysis of TEOS in ethanol containing ammonia after 24 h reaction time.

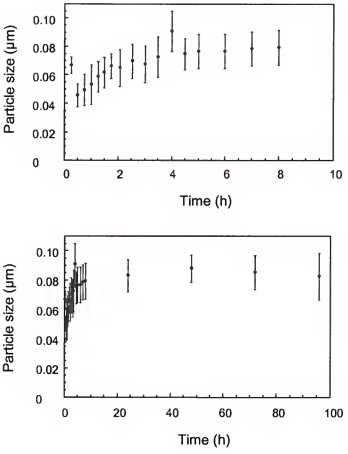

Figure 3-2 Evolution of the particle size and particle size distribution of nonporous silica during the hydrolysis precipitation of TEOS as a function of reaction time.

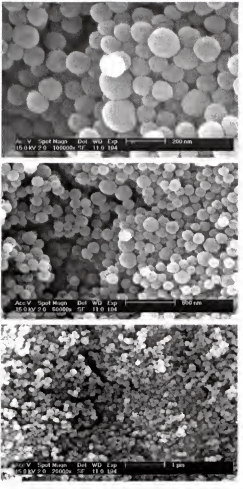

Figure 3-3 SEM micrographs of nonporous SiO_2 nanoparticles formed by the hydrolysis of TEOS in ethanol containing ammonia at an intermediate stage of the synthesis after 4 h reaction time.

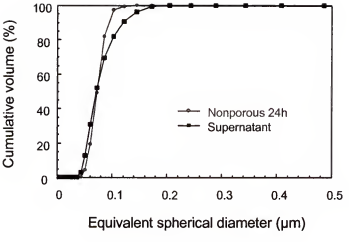

Figure 3-4 Particle size distribution of nonporous SiO_2 nanoparticles formed after 24 h reaction and in the supernatant after 24 h more. The results were determined using UPA-150.

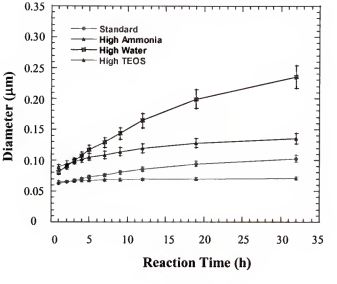

Figure 3-5 Effect of chemical concentration on evolution of the particle size and size distribution of nonporous silica particles during the hydrolysis of TEOS.

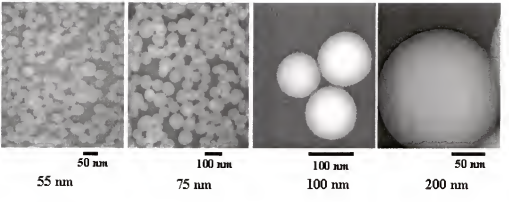

Figure 3-6 TEM micrographs of nonporous SiO_2 nanoparticles formed by the hydrolysis of TEOS in ethanol containing ammonia after 24 h reaction time. The particle size can be controlled by the ratio of combined concentrations of chemicals and by reaction time.

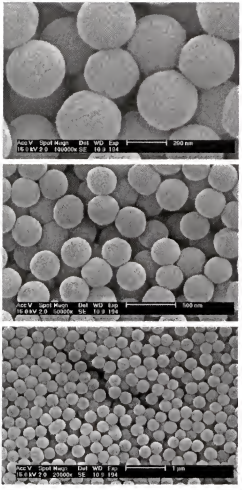

Figure 3-7 SEM micrographs of nanoporous SiO_2 particles formed by the hydrolysis of TEOS in the presence of glycerol in ethanol containing ammonia after 24 h reaction.

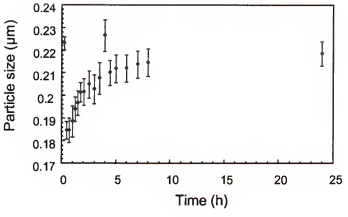

Figure 3-8 Evolution of the particle size and particle size distribution of nanoporous silica during the hydrolysis precipitation of TEOS in the presence of glycerol.

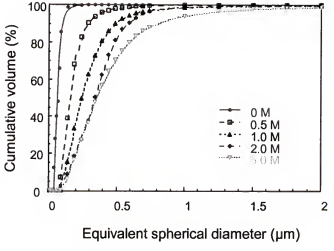

Figure 3-9 Particle size distribution of SiO_2 nanoparticles formed by the hydrolysis of TEOS at various concentration of glycerol in ethanol containing ammonia. The results were determined using the UPA 150 with a light scattering correction.

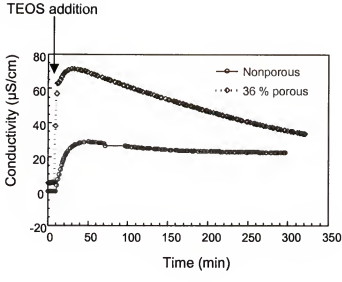

Figure 3-10 Conductivity evolution during the synthesis of silica nanoparticles formed by the hydrolysis of TEOS in the presence of glycerol or not.

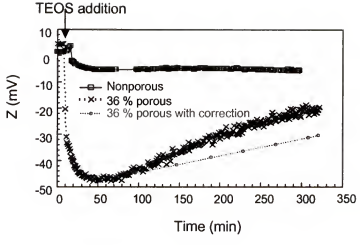

Figure 3-11 SiO_2 zeta-potential evolution during the synthesis of nanoparticles formed by the hydrolysis of TEOS in the presence of glycerol or not.The dash line presents a linear correction due to particle density variations.

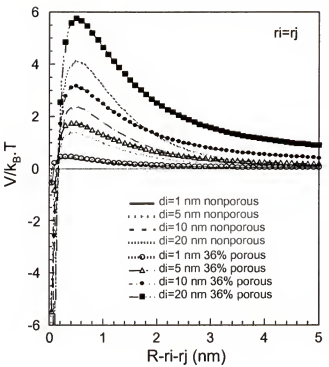

Figure 3-12 Total particle interaction energy (potential barrier) after 24 h reaction as a function of center to center separation for two particle of the same size characteristic of the precipitation condition.

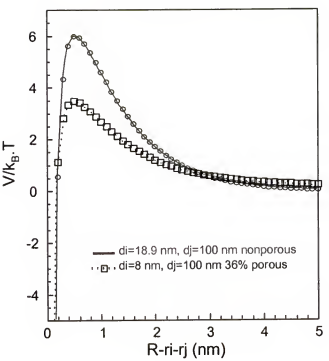

Figure 3-13 Total particle interaction energy (potential barrier) after 24 h reaction as a function of center to center separation for two particle of different size characteristic of the precipitation conditions.

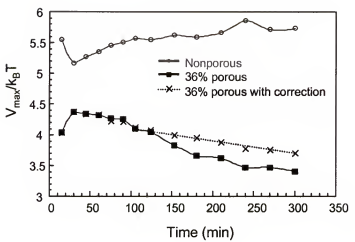

Figure 3-14 Evolution of the maximum of the total particle interaction energy (potential barrier) during the early stage of the synthesis of silica nanoparticles, considering the interaction between primary and growing particles. Dash lines present linear corrections due to particle density variations.

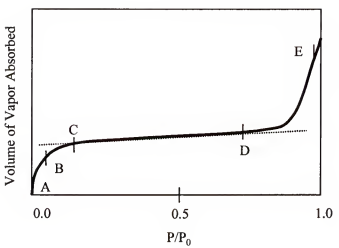

Figure 3-15 Schematic diagram of isotherm adsorption and desorption as a function of the gas pressure [Got97].

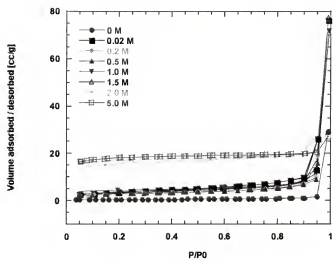

Figure 3-16 N_2 gas isotherm adsorption and desorption of silica nanoparticles in various concentration of glycerol.

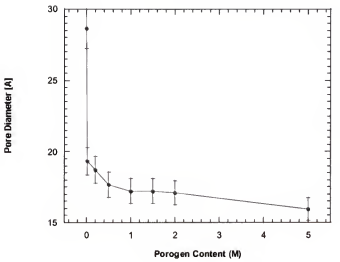

Figure 3-17 Pore size of nanoporous silica particles as a function of concentration of glycerol.

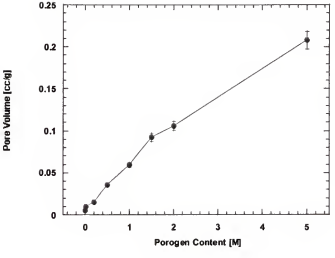

Figure 3-18 Pore volume of nanoporous silica particles as a function of concentration of glycerol.

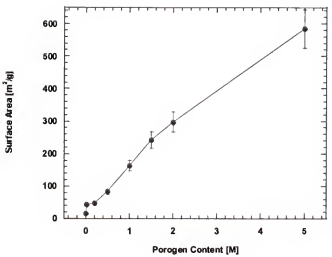

Figure 3-19 Surface area of nanoporous silica particles as a function of concentration of glycerol.

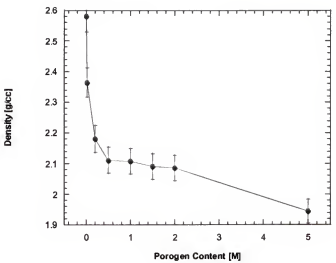

Figure 3-20 Density of nanoporous silica particles as a function of concentration of glycerol.

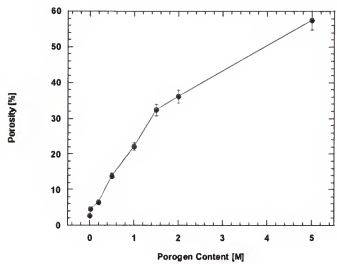

Figure 3-21 Porosity of nanoporous silica particles as a function of concentration of glycerol.

CHAPTER 4
DETERMINATION OF HAMAKER CONSTANT OF NANOPOROUS SILICON DIOXIDE PARTICLES

Introduction

Spherical microporous silica nanoparticles (nanoporous silica) with a narrow size distribution have been prepared by a precipitation technique involving the hydrolysis reaction of a silicon alkoxide in ethanol as described in chapter 3. The van der Waals force between two surfaces is linearly proportional to the Hamaker constant [Hie97]. As porous particles have a reduced density due to pore formation, thus its Hamaker constant is expected to be considerably reduced, which leads to reduced particle adhesion on the surfaces. In this chapter, the optical properties of the nanoporous silica particles with different surface porosities were measured in terms of the index of refraction and dielectric constant using ellipsometry to calculate the Hamaker constants of porous silica particles.

Index of Refraction and Dielectric Constant

The optical properties of particles are responsible for many phenomena, such as scattering, adsorption, and extinction of light [Bri67]. These interactions between particles and light are also used as the basis for measuring particle size and concentration. In describing such optical phenomena, the size parameter, α, defined by the following expression may be important:

$$\alpha = \frac{\pi D_p}{\lambda} \qquad 4.1$$

where D_p is the particle diameter and λ is the wavelength. Visible light has λ between 0.4 μm (violet) and 0.7 μm (red) [Pal85].

Another important parameter is the index of refraction, n. When light passes from an optically "thin" into an optically dense mediums, one observes that in the dense medium, the angle of refraction, β, (i.e., the angle between the refracted light beam and a line perpendicular to the surface) is smaller than the angle of incidence, α. This well-known phenomenon is used for the definition of the refractive index of a material and is called Snell's law [Pal91]:

$$\frac{\sin\alpha}{\sin\beta} = \frac{n_{med}}{n_{vac}} = n \qquad 4.2$$

Commonly, the index of refraction for vacuum, n_{vac}, is arbitrarily set to be unity. The refraction is caused by the different velocities, c, of the light in the two media:

$$\frac{\sin\alpha}{\sin\beta} = \frac{c_{vac}}{c_{med}} \qquad 4.3$$

Thus, if light passes from vacuum into a medium, we find

$$n = \frac{c_{vac}}{c_{med}} = \frac{c}{\upsilon} \qquad 4.4$$

The magnitude of n or the degree of bending will depend on the wavelength of the

light. This effect is graphically demonstrated by the familiar dispersion or separation of a beam of white light into its component colors by a glass prism. Each color is deflected by a different amount as it passes into and out of the glass, which results in the separation of the colors. Not only does the index of refraction affect the optical path of light, but also, as explained below, it influences the fraction of incident light that is reflected at the surface.

All electromagnetic radiation traverses a vacuum at the same velocity, that of light, namely, 3×10^8 m/s (186,000 miles/s) [Pal91]. This velocity, c, is related to the electric permittivity of a vacuum ε_0 and the magnetic permeability of a vacuum μ_0 through

$$c = \frac{1}{\sqrt{\varepsilon_0 \mu_0}} \qquad 4.5$$

Just as the magnitude of c, the velocity of light, v, in a medium can be expressed as

$$\upsilon = \frac{1}{\sqrt{\varepsilon \mu}} \qquad 4.6$$

where ε and μ are, respectively, the permittivity and permeability of the particular substance. From Equation above, we have

$$n = \frac{c}{\upsilon} = \frac{\sqrt{\varepsilon \mu}}{\sqrt{\varepsilon_0 \mu_0}} = \sqrt{\varepsilon_r \mu_r} \qquad 4.7$$

where ε_r and μ_r are the dielectric constant and the relative magnetic permeability, respectively. Since most substances are only slightly magnetic, $\mu_r \approx 1$, and

$$n \cong \sqrt{\varepsilon_r} \qquad 4.8$$

Measurement of the Optical Properties

The measurement of the optical properties of solids is simple in principle, but can be involved in practice. This is because many bulk solids (particularly metals) are opaque so that the measurements have to be taken in reflection. Light penetrates about 10 nm into a metal. As a consequence, the optical properties are basically measured near the surface which is susceptible to oxidation, deformation (polishing), or contamination by adsorbed layers. One tries to alleviate the associated problems by utilizing ultrahigh vacuum, vapor deposition, sputtering, etc. Needless to say, the method by which a given sample was prepared may have an effect on the numerical value of its optical properties.

The most relevant optical properties, namely, n, ε, and the energies for interband transitions can not be easily deduced by simply measuring the reflectivity, i.e., the ratio between reflected and incident intensity [Mal65]. Thus, a wide range of techniques have been developed in the past century to obtain the above-mentioned parameters. Spectroscopic ellipsometry are used for measuring the index of refraction and dielectric constant of nanoporous silica particles.

Spectroscopic Ellipsometry

This technique was developed in its original form at the turn of the century. The underlying idea is as follows: If plane polarized light impinges under an angle on a metal, the reflected light is generally elliptically polarized. The analysis of this elliptically polarized light yields two parameters, the azimuth and the phase difference from which the optical properties are calculated. We consider plane polarized light whose vibrational plane is inclined by 45° towards the plane of incidence. This angle is called azimuth, Ψ_e, in contrast to the azimuth of the reflected light Ψ_r which is defined as

$$\tan \psi_r = \frac{\xi_{Rp}}{\xi_{Rs}} \qquad 4.9$$

where ξ_{Rp} and ξ_{Rs} are parallel and perpendicular components of the reflected electric field strength, $|\xi|$, i.e., the amplitudes of the reflected light wave [Pal85].

In elliptically polarized light the length and direction of the light vector is altered periodically. The tip of the light vector moves along a continuous screw, having the direction of propagation as an axis. The projection of this screw onto x-y plane is an ellipse. Elliptically polarized light can be thought of as composed of two mutually perpendicular, plane polarized waves, having a phase difference δ between them expressed in fractions of 2π. For the actual measurement of Ψ_r and δ, one needs two polarizers consisting of a birefringent material which allows only plane polarized light to pass, and a compensator also consisting of birefringent material which allows one to measure the phase difference, δ. The light reflected from a metal is represented by two light vectors pointing in the x- and the y- directions, respectively. They have a phase difference, δ, between them. By varying the thickness of the birefringent materials in the compensator, one eventually accomplishes that the light which leaves the compensator is plane polarized (i.e, $\delta = 0$). The resulting vector, R_{res}, is then titled by an angle, Ψ_r, against the normal to the plane of incidence. One determines Ψ_r by turning the analyzer to a position at which its axis is perpendicular to R_{res}. In short, δ and Ψ_r are measured by simultaneously altering the thickness of the compensator and turning the analyzer until no light leaves the analyzers. It is evident that this method is cumbersome and time-consuming, particularly in cases in which an entire spectrum needs to be measured point

by point. Thus, in recent years automated and computerized ellipsometrys have been developed.

Hamaker Constant and van der Waals Force

Hamaker calculated the energy of the van der Waals (*vdW*) interaction between two macroscopic bodies by summing the interactions between all molecular pairs of two bodies [Ham37]. In practice this is done by an integration and the result is that the distance dependence of the *vdW* interaction between microscopic bodies is much weaker than that between molecules. The integration has the form that can be expressed as

$$F(H) = -\int_{v_1} d\tau_1 \int_{v_2} \frac{C_{12}\rho_1\rho_2}{r_{12}^6} d\tau_2 \qquad 4.10$$

Here, r_{12} is the distance between two volume elements, $d\tau_1$ and $d\tau_2$, of body 1 and 2 with volume, v_1 and v_2, respectively and ρ_1 and ρ_2 are the atom number densities in the two interacting bodies. The result for the *vdW* energy for the interaction between a sphere and a flat surface separated by a distance, H, is given by

$$F(H) = -\frac{AR}{6H} \qquad 4.11$$

where R is the radius of a sphere and A is the Hamaker constant which is defined as

$$A = \pi^2 C\rho_1\rho_2 \qquad 4.12$$

where p_1 and p_2 are the number of atoms per unit volume in the two bodies and C is the coefficient in the atom-atom pair potential [Ham37]. An advantage of this approach is that the obtained results have the general form, which can be expressed as

$$F(H) = -AG(H) \qquad 4.13$$

The Hamaker constant, A, is a material parameter and $G(H)$ is a factor that depends only on the geometry of the interacting bodies. This separation into a material portion and a geometric portion simplifies the evaluation of *vdW* interaction for different materials and different geometries.

As it is shown above, the vdW interaction can be characterized by determining the Hamaker constant, however, since Hamaker's method ignores multi-body interactions with neighboring bodies, it is very difficult to get an accurate value of the Hamaker constant when a medium separates the two interacting bodies.

An alternative approach, which was proposed by Lifshitz is to consider the muli-body interactions by treating the interacting bodies and the intervening medium as contineous phases with certain dielectric properties and viewing the vdW interaction as a result of the interference between fluctuating electromagnetic fields extending from the interacting bodies [Lif56].

Experimental

Spectroscopic ellipsometry was employed to measure the index of refraction and dielectric constant of the nanoporous silica particles. Eight samples were prepared in this experiment. Microporous silica particles of various surface porosities (2.8%, 4.6%, 6.9%, 13.9%, 22.2%, 32.2%, 36.6% , and 57.6%) synthesized by a precipitation technique involving the hydrolysis reaction of a silicon alkoxide in ethanol were dispersed in water with the same concentration of 5 wt% for all samples and then two drops of each solution were deposited onto TEOS wafer surface in size of 1 in^2. The samples were dried at room temperature for 24 hours.

The thickness of each sample was measured by ellipsometry prior to the measurements of refractive index and dielectric constant to ensure that each sample has

the almost same thickness. The index of refraction and dielectric constant of each sample were measured simultaneously as a function of wavelength ranging from 280 to 770 nm

Results and Discussion

Effect of the Surface Porosity on the Index of Refraction and Dielectric Constant

The index of refraction of silica particles, which were uniformly deposited onto TEOS wafer surface, of various surface porosities were measured using the spectroscopic ellipsometry as a function of wavelength ranging from 280 to 770 nm. Clean TEOS surface also was measured to obtain both refractive index and dielectric constant to be used as a reference data. Figures 4.1 through 4.8 show the results of this experiment. The top plot of each figure presents the index of refraction of each sample as a function of wavelength with that of TEOS. As a result, the index of refraction of nanoporous silica particles with porosity over 13.9% is decreased as increasing the surface porosity at high wavelength rages over 400 nm based on that of TEOS surface. However, most nonporous silica samples with lower surface porosity of 2.8%, 4.6%, and 6.9% do not show any different values of refractive index between their surfaces and TEOS surface in the entire ranges of wavelength resulting in almost overlapping with that of TEOS indicating that the surface porosity does not much affect the refractive index. The higher the surface porosity, the lower the value of the refractive index of highly porous silica particles. The higher the wavelength, the greater the difference of the refractive index.

In general, the refractive index is related to electronic polarization at the relatively high frequencies for visible light, thus, the electronic component may be determined from index of refraction measurements using Equation 4.8. Since the retardation of electromagnetic radiation in a medium results from electronic polarization, the size of constituent atoms or ions has a considerable influence on the magnitude of this effect.

Generally, the larger an atom or ion, the greater will be the electronic polarization, the lower the velocity, and the greater the index of refraction. For crystalline ceramics that have cubic crystal structures, and for glasses, the index of refraction is independent of crystallographic direction (i.e., it is isotropic). Noncubic crystals, on the other hand, have an anisotropic *n*; that is, the index of refraction is greatest along the directions that have the highest density of ions. Figure 4.9 shows the effect of the surface porosity of silica particles on the index of refraction as a function of wavelength indicating that all samples have the same trend of curves for this wavelength ranges applied.

On the other hand, the dielectric properties of a material are generally represented by the frequency dependent relative permittivity, also called the dielectric response function, $\varepsilon(\omega)$

$$\varepsilon(\omega) = \varepsilon'(\omega) + i\varepsilon''(\omega) \qquad 4.14$$

which is a complex function where $\varepsilon'(\omega)$, the real part is related to the transmission, and $\varepsilon''(\omega)$, the imaginary part is related to the absorption of the applied electromagnetic energy. In the frequency range where the absorption, $\varepsilon''(\omega)$, is zero, the material is transparent and the real part of the dielectric response function is directly related to the refractive index, $n(\omega)$, through

$$\varepsilon(\omega) = \varepsilon'(\omega) = n^2(\omega) \qquad 4.15$$

For a static applied field ($\omega = 0$), non-conductive materials are characterized by $\varepsilon''(\omega) = 0$, hence $\varepsilon'(0)$ is equal to $\varepsilon(0)$, which is the static dielectric constant [Gee89].

The dielectric data of a material can be measured by a number of methods including capacitance bridge, optical reflectance, ellipsometry, and electron loss spectroscopy. Most of these methods produce only one of the constituents of the complex

dielectric response function, therefore the conversion from the real to the imaginary constituent or vice versa is necessary. To do this, the Kramers-Kronig (*K-K*) relation is commonly used, which can be given by

$$\varepsilon'(\omega) = 1 + \frac{2}{\pi}\int_0^{\infty} \frac{x\varepsilon''(\omega)}{x^2 - \omega^2} dx \qquad 4.16$$

where x corresponds to the real values of the frequency. If $\varepsilon''(\omega)$ (i.e. the absorption spectrum) is known in the entire frequency range, $0 \leq \omega \leq \infty$, then $\varepsilon'(\omega)$ can be fully defined using the *K-K* relation [Ber97].

The middle of each plot of Figures 4.1 though 4.8 show the dielectric constants of nanoporous silica particles with various surface porosities as a function of wavelength. The dielectric constant is decreased with increasing the surface porosity of silica particle for all wavelength ranges compared to that of TEOS surface. Even though dielectric constant is related to the refractive index, all ranges of wavelength affect the variation of dielectric constant, whereas only high wavelength range influences the refractive index as described above. Figure 4.10 shows the different values of dielectric constant of silica particles with various surface porosities including TEOS presenting that over 20% porosity of the particles have lower values of dielectric constant.

Calculation of Hamaker Constant

The calculation of the Hamaker constant of nanoporous silica particles were conducted using Tabor-Winterton approximation between two different surface assuming in aqueous solution. In the Lifshitz theory the description of the vdW interaction energy is the same as with the Hamaker approach, however, the only difference is the way the Hamaker constant is calculated. The Hamaker constant can be calculated by the

frequency dependent bulk dielectric properties of the continuous phases.

As it is shown in Equation 4.16, the dielectric response function can be acquired from the *K-K* relation from measurements of the complex refractive indices as a function of frequency. However, since the *K-K* relation is only formally correct if the dielectric properties are known for the full frequency range, this technique is sensitive to numerical errors from approximations in unavailable parts of the spectrum.

Ninham and Parsegian demonstrated that a simpler dielectric representation could be used for the purpose of calculating the Hamaker constants by making an imaginary dielectric response function, $\varepsilon(i\xi_m)$ [Mye99]. The description of $\varepsilon(i\xi_m)$ based on the damped oscillators model with limited spectral data available can be written as

$$\varepsilon\left(i\xi_m\right) = 1 + \sum_{j=1}^{N} \frac{C_j}{1 + \left[\frac{\xi_m}{\omega_j}\right]^2} \qquad 4.17$$

with

$$C_j = \frac{2f_j}{\pi\omega_j} \qquad 4.18$$

where ω_j is the oscillator damping frequency, f_j, is the oscillator damping strength, and $i\xi_m$, the imaginary frequency is

$$\xi_m = m\frac{4\pi^2 kT}{h} \qquad 4.19$$

where k is Boltzmann's constant, T is the temperature in Kelvin, m is an integer, and h is Plank's constant. The reason for using imaginary representation is completely mathematical, the imaginary part of the frequency has no physical significance [Par69].

For the non-retarded Hamaker constant, A_{132}, can be given by

$$A_{132} = \frac{3kT}{2}\sum_{m=0}^{\infty}{}'\sum_{s=1}^{\infty}\frac{\left(\Delta_{13}\Delta_{23}\right)^{s}}{s^{3}} \qquad 4.20$$

with Δ_{13} described as

$$\Delta_{13} = \frac{\varepsilon_1\left(i\xi_m\right) - \varepsilon_3\left(i\xi_m\right)}{\varepsilon_1\left(i\xi_m\right) + \varepsilon_3\left(i\xi_m\right)} \qquad 4.21$$

and the prime in Equation 4.20 means that the $m = 0$ term should be multiplied by 0.5 and $\varepsilon_1(i\xi_m)$ is the frequency dependent dielectric response function of material 1 [Ham37].

Hough and White showed that Equation 4.17 could be more simplified for most non-conductive solid materials, because the dielectric response in the visible-ultraviolet (*UV*) range fully dominates the vdW interaction [Hou80]. The dielectric response function for most non-conductors can be written as

$$\varepsilon\left(i\xi_m\right) = 1 + \frac{C_{IR}}{1+\left(\frac{\xi_m}{\omega_{IR}}\right)^2} + \frac{C_{UV}}{1+\left(\frac{\xi_m}{\omega_{UV}}\right)^2} \qquad 4.22$$

where C_{IR} and C_{UV} are the absorption strengths in the infrared (*IR*) and *UV* regions,

respectively, and ω_{IR} and ω_{UV} are the characteristic absorption frequencies in the *IR* and *UV* regions, respectively. Hough and White demonstrated that C_{IR} and ω_{UV} can be acquired from the frequency dependence on the refractive index for materials, which do not absorb in the visible and *UV* ranges. This is done by using the so-called the Cauchy equation, which can be given by

$$n^2(\omega) - 1 = \left(n^2(\omega) - 1\right)\frac{\omega^2}{\omega_{UV}^2} + C_{UV} \qquad 4.23$$

A linear plot of $(n^2(\omega)\text{-}1)$ versus $(n^2(\omega)\text{-}1)\omega^2$ will have the slope $1/\omega^2{}_{UV}$ and cross the ordinate axis at C_{IR} can be then be calculated from the equation, which is given by

$$C_{IR} = \varepsilon(0) - C_{UV} - 1 \qquad 4.24$$

The contribution due to the dispersion interaction to the total vdW force decays rapidly as the separation distance between the two interacting bodies becomes larger than a few nm, since the time taken for the electromagnetic field to propagate is not the same as the period of the fluctuating dipole itself at the separation distance larger than a few nm.

This retardation effect should be taken into account for the interactions between macroscopic bodies, especially in a liquid medium. A simple and accurate expression of the correction factor for the retardation effect in practical applications is given by Zhang which can be written as

$$f_{retard}(D) = 1 - \frac{aD}{\lambda}\left(1 + \frac{\lambda}{4aR}\right)\ln\left(1 + \frac{\lambda}{aD}\right) \qquad 4.25$$

where a is 5.32 and λ is 100 *nm* in these calculations [Zha99].

For materials in which spectral optical properties are not available, the Tabor-Winterton approximation for the Hamaker constant provides a useful estimation based on readily available refractive indices and the static dielectric constants. Therefore, the non-retarded Hamaker constant for two macroscopic bodies 1 and 2 interacting over a medium 3, is approximately given by

$$A_{132} = \frac{3kT}{4}\left(\frac{\varepsilon_1 - \varepsilon_3}{\varepsilon_1 + \varepsilon_3}\right)\left(\frac{\varepsilon_2 - \varepsilon_3}{\varepsilon_2 + \varepsilon_3}\right) + \frac{3h\omega}{32\pi\sqrt{2}} \frac{\left(n_1^2 - n_3^2\right)\left(n_2^2 - n_3^2\right)}{\left(n_1^2 + n_3^2\right)^{1/2}\left[\left(n_1^2 + n_3^2\right)^{1/2} + \left(n_2^2 + n_3^2\right)^{1/2}\right]} \quad 4.26$$

where ε_i and n_i is the static dielectric constant and the refractive index in the visible of material 1, respectively, and ω is the characteristic absorption frequency. Typically, a characteristic absorption frequency of 3×10^{15} *Hz* is used in this approximation [Tab77].

This approximation is obtained from Equation 4.20 ignoring all summation terms $s \rangle 1$, converting the summation over m to an integral for $m \rangle 1$ and finally setting the absorption frequencies of the materials equal, $\omega_1 = \omega_2 = \omega_3 = \omega$ [Ped98].

The bottom of each plot of Figures 4.1 through 4.8 show the results of Hamaker constants of nanoporous silica particle of various surface porosities. To calculate this, the values of refractive index and dielectric constant of both nanoporous silica particle samples and TEOS were used as the surface 1 and 2, respectively, of A_{132} expressed in Equation 4.26. Medium 3 is the aqueous solution of DI water. In this case, since TEOS surface was used for the refractive index and dielectric constant of the surface 2, which is

constant as a base line, only n_1 and ε_1 of the surface 1, porous silica samples, were applied to this calculation. Figures 4.11 and Figure 4.12 show the effect of the surface porosity on Hamaker constants of nanoporous silica particles with various surface porosities as a function of wavelength. Figure 4.11 presents the results of calculated Hamaker constants in the entire range of wavelength, while Figure 4.12 shows the different scale of plots only at higher wavelength ranges over 360 nm. At low wavelength the values of the Hamaker constants of all samples increase with increasing the wavelength and then keep constant levels due to consistency of both refractive index and dielectric constant of each sample at high wavelength ranges as shown before. Figure 4.13 shows the variation of the Hamaker constant of nanoporous silica particle obtained from Equation 4.26 as a function of the surface porosity.

Table 4.1 Refractive index, dielectric constant, and Hamaker constant of silica particles.

Porosity	Refractive Index	Dielectric Constant	Hamaker Constant (10^{-20} J)
2.76	1.4696	3.8002	0.67
4.58	1.4647	3.7100	0.61
6.48	1.4635	3.5002	0.54
13.89	1.4636	3.2100	0.47
22.18	1.4631	2.6202	0.36
32.34	1.4628	2.3002	0.31
36.14	1.4628	2.0004	0.26
57.57	1.4624	1.7202	0.23

Table 4.1 also presents the refractive index and dielectric constant of each sample measured by spectroscopic ellipsometry at specific wavelength, 504.1 nm, and the result of the Hamaker constant calculated at the same wavelength. As a result, very low values of the Hamaker constants were obtained in highly porous silica particle samples. Table 3.3 shows the density of silica particles with a variation of the surface porosity, which is described in chapter 3. Since the Hamaker constant is related to the densities of two bodies, 1 and 2 in A_{132}, it is expected that the highly porous silica spheres with lower

density may have lower Hamaker constant if other conditions are the same. The result of the Hamaker constant calculated according to the surface porosity showed the same trend as expected. The higher the surface porosity of silica particle, the lower the density, and the lower the Hamaker constant.

van der Waals Forces between Nanoporous Silica and TEOS

The vdW forces are always present between atoms or between molecules, and may be attractive or repulsive [Dzy61]. Attractive vdW forces have been used to explain why neutral, chemically saturated atoms congregate to form liquids and solids. The vdW interactions are caused by a change in dipole moment arising from a shift of orbital electrons to one side of an atom or molecule, creating a similar shift in adjacent atoms or molecules. One of the interactions contributing to the overall vdW interaction is Heesom interaction-orientation effect. A permanent molecular dipole, such as H_2O molecules, creates an electric field, which has the effect of orienting other permanent dipoles so that they are attracted to the first one. Debye interaction-induction effect also contributes to vdW interaction. A permanent dipole includes a dipole in a polarizable atom, molecule, or medium, and the induced dipole is oriented such that it is attracted. These results from the intrinsic polarizability of the multiple electron clouds that constitute the interatomic bonds of the atom or molecule. Another type of interaction contributing to vdW is London interaction-distance effect. An instantaneous dipole, arising from a fluctuation in the distribution of electronic charge, induces dipoles in surrounding atoms and molecules. This dispersion contribution exists between all atoms as well as between non-polar molecules and is the most important contribution to the total vdW interaction.

As the separation distance between two interacting molecules becomes larger than a few nm, the interaction becomes retarded due to the finite speed of electromagnetic

radiation. This only affects the dispersion contribution, however, the orientation and induction energies remain non-retarded at all separation. Therefore, at relatively large separations, the dispersion contribution changes with separation distance as $1/r^7$ while the smaller static part still remains as $1/r^6$ and the overall interaction will vary as $1/r^7$as described in Equation 4.10. At very large separations, where the dispersion part is fully related, the total interaction again changes as $1/r^6$.

DLVO interaction energy and force between nanoporous silica particle surface and TEOS surface in a liquid medium were calculated using Equation 4.11. The Hamaker constant of nanoporous silica particles of various surface porosity ranges, which was calculated by Equation 4.26 using the measurements of the refractive index and dielectric constant of each sample, was applied to this calculation. Several parameters used for this calculation were fixed as a constant. Stern potential of both surface 1 and 2 was 30 mV and electrolyte concentration of 0.001 M was applied with the counter-ion valency of 4 at temperature of 293 °K. Relative dielectric constant of the medium, water, was used the value of 78.54 and particle size of 200 nm of the surface 1 was applied for all silica particle samples. Debye-Hukel parameter and Debye length of 3.3×10^7/m and 30.17 nm, respectively, were applied in this calculation, whereas Debye-Hukel parameter×radius of the surface 1 was calculated as 16.5741416. Grahame charges was used as 7.33×10^{-4} C/m^2 for both surfaces 1 and 2.

The DLVO total energy and force between spherical silica nanoparticle surface and flat TEOS surface in a aqueous medium were calculated by Equation 4.11 according to different surface porosity of silica particles. The total DLVO energy constant charge and potential between two surfaces, silica sphere and TEOS flat, as a function of separation distance, and the total DLVO force/radius constant charge and potential were obtained in

this calculation. As a result, all types of total DLVO interaction energies and forces between spherical silica particle surface and flat TEOS surface increase with increasing the surface porosity of silica particles, whereas van der Waals attraction force decreases as the surface porosity increases. As shown in Figure 4.14, the total DLVO energy constant charge between nonporous silica particle (2.8%, 4.6%, 6.9, and 13.9%) surfaces and TEOS surface starts decreasing from the separation distance of 2 nm, while that between highly porous silica particle (22.2%, 32.3%, 36.1%, and 57.6%) surface and TEOS surface starts decreasing in more closer distance around 1 nm. Figure 4.15 also shows the total DLVO energy constant potential presenting the same phenomenon as of interaction charge even though the decaying distance of interaction potential in both nonporous and porous cases was extended about 1 nm more. Figures 4.16 and 17 show the total DLVO interaction force in terms of constant charge and potential, respectively, between silica sphere surface and TEOS flat surface indicating that porous silica particle interacts more repulsively than nonporous one. The van der Waals attractive forces between silica particle surface and TEOS surface are plotted in Figure 4.18.

As a result, the higher the surface porosity of silica particles, the lower the van der Waals attractive force at short separation distance less than 20 nm. It is meant that very weak attractive or adhesion force between highly porous silica particle and TEOS wafer surface may be applied in CMP performance, which can reduce the particle adhesion and residual slurry particles during CMP. Table 4.1 shows the Hamaker constant value of spherical silica particles with a variation of the surface porosity, which is calculated with the values of the refractive index and dielectric constant using Tabor-Winterton approximation in Equation 4.26. Since van der Waals force is proportional to the Hamaker constant as described in Equation 4.11, it is expected that lower van der Waals

force is observed in highly porous silica particles more than nonporous one. This expectation is agreed with the calculation of van der Waals force and DLVO theory.

Summary

The optical properties of nanoporous silica particles were characterized in this chapter. The measurements of the refractive index and dielectric constant of silica particles with a variation of the surface porosity and TEOS wafer were conducted using the spectroscopic ellipsometry as a function of wavelength to be used to calculate the Hamaker constant of each sample. Tabor-Winterton approximation was employed for the Hamaker constant calculation with an assumption of two different bodies interacting in a aqueous medium of water. For A_{132}, body 2 was fixed as a TEOS surface whereas body 1 was varied by the type of silica particles synthesized with various surface porosities. The final step of this study was the calculation of total DLVO interaction energy and van der Waals force between silica sphere surface and TEOS flat surface in a liquid medium using the previous result of the Hamaker constant calculated.

As a result, the surface porosity of silica particles influences the refractive index and dielectric constant resulting in the variation of the Hamaker constant. Both the refractive index and dielectric constant of silica particles decrease with increasing the surface porosity due to the change in the surface roughness. The low Hamaker constants were obtained in highly porous silica particles due to lower particle density compared to nonporous one. DLVO interaction energy and force between silica sphere and TEOS also were calculated from the results of the Hamaker constant. As expected, the van der Waals attractive force decreases with increasing the surface porosity of silica particles indicating that lower adhesion force between porous abrasive slurry particles and wafer

surface may be expected to be observed in CMP performance leading to lower surface defects.

(a)

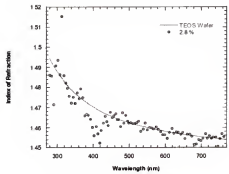

(b)

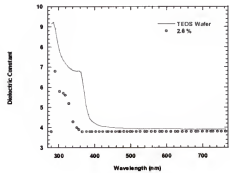

(c)

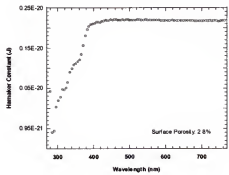

Figure 4-1 Index of refraction, dielectric constant, and Hamaker constant of 2.8 % porous silica particles as a function of wavelength: (a) index of refraction, (b) dielectric constant, (c) Hamaker constant.

(a)

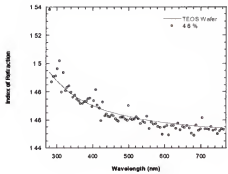

(b)

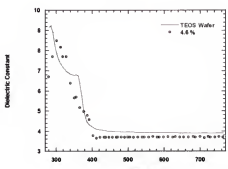

(c)

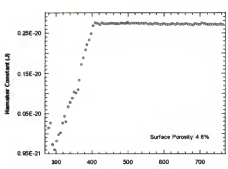

Figure 4-2 Index of refraction, dielectric constant, and Hamaker constant of 4.6 % porous silica particles as a function of wavelength: (a) index of refraction, (b) dielectric constant, (c) Hamaker constant.

(a)

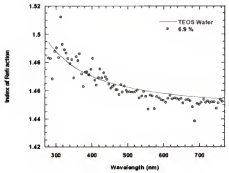

(b)

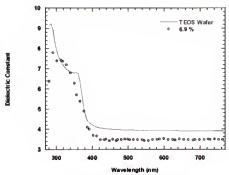

(c)

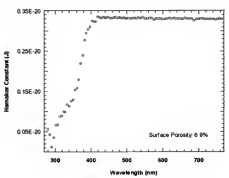

Figure 4-3 Index of refraction, dielectric constant, and Hamaker constant of 6.9 % porous silica particles as a function of wavelength: (a) index of refraction, (b) dielectric constant, (c) Hamaker constant.

(a)

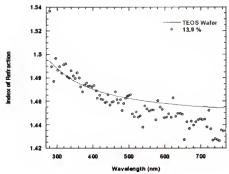

(b)

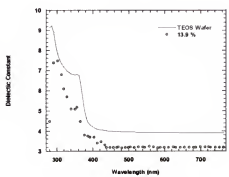

(c)

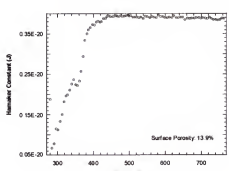

Figure 4-4 Index of refraction, dielectric constant, and Hamaker constant of 13.9 % porous silica particles as a function of wavelength: (a) index of refraction, (b) dielectric constant, (c) Hamaker constant.

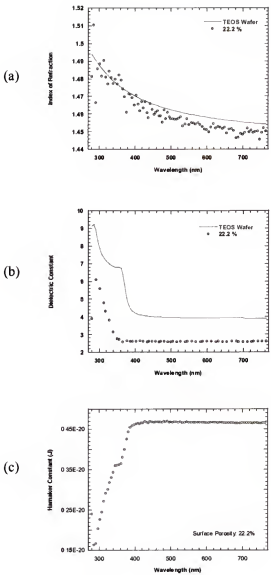

Figure 4-5 Index of refraction, dielectric constant, and Hamaker constant of 22.2 % porous silica particles as a function of wavelength: (a) index of refraction, (b) dielectric constant, (c) Hamaker constant.

(a)

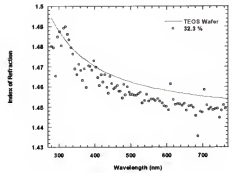

(b)

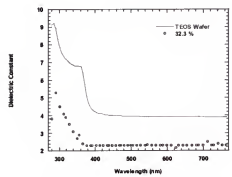

(c)

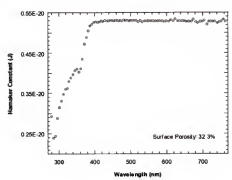

Figure 4-6 Index of refraction, dielectric constant, and Hamaker constant of 32.3 % porous silica particles as a function of wavelength: (a) index of refraction, (b) dielectric constant, (c) Hamaker constant.

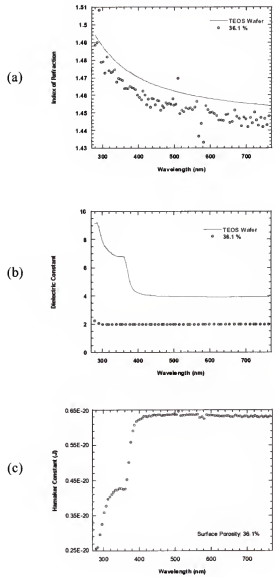

Figure 4-7 Index of refraction, dielectric constant, and Hamaker constant of 36.1 % porous silica particles as a function of wavelength: (a) index of refraction, (b) dielectric constant, (c) Hamaker constant.

(a)

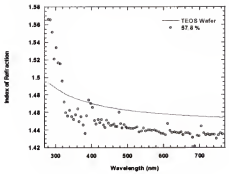

(b)

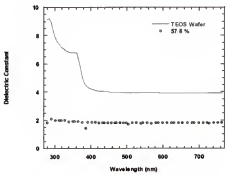

(c)

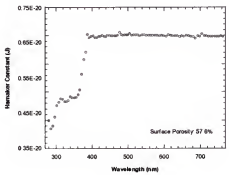

Figure 4-8 Index of refraction, dielectric constant, and Hamaker constant of 57.6 % porous silica particles as a function of wavelength: (a) index of refraction, (b) dielectric constant, (c) Hamaker constant.

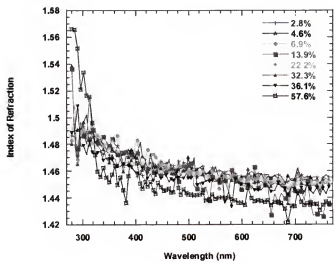

Figure 4-9 Effect of the surface porosity on index of refraction of silica nanoparticles as a function of wavelength.

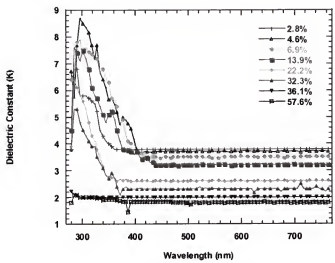

Figure 4-10 Effect of the surface porosity on dielectric constant of silica nanoparticles as a function of wavelength.

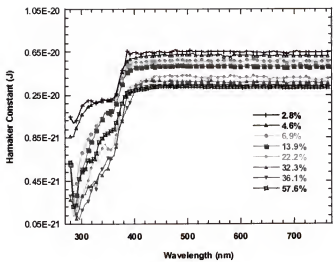

Figure 4-11 Effect of the surface porosity on Hamaker constant of silica nanoparticles as a function of wavelength between 280 nm and 770 nm..

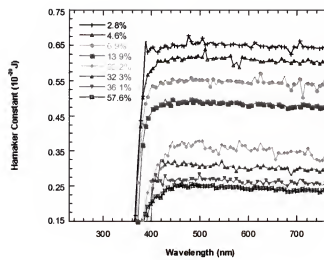

Figure 4-12 Effect of the surface porosity on Hamaker constant of silica nanoparticles as a function of wavelength between 360 nm and 770 nm.

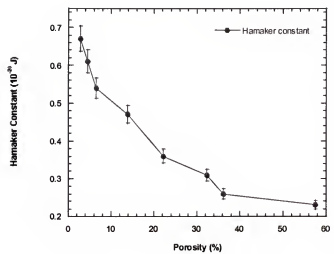

Figure 4-13 Hamaker constant of silica nanoparticles as a function of the surface porosity.

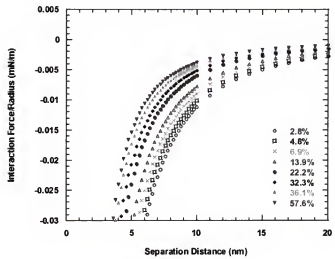

Figure 4-14 van der Waals force calculated by DLVO theory between porous silica particle surface and TEOS flat surface as a function of separation distance.

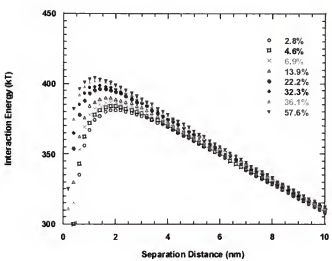

Figure 4-15 Total DLVO energy constant charge between porous silica particle surface and TEOS flat surface as a function of separation distance.

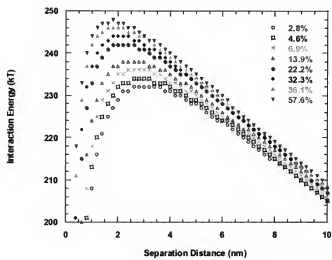

Figure 4-16 Total DLVO energy constant potential between porous silica particle surface and TEOS flat surface as a function of separation distance.

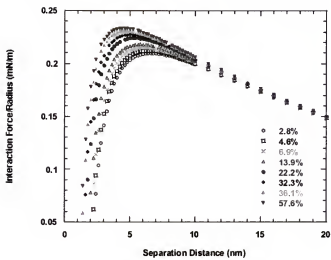

Figure 4-17 Total DLVO force constant charge between porous silica particle surface and TEOS flat surface as a function of separation distance.

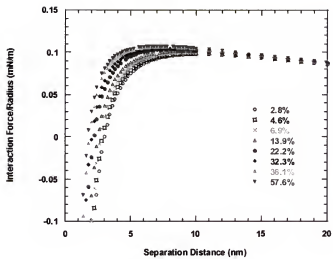

Figure 4-18 Total DLVO force constant potential between porous silica particle surface and TEOS flat surface as a function of separation distance.

CHAPTER 5
DIRECT FORCE MEASUREMENTS

Introduction

In chapter 4 the interaction between spherical nanoporous silica particles with a variation of the surface porosity and flat TEOS surface in an aqueous medium has been studied by calculating the Hamaker constant and van der Waals attractive force using the optical measurements of the refractive index and dielectric constant of silica spheres as a function of wavelength. As a result of these calculations, the highly porous silica particles led to lower refraction index and dielectric constant resulting in lower values of the Hamaker constant, A_{132}, between nanoporous silica particles and TEOS interacting in water. This result also pointed out that lower van der Waals force is dominant in highly porous silica-TEOS interaction in an aqueous solution.

In this chapter, we want to confirm this result by measuring the direct forces between silica particle probe and nanoporous silica particle surface, which is a small pellet mounted in the polymeric material and then polished until silica particle surface appears, using AFM technique. The interaction between silicon nitride tip and nanoporous silica particles with a variation of the surface porosity also was measured for the comparison. It was found that the van der Waals attractive force between silicon nitride tip and nanoporous silica particle surfaces in an aqueous solution at pH 3 was much larger than that between silica probe and nanoporous silica particle surface. These

results were agreed well with the calculation of the Hamaker constants and van der Waals forces conducted in chapter 4 and the interaction energy could be described well by DLVO theory.

van der Waals Force

One of the most important forces in surface and colloid chemistry is van der Waals forces between atoms, molecules, or particles. These forces have their origin in the dipole or induced-dipole interactions at the atomic level and are therefore of extreme importance in almost all aspects of the study of materials. The strength of van der Waals forces increases in the case of interaction between macroscopic objects such as colloidal particles since typically each particle has a large number of atoms or molecules [Mye99].

Almost all interfacial phenomena are influenced to various extends by forces that have their origin in atomic- and molecular-level interactions due to the induced or permanent polarities created in molecules by the electric fields of neighboring molecules or due to the instantaneous dipoles caused by the positions of the electrons around the nuclei [Atk86]. These forces consist of three major categories known as Keesom interaction between two permanent dipoles, Debye interaction between permanent dipole and induced dipole, and London interaction between two induced dipoles [Got97]. The three are known collectively as van der Waals interactions and play a major role in determining material properties and behavior important in colloid and surface chemistry.

The London force is always present like the gravitational force because it does not require the existence of permanent polarity or charge-induced polarity in the molecules. Even neutral atoms or molecules such as helium or hydrocarbons give rise to the London interaction [Cha85]. As a consequence, the London interaction plays a special role in colloid and surface chemistry. It influences physical adsorption and surface tension. In

addition, it is important in adhesion, wetting phenomena, structure of macromolecules such as proteins and other biological and nonbiological polymer molecules, and stability of foams and tin films. It also plays a very important part in determining the strengths of solids, properties of gases and liquids, heat of melting and vaporization of solids, and the like [Duc91].

The van der Waals forces are always attractive although the London forces between two macroscopic bodies immersed in a medium can be repulsive, depending on the material properties [Ham37]. They are relatively long ranged compared to other atomic- or molecular-level forces and can have an interval of influence ranging from about 0.2 nm to over 10 nm. The London force is also often called the dispersion force. The word dispersion has noting to do with the role of the London force in colloidal dispersions, but is the result of the role this type of interaction force plays in the dispersion of light in the visible and ultraviolet wavelengths. The dispersion force between two atoms, molecules, or large bodies is influenced by the presence of other nearby particles.

The interaction energy of two molecules of condensed matter may be written as Lennard-Jones potential:

$$U = -\frac{C}{r^6} + \frac{B}{r^{12}} \qquad 5.1$$

where C is London dispersion force constant related to the polarizability of the molecule, B is Born repulsion force constant, and r is molecular radius [Got97].

C may be related to a and b by

$$C = \frac{9ab}{4\pi^2 N_a^3} \qquad (\mathrm{Jm}^6) \qquad 5.2$$

Hence, molecular forces between non-polar molecules may be referred to as van der Waals forces, London forces, and dispersion forces. Hamaker calculated the total interaction between two spherical particles by adding contributions for each atom in the solid as described in Equation 4.11. The Hamaker constant was defined in Equation 4.12.

Among the many contributions to the forces between surfaces, e.g. double layer, structural, steric, depletion, hydration, and hydrophobic forces, there is one type of interaction that is always present, the van der Waals (vdW) interaction. Since the vdW interactions are ubiquitous, vdW forces play an important role in the stability and rheology of a colloidal dispersion, as well as many other colloidal and interfacial phenomena such as adhesion, adsorption, wetting and spreading of liquids, and more. Therefore, obtaining full knowledge of the vdW interactions between surfaces by a quantitative description and a direct measurement is of fundamental importance previously stated.

The vdW forces may be attractive or repulsive. For like materials, the vdW forces are always attractive, however, repulsive forces are predicted for certain dislike material combinations. The fact that the vdW forces can be repulsive is not well reported, since the cases of repulsive vdW interactions are very rare. For this reason, the direct measurements and theoretical studies of repulsive vdW have been spare. Furthermore, repulsive vdW forces can be measured with higher precision than attractive vdW forces [Hor90].

The atomic force microscope (AFM) has been a major analytical tool for the characterization of interfacial phenomena by measuring the interaction forces between two surfaces. Measurements of forces on the order of a few nano-newtons have been performed using the AFM. The AFM can be used to measure repulsive vdW forces,

which arise between different surfaces across the intervening medium. Comparison of the results acquired from the direct measurements with the theoretical predictions can enable us to analyze the repulsive vdW forces thoroughly.

Surface Force Measurement Techniques

The behavior of colloidal dispersion and a variety of interfacial phenomena depend on the forces interacting between surfaces. As a result, several different techniques have been developed for measuring forces between a variety of surfaces during the last decades. The AFM is now regarded a valuable force measurement instrument. This technique is very sensitive and a wider variety of surfaces can be employed because the surfaces do not need to be transparent. Furthermore, the force measurements can be performed much faster than previously described techniques. This ability of the AFM has made it an important tool for imaging surfaces in the areas of materials science and engineering as well as many other areas such as colloidal science, biology, and more. The instrument relies on the contact between a sharp tip and the surface of the sample to create the image. This allows the instrument to image both conductive and nonconductive surfaces in a variety of media including air, other gases, liquids, and vacuum. The two most commonly used modes of operation for surface imaging are contact mode AFM and tapping mode AFM.

Figure 5.1 shows the setup of contact mode AFM force measurement consisting of scanning the probe across a sample surface while monitoring the change in cantilever deflection with the split-diode photo detector. The piezoelectric scanner moves the sample in a raster scan pattern underneath the tip to produce a height image. As the cantilever starts deflecting upward due to a change in the topography of sample, the scanner lowers the sample begins to deflect downward, the scanner raises the sample.

The voltage, which is applied to the scanner as the scanner moves the sample in a raster pattern is recorded by the computer. This recorded voltage applied to the scanner in the x and y directions is used to create the x and y directions of the image. The recorded voltage applied to the z direction is used to make color differences in the image, which refers to different heights [Laa01].

In tapping mode AFM, the cantilever on which the tip is mounted is oscillated at a frequency near its resonance frequency while the tip is separated from the sample surface. The oscillation is driven by a constant driving force and the amplitude of its oscillation is monitored. The tip is brought toward the sample surface until it begins to touch the surface, which reduces the oscillation amplitude. The feedback control loop of the system then maintains this new amplitude constant as the oscillating or tapping tip traverses the system. This is done by the z component of the piezoelectric scanner, which is changing the tip height to exactly adjust for the surface height variations as the tip scans across the sample surface. Tapping mode technique is typically used for soft or delicate materials such as biological samples or rubber, which might be distorted or damaged by the tip sliding across the surface [Lou94].

Force-Separation Curves by AFM

The AFM was originally intended for three-dimensional imaging of surfaces and was modified to measure forces between a surface and the tip of a cantilever. It was extended to measure the forces between a particle and a surface by attracting a probe particle to the cantilever and has emerged as a powerful tool for studying the indentations between surfaces. The interaction forces between the tip and the sample can be measured by the AFM as a function of separation distance. The force-separation curves yield information regarding the sample and the tip. The force measurement can be done in air,

as well as liquid and vacuum and a variety of forces between surfaces such as electrical double layer, vdW forces, polymer-induced forces, hydration, and hydrophobic forces can be recorded in the force-separation curves.

Alternatively raising the sample into contact with the tip and then lowering it out of contact with the tip produces the force-separation curves. As the sample arises toward the tip, any attractive or repulsive force between the tip and the surface is recorded. A cantilever deflection-distance curve is shown in Figure 5.2. The x-axis represents the distance moved by the sample in nanometers and the y-axis corresponds to the deflection of cantilever in volts as measured by the piezoelectric scanner. The solid curve and dashed curve show the approaching curve generated when the sample is raised into contact with the tip and the retracting curve produced when the sample is pulled away out of contact with the sample respectively. At the point labeled "A" in Figure 5.2 the surface ramps towards the tip. At large separation, no force is exerted, hence no deflection of cantilever is observed and the portion is called the zero force region. As the sample moves close to the tip, surface forces are exerted the tip and the surface as marked "B". In this case shown, the tip feels repulsive forces and the cantilever deflects upward before making contact with the surface. At the point "C" the surface is brought very close to the tip and the tip responds to attractive forces from the sample and the cantilever deflects downward and eventually the tip is in contact with the sample. Once the tip and the surface contact each other, the cantilever deflects linearly with respect to surface movement and the constant compliance region is referred to this region marked "D". After loading the cantilever to a desired force value, the process is reversed. As the sample is brought down from the tip, adhesion or bonds formed during contact cause the tip to adhere to the sample some distance past the initial contact point on the approaching

curve. The point labeled "E" is where the adhesion is overcome and the the tip comes free from the surface [Got97].

The cantilever deflection-distance curve is the raw data, which is obtained directly from the AFM. This raw data needs to be converted into the force-separation curve because the cantilever deflection has little meaning by itself and the distance moved by the sample is useless without a reference for the movement. The cantilever deflection-distance curve can be converted into the force-separation curve with a known spring constant of the cantilever. The x-axis in the force-separation curve shows the separation distance between the sample and the tip. To get the separation distance from the distance moved by the sample, a reference point should be known. The surface of sample should be chosen point. To find the surface of sample a straight line is fitted to the constant region, and another straight line is fitted to the zero force region. The value of distance where these two straight lines cross becomes zero on the x-axis of the separation. The x-axis of distance moved is then shifted to this new scale. The y-axis represents the normalized force, which is converted from the cantilever deflection. The conversion into force is done by multiplying the spring constant of the cantilever by the amount of deflection and this force is then normalized by dividing by the radius of the tip.

Experimental

Flat Substrate Preparation

Silica nanoparticles with various surface porosities from 2.8% to 57.6%, which were synthesized previously by a precipitation technique using the hydrolysis reaction of silicon alkoxide in ethanol, were used for the preparation of the flat substrate to be used in the direct force measurement between silica spheres and silica particle probe, and between silica spheres and silicon nitride tip in a liquid solution at pH 3. The fine silica

particles were pressed in size of 0.25 inch diameter die with very low pressure of 1000 *Psi* using CARVER Hydraulic Press (Wabash, IN) to avoid any change in mechanical properties such as the hardness and elastic modulus of the particle itself. The BUEHLER sample-kwick cold mounting material (Lake Bluff, IL) consisting of polymeric powder and liquid solution was employed for mounting the small pellet samples. The mixed gel of cold mounting powder and liquid with ratio of 2 to 1 was poured into 0.5 inch mold and then the pellet was put onto the gel. To cover the whole sample, more gels were poured and then the sample was hardened at room temperature. The hard sample was polished carefully using a polisher with sand paper until the silica particles appear. Figure 5.3 shows a schematic diagram of flat substrate of nanoporous silica particles.

TEOS wafer was also prepared for the direct force measurements for two cases, silica probe and silicon nitride cantilever tip. TEOS piece of 1.3 ×1.3 cm^2 in size was cut from the 2 inch Wafers. It was cleaned with an acetone in the ultrasonificator and then rinsed with deionized water.

Colloid Probe Preparation

The colloid probes were prepared by attaching a 5 μm amorphous silica sphere (Duke Scientific, Palo Alto, CA) on the tip of the 200 μm wide Si_3N_4 contact mode cantilevers (Digital Instruments, Santa Babara, CA) using a thermoplastic polymer glue (Epon R 1004f, Shell Chemical, Houston, TX).

Attaching colloid spheres on the tip of cantilevers was done by the following sequence. A 25 μm tungsten wire (Goodfellow, Berwyn, PA) was attached to a three-dimensional translation table. The translation table was positioned beside an optical microscope (Fisher Scientific, Pittsburgh, PA) so that the end of the tungsten wire was in focus in the microscope. The microscope was designed so that the sample stage would

raise and lower to bring the sample into focus. Since the lens assembly remained fixed, the tungsten wire would remain in focus as the sample was raised into focus. A small amount of glue, the AFM cantilevers, and a small amount of the spheres were placed on the different microscope slides. The slide with the glue was placed on the microscope stage and the glue was positioned under the tungsten wire. The sample was then raised until the glue touched the wire. With the glue clung to the wire, the slide with the cantilevers was placed on the microscope stage and the glue was dropped on the tip of the cantilever. The cantilever with the glue was then heated and after melting the glue covered the tip of the cantilever. By the same method, which was described previously, the colloid sphere was dropped on the glue covered tip of the cantilever, then the cantilever was slightly reheated to improve the adhesion of the sphere to the tip. Figure 5.4 shows the micrograph of 5 μm amorphous silica particle probe attached onto silicon nitride cantilever tip. The colloid probes were cleaned by copious rinsing with isopropanol and water, and dried immediately prior ro experimentation.

Solution Preparation

DI water was used as an aqueous medium solution and pH was adjust with *HCl* and NH_4OH. Water was filtered through a 0.2 μm syringe filter (Fisher Scientific, Pittsburgh, PA). In the AFM experiment, water was introduced into the AFM fused silica liquid cell (Digital, Instruments, Santa Babara, CA) via a syringe (Fisher Scientific) and allowed to reach thermal equilibrium prior to the collection of force separation data

Determination of the Spring Constant of the AFM Cantilever

The normal spring constants of the cantilevers were determined by measuring the resonant frequency of cantilevers with a known mass at the end according to the method proposed by Cleveland [Cle93]. The resonant frequency of a cantilever, ν, can be given

by

$$\nu = \frac{1}{2\pi}\sqrt{\frac{k}{M+m}} \qquad 5.3$$

where k is the spring constant, M is the added end mass, and m is the effective mass of the cantilever itself. For an unloaded cantilever, the effective mass, m, can be written as

$$m = \frac{(2\pi)^2 k}{\nu_0^2} \qquad 5.4$$

where ν_0 is the resonance frequency of an unloaded cantilever. From combining two equations, Equations 5.3 and 5.4, the spring constant can be expressed as

$$k = (2\pi)^2 \frac{M}{\left(1/\nu_1\right)^2 - \left(1/\nu_0\right)^2} \qquad 5.5$$

where ν_1 is the resonant frequency of a cantilever with added mass. The spring constant, k, and the effective mass of a cantilever, m, can be calculated from Equations 5.4 and 5.5 by measuring the resonant frequency of the cantilever and the added mass. Utilizing this method, the average spring constant of a 5 μm amorphous silica sphere was determined to be 0.16 nN/μ. The values of spring constant and effective tip radius of silicon nitride cantilever used to transform PSD voltages to force, which were given by the vendor, were 0.12 nN/m and 500 nm, respectively.

Direct Force Measurements

All AFM experiments were conducted by a Nanoscope III AFM (Digital Instruments, Santa Babara, CA) in a fused silica liquid cell using the colloid probe

technique. A schematic drawing of the AFM force measurement setup is shown in Figure 5.1. In this device, the force between a flat sample and a colloid probe is measured as a function of the displacement of the sample. Sample displacement is achieved using a piezoelectric scanner. The colloid probe is mounted on a cantilever, which will bend up or down depending on whether the interacting force is repulsive or attractive. A laser beam, which is reflected from the back of the cantilever falls onto a split-diode photo detector. Any small change in the deflection of the cantilever is detected by a split-diode photo detector. A 20-50 μm laser beam is used and a split-diode photo detector is divided in four quadrants. As mentioned previously, the cantilever deflection is monitored as a function of the piezo extension and contraction. As a result, the raw data of the deflection of the cantilever versus the displacement of the flat surface is obtained. To convert the raw data into an interaction force versus separation distance, the zeros of force and separation distance is defined from the zero force region and the constant compliance region and the amount of the deflection of cantilever is multiplied by the spring constant of cantilever.

Results and Discussion

Interaction between Silica Probe and Nanoporous Silica Particles

The interaction force measurement between spherical silica probe and nanoporous silica particle flat surface mounted polymeric material were conducted in deionized water (DIW) at pH 3. The silica probe-TEOS interaction also was observed in air for the investigation of the effect of the type of the medium. In the Figures 5.5 through 5.9 both the PDS voltage-sample position curve and the force-separation curve are plotted, since the former is the direct measured result but is not convenient to compare among themselves. The latter force result is more widely known but is indirectly obtained with

the possibility of increasing error. However, since all experiments of silica-silica interactions were done with the same silica particle probe the inaccuracy of some parameters such as spring constant or tip radius will not hinder the validity of cross-consistent. In general, since the retracting direction often involves adhesion forces which always cause tip instability, AFM force measurement is more accurate from the approaching direction. Thus the approaching curve at short separation distance is especially plotted for each case and may reveal more detailed information.

Figure 5.5 shows the results of the silica probe-TEOS interaction in air. The plot of PSD voltage versus sample position represents both approaching and retracting curves indicating that the approaching curve does not show any attraction, whereas the retracting curve shows a little adhesion force. It clearly indicates that the repulsive force is dominant in the interaction between silica-silica surfaces due to the same surface charge. The silica probe-nanoporous silica with different surface porosities (2.8%, 22.2%, 36.1%, and 57.6%) interaction force measurements conducted in deionized water at pH of 3 are shown in Figure 5.6 through Figure 5.9. The approaching curves of all cases do not show any attraction force or energy barrier when the silica probe approaches from the long distance until it touches the sample surface. The trend of the approaching curve of each sample is the same as that of silica probe-TEOS wafer surface. It is meant that the surface porosity does not influence the repulsive force between silica-silica surface. However, in the retracting curves of silica probe-nanoporous silica surfaces, a little change in adhesion force was observed depending on the surface porosity. The adhesion force between silica probe-nonporous silica particle (2.8%, Figure 5.6) in water is similar to that of silica probe-TEOS interaction but is reduced somehow due to the capillary effect in air. The adhesion force is decreased as the surface porosity of silica particle increases as shown in

Figures 5.6 through 5.8 and then it is vanished in the silica probe-highly porous silica particle of 57.6% surface porosity as shown in Figure 5.9. Figure 5.10 shows all approaching curves of silica probe-nanoproous silica particles including TEOS surface resulting in the difference of the repulsive force depending on the surface porosity. The highly porous silica surface presents the high repulsive force while other silica particles with lower surface porosity show almost same values of the repulsive forces even though being observed a little increasing as the surface porosity increases. Figure 5.11 shows all retracting curves of silica probe-nanoporous silica surface and TEOS surface interactions. All samples except for 57.6% porous silica particle show the adhesion force in short distance range of about 10 nm. The reduction of the adhesion force is observed in silica probe-nanoporous silica particle surface interaction indicating that the surface porosity influences the adhesion force in that it is inversely proportional to the adhesion force. Furthermore, the highly porous silica particle does not show any more adhesion force between silica-silica interaction. It is clear that the silica-silica interaction is dominated by the electrostatic repulsive force for all separation distance ranges when the silica probe approaches the sample surface, while the weak adhesion force exists between them when the silica probe detaches in short separation distance due to the attractive van der Waals force.

Interaction between Silicon Nitride Tip and Nanoporous Silica Particles

The direct force measurements of the silicon nitride tip-nanoporous silica particles interactions were performed in an aqueous solution with a fixed pH of 3. The silicon nitride tip-TEOS surface interaction also was observed in air. Figure 5.12 shows the silicon nitride tip-TEOS surface interaction in terms of both the PSD voltage-sample position curve and the force-separation distance curve. The approaching curve in the

bottom plot of Figure 5.13 shows a long range attractive force starting at 150 nm from TEOS surface. Since generally van der Waals force becomes essentially zero after around 20 nm separation, the long range attractive force cannot be attributed to the van der Waals force only. There must be some other forces that play a predominant role in the apparent attractive force. One of the possibilities is the electrostatic force. If two surfaces are opposite charges each other, the electrostatic interaction between them is attractive. Since the surrounding medium is air, the electrostatic force will not be effectively screened so that the interaction range becomes quite long in comparison to the case of an aqueous solution [Mar87].

An the other hand, the retracting curve in the same figure shows a very large adhesion force compared to that between silica-silica interaction. Similar results were also observed by other people, which indicates that the large adhesion force in air is attributed to capillary force [Mar87, Wei89]. Water molecules condense almost any surface in room temperature to form a very thin water layer. When the tip touches the sample surface, the water layers between the two surfaces form a neck with negative curvature. Therefore, the capillary force is in the direction to keep the two surfaces to be close. If the two surfaces are immersed into water, then the capillary force should vanish and the adhesion force be greatly reduced. The normalized adhesion force is reduced significantly in silicon nitride tip-nonporous (2.8%) silica particle surface in water at pH 3. This is shown in Figure 5.13 by the comparison with the silicon nitride tip-TEOS surface interaction in air as shown in Figure 5.12.

The approaching curve in Figure 5.13 shows a repulsive force at long separation between silicon nitride tip and silica particle surface with low porosity of 2.8%. At short separation distance the force becomes attractive and the tip suddenly jumps onto the silica

particle surface. This can be understood by combining van der Waals force and the electrostatic force. From the Figure 6.2 in chapter 6, the zeta-potentials of TEOS and silicon nitride particles at pH 3 are -21 mV and 22 mV, respectively, indicating that the electrostatic interaction between silicon nitride-silica surfaces is repulsive at long separation distance, whereas the van der Waals interaction becomes dominant at short separation distance so that the total interaction force is attractive. It should be noted that the zeta-potential value of silicon nitride wafer measured in water by the streaming potential technique may not be equal to that of silicon nitride tip. However, we would expect more positive zeta-potential value of silicon nitride particles due to larger surface area. At short separation distance the attractive van der Waals is predominant so that the total force becomes attractive and causes a maximum force barrier at the turning point.

The silicon nitride tip-silica particle surface interactions are changed when the surface porosity of silica particle increases. The energy barrier on the approaching curve of silicon nitride-silica interaction is decreased with increasing the surface porosity of the silica particles as shown at short separation distance in both Figures 5.13 and 5.14. The energy barrier is vanished in the approaching curves of silicon nitride-highly porous (36.1% and 57.6%) silica particle interactions as shown in Figures 5.15 and 5.16. It is meant that the repulsive force is predominant in highly porous silica particle surface with the reduction of attractive van der Waals force at short separation distance. Figure 5.17 shows all approaching curves of silicon nitride-porous silica particle surface interaction in water at pH 3 including that of silicon nitride-TEOS interaction in air. It clearly indicates that the repulsive force predominates the total interaction at short separation distance resulting in the reduction of the energy barrier as the surface porosity increase. The silica particles embedded flat surface is so rough that the approaching curve of all silicon

nitride tip-porous silica particle surface interactions is not smooth at short separation distance, while that of silicon nitride tip-TEOS surface interaction is very smooth as shown in Figure 5.17.

The retracting curve of silicon nitride-porous silica particle surface also changes when the surface porosity of silica particle changes. As a result, the adhesion force is decreased significantly with increasing the surface porosity. The adhesion forces of silicon nitride-nonporous or low porous silica particle surface (2.8% and 22.2%, respectively) interactions in water at pH 3 are similar to that of silicon nitride-TEOS interaction in air. However, The adhesion force of silicon nitride-36% porous silica particle surface interaction is significantly reduced as shown in Figure 5.15 and that of silicon nitride-57.6% porous silica surface interaction is almost vanished. Figure 5.18 apparently shows that the changes in the adhesion forces of silicon nitride-porous silica particle surface interactions including that of silicon nitride-TEOS surface interaction at short separation range.

As a consequence, the strong attractive force exists in silicon nitride-silica surface interaction much more than in silica-silica interaction due to the opposite surface charges between them indicating that the van der Waals force is predominant in silicon nitride-silica surface interaction at short separation distance. However, this van der Waals force decreases as the surface porosity increases. No repulsive force was observed in the approaching curve. This is because the electrostatic force is so small that in all interaction ranges the van der Waals force predominates. The retracting curve also shows an adhesion force. It can be seen from the figures that with the increasing the surface porosity the degree of "jump-in" near the surface after a force barrier decreases in every approaching curve. The force is attractive until the tip touches the surface. The force

after "jump-in" is repulsive all the way to the surface. The "jump-in" seems to result from the breaking of a surface film structure. A similar observation was also shown in the work of Manne [Man94] but was not discussed. The retracting curves show an adhesion force at short separation and then overlap with approaching curve when the tip moves far away from the substrate surface.

The adhesion force is difficult to analyze quantitatively. First of all, the contact area cannot be easily defined, as revealed by Hertz model [Her81], DMT model [Der75], and JKR model [Joh71] for instances. The contact area is highly dependent of the surface forces as well as the applied force. If the forces are not clearly known, the contact area cannot be predicted. Furthermore, all the models are dealing with viscoelastic deformation during contact. If plastic deformation occurs, then these models are not applicable. Secondly, the interfacial energies are not generally available. Even if the contact area is known, it still requires the knowledge of interfacial energy to evaluate adhesion. The interfacial energy itself between a solid and a liquid or gas is a challenging task to evaluate. In fact, people measure the interfacial energy by measuring adhesion force. Thirdly, surface roughness will influence adhesion force greatly. It is reported that even small surface asperities can significantly reduce adhesion [Tab77]. Finally the tip may move on the surface during retraction, causing ill-defined geometry and contact area. These are the reason that the adhesion force in AFM force measurements generally gives a large deviation, and only the trends of the adhesion can be discussed.

We can discuss a general behavior of adhesion force based on all experiments presented above. As long as there is a repulsive force, or an increased repulsive force on the approaching curve, then adhesion force on the retracting curve will be reduced.

Summary

In this study the silica-silica surface and the silicon nitride-silica surface interactions were investigated using a single silica particle probe and silicon nitride tip interaction with the porous silica particle embedded in the cold mounting polymeric material by AFM. No potential barrier or "jump-in" on the attracting curves was observed in the silica-silica interaction indicating that the repulsive energy is predominant when the silica particle probe approaches the silica flat surface for all cases of the samples. However, the degree of the repulsive force on the approaching curves depends on the surface porosity of silica particles embedded on the flat substrate surface. It means that the surface porosity influences the silica-silica interaction due to lower Hamaker constant of highly porous silica particles leading to lower van der Waals attraction force, even though it is not significant. In the retracting curves of silica-silica interaction the adhesion force was observed when the silica probe moves away from the substrate surface at short separation distance. This adhesion force was decreased with increasing the surface porosity of silica particles existing on the substrate surface and finally vanished at highly porous silica sample (57%) indicating that the van der Waals force becomes weaker as the surface porosity increases while the repulsive force between silica-silica interaction becomes stronger depending on the surface porosity of the sample.

On the other hand, the "jump-in" on the approaching curves was observed in the silicon nitride-silica interaction for all samples indicating the strong van der Waals force was caused when the silicon nitride tip approaches the silica substrate surface since they are opposite charges each other. The reason that the position of "jump-in" is not regular in each sample is because the silica substrates surfaces, which is composed of porous silica particles, are not smooth. The surface porosity of silica particles does not affect

significantly the interaction force between silicon nitride and silica except for a highly porous silica case, which does not show any attraction force. In the retracting curves of silicon nitride-silica interaction very strong adhesion forces were observed depending on the surface porosity of silica particles. The higher the surface porosity, the lower the adhesion force between silicon nitride and silica surfaces.

As a result, it has clearly proven that the surface porosity of silica particles influences significantly the interaction energy between silica or silicon nitride and silica surfaces using the direct force measurement in the liquid cell system by AFM and these result are agreed well with the results of van der Waals force and DLVO theory studied in previous chapter.

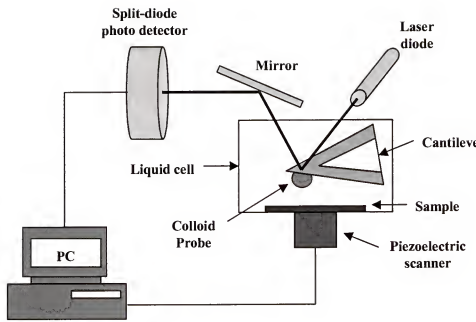

Figure 5-1 Schematic diagram of the AFM force measurement setup [Got97].

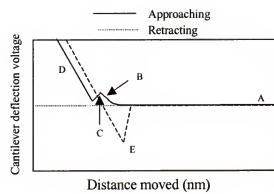

Figure 5-2 Cantilever deflection-distance curves. The solid curve represents the approaching curve and the dashed curve shows the retracting curve. Point "A" is the beginning of the approaching curve. The tip feels repulsive forces from the surface and the cantilever deflects upward at the point "B". At the point "C" the cantilever deflects downward and the tip and the sample eventually make contact. The portion of curve marked "D" is the constant compliance region. The tip detaches from the surface at the point "E" [Got97].

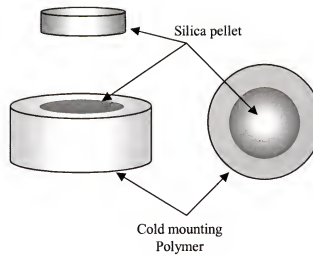

Figure 5-3 Schematic diagram of the nanoporous silica sample for the direct force measurement in liquid cell. The small pellet of silica particles are embedded into cold mounting polymeric material and then polished until the particles appear.

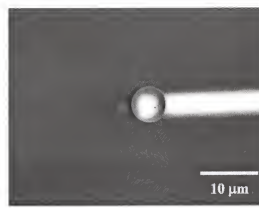

Figure 5-4 Micrograph of the silica particle probe of 5 μm size attached on silicon nitride tip.

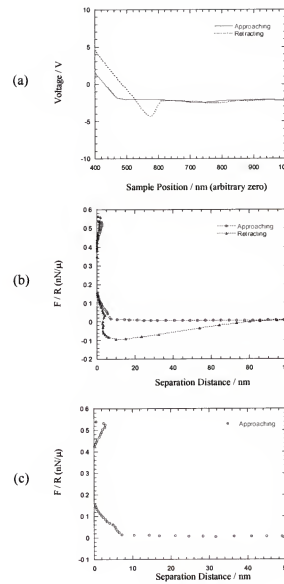

Figure 5-5 Silica probe–TEOS surface interaction in deionized water at pH 3. (a) plots of PSD voltage versus sample position, (b) plots of the normalized force versus separation distance, (c) plots of the normalized force versus separation distance when the sample approaches the silica probe.

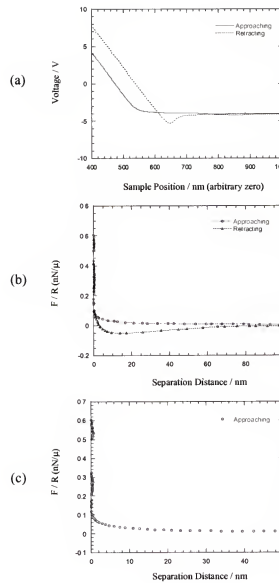

Figure 5-6 Silica probe–2.8 % porous silica surface interaction in deionized water at pH 3. (a) plots of PSD voltage versus sample position, (b) plots of the normalized force versus separation distance, (c) plots of the normalized force versus separation distance when the sample approaches the silica probe.

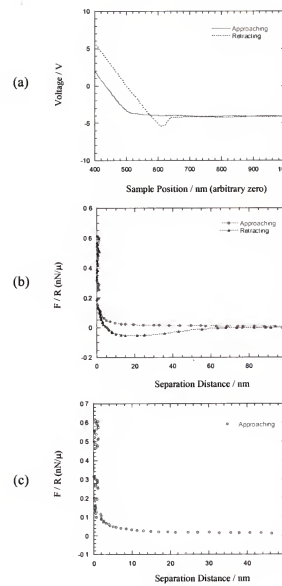

Figure 5-7 Silica probe–22.2 % porous silica surface interaction in deionized water at pH 3. (a) plots of PSD voltage versus sample position, (b) plots of the normalized force versus separation distance, (c) plots of the normalized force versus separation distance when the sample approaches the silica probe.

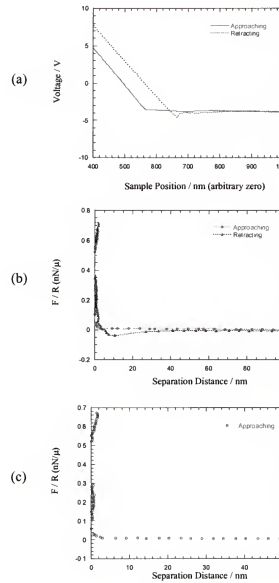

Figure 5-8 Silica probe–36.1 % porous silica surface interaction in deionized water at pH 3. (a) plots of PSD voltage versus sample position, (b) plots of the normalized force versus separation distance, (c) plots of the normalized force versus separation distance when the sample approaches the silica probe.

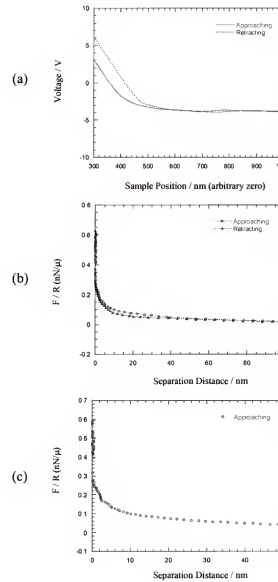

Figure 5-9 Silica probe–57.6 % porous silica surface interaction in deionized water at pH 3. (a) plots of PSD voltage versus sample position, (b) plots of the normalized force versus separation distance, (c) plots of the normalized force versus separation distance when the sample approaches the silica probe.

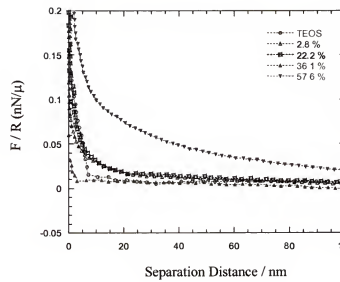

Figure 5-10 Plots of the normalized force versus separation distance silica probe–porous silica surface interaction in deionized water at pH 3 when the sample approaches the silica probe.

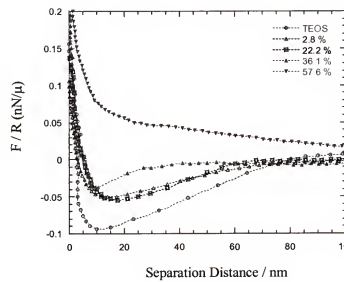

Figure 5-11 Plots of the normalized force versus separation distance silica probe–porous silica surface interaction in deionized water at pH 3 when the sample retracts the silica probe.

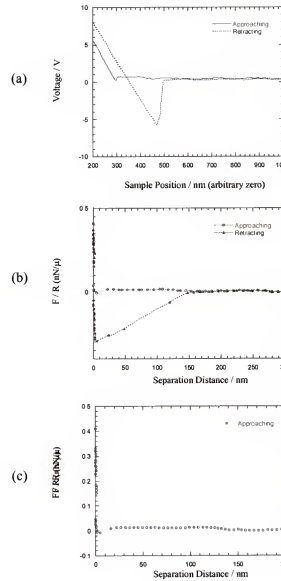

Figure 5-12 Silicon nitride probe–TEOS surface interaction in deionized water at pH 3. (a) plots of PSD voltage versus sample position, (b) plots of the normalized force versus separation distance, (c) plots of the normalized force versus separation distance when the sample approaches the silica probe.

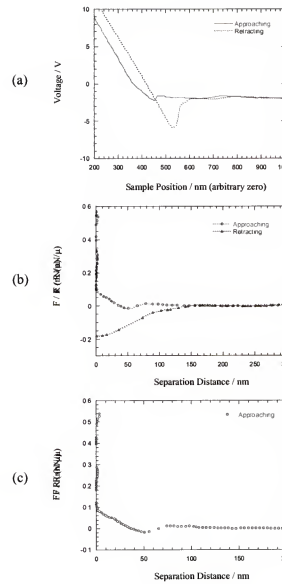

Figure 5-13 Silicon nitride prob-2.8 % porous silica surface interaction in deionized water at pH 3. (a) plots of PSD voltage versus sample position, (b) plots of the normalized force versus separation distance, (c) plots of the normalized force versus separation distance when the sample approaches the silica probe.

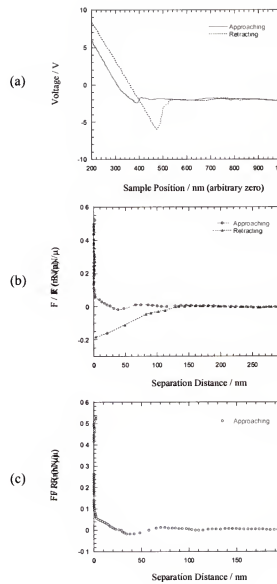

Figure 5-14 Silicon nitride probe–22.2 % porous silica surface interaction in deionized water at pH 3. (a) plots of PSD voltage versus sample position, (b) plots of the normalized force versus separation distance, (c) plots of the normalized force versus separation distance when the sample approaches the silica probe.

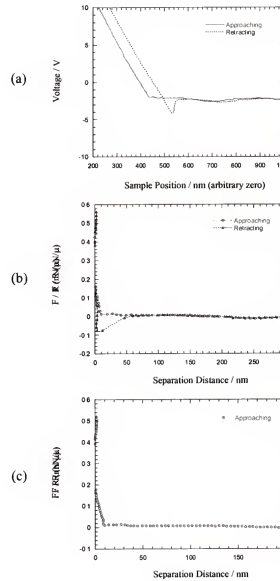

Figure 5-15 Silicon nitride probe–36.1 % porous silica surface interaction in deionized water at pH 3. (a) plots of PSD voltage versus sample position, (b) plots of the normalized force versus separation distance, (c) plots of the normalized force versus separation distance when the sample approaches the silica probe.

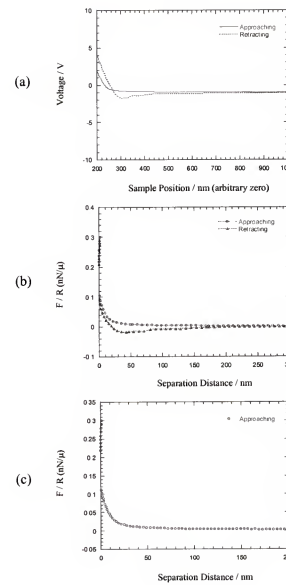

Figure 5-16 Silicon nitride probe–57.6 % porous silica surface interaction in deionized water at pH 3. (a) plots of PSD voltage versus sample position, (b) plots of the normalized force versus separation distance, (c) plots of the normalized force versus separation distance when the sample approaches the silica probe.

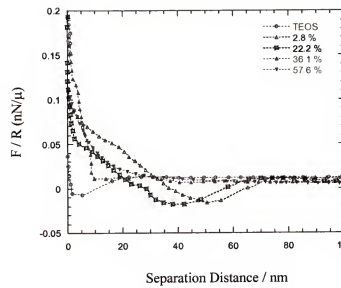

Figure 5-17 Plots of the normalized force versus separation distance silicon nitride probe–porous silica surface interaction in deionized water at pH 3 when the sample approaches the silica probe.

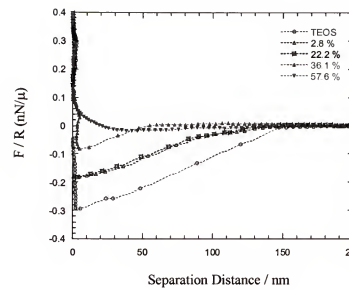

Figure 5-18 Plots of the normalized force versus separation distance silicon nitride probe–porous silica surface interaction in deionized water at pH 3 when the sample retracts the silica probe.

CHAPTER 6
SURFACE CHEMISTRY OF ABRASIVE SLURRY PARTICLES AND THEIR INTERACTIONS WITH WAFER SURFACES

Introduction

We have been studied the interaction forces between the spherical nanoporous silica particles and a flat wafer surface such as TEOS in terms of the van der Waals attractive force and the electrostatic repulsive force by measuring the optical properties such as the refractive index and dielectric constant of silica particles resulting in the calculations of the Hamaker constant and DLVO energy in chapter 4. Furthermore, we have conducted the direct force measurements of silica-silica and silica-silicon nitride interactions using AFM as described in chapter 5.

One of the purposes of this work is to design the slurry system based on nanoporous silica particles to reduce the surface defects of the wafer surface polished in CMP performance. The actual interaction during CMP is occurred between the abrasive slurry particles and wafer surface in an aqueous solution with additives such as salts or surfactants. Even though previous chapters revealed that the nanoporous silica particle based slurry can reduce the van der Waals force compared to nonporous large sized conventional abrasive particle based slurries, we need to investigate the abrasive particle-wafer surface interaction by measuring the zeta-potentials of the particles and wafers, which can lead to the calculations of DLVO energy and force.

The zeta-potentials of slurry particles such as nonporous silica particles and

nanoporous silica particles with the surface porosity of 57% and substrates such as silicon, TEOS, and silicon nitride have been measured by electrophoretic and streaming potential methods, respectively, to evaluate the electrical properties of surfaces. The zeta-potentials of oxide and metal surfaces showed similar values to those of particles as a function of pH. The interaction energy between the abrasive slurry particles and wafer substrates were calculated based on DLVO theory. Experimental results were well agreed with the theoretical calculation.

Surface Charge

When an interface is formed between solid and liquid, the solid surface will be charged because of the difference of the affinity of electrons to the surfaces [Fro99]. The charging mechanism depends on both the properties of the solid and the medium. One of the charging mechanisms is Nerst-type charging. When crystal particles are dispersed in water, an equilibrium will be established between the particle surface and the medium. Cations (M^+) and anions (M^-) have a high affinity to the particle surface and are adsorbed as if they are a part of the surface. When the number concentration differs between adsorbed ions of M^+ and M^-, the excess amount of either M^+ or M^- results in the corresponding charge of the particle. These ions are called potential-determining ions. Because the concentration of adsorbed ions is high enough that it is not affected by the charge of their bulk concentration, the following Nerst equation holds for the surface potential, ψ_0:

$$\psi_0 = -\left(\frac{2.3kT}{e}\right)\left(pM^+ - pM^-\right) \qquad 6.1$$

where k is the Boltzmann constant, T is the temperature, e is the elementary charge,

$p\,M^{+} = log a_{M^{+}}$, and $a_{M^{+}}$ is the activity of cation [Got97].

The surface charging also can be caused by dissociable groups. Particles with groups will be charged by their dissociation in an aqueous solution, and the degree of dissociation depends on the *pH* of the solution. For example, *-COOH* dissociates as $-COOH = COO^{-} + H^{+}$, and so the surface potential is always negative and varies with the pH. When a surface is zwitterionic because of *-COOH* and $-NH_3$ groups on the surface, the particle will be charged positively or negatively depending on the pH and p.z.c exists in-between. Varius oxide particles, such as SiO_2, TiO_2, and Al_2O_3 are easily dispersed in water and their surfaces become hydrophilic because the adsorption of water molecules results in the formation of *-OH* groups on the surface. Then the surface will be charged by the adsorption or desorption of H^{+} and the surface potential of particles varies with the pH in the similar way as that of zwitterionic particles. Isomorphic substitution also is one of the surface charging mechanisms which is found particularly in clay minerals. When there are defects in the crystal lattice in which Si^{4+} is substituted by Al^{3+}, or by Mg^{2+}, the deficit of positive charge results in charging particles. This charge is not affected by the pH value [Got97].

Other surface charging mechanisms can be explained by ions, ionic surfactants, or polymers. When ions, ionic surfactants, or polymers are adsorbed on the particle surface by the covalent force, the van der Waals force, or the electrostatic force, the particle will be charged because of the charge of adsorbed molecules. The adsorption of impurities with charge solution also results in the charge of particles. In these cases, the charging mechanism is hard to estimate [Chi77].

Electrical Double Layer around Spherical Particle and Their Charge

Particles in solutions are usually charged. Then, because of the electroneutrality

principle, ions which are of the same amount but different sign are attracted toward the particle surface [Ada67]. Figure 6.1 shows a schematic diagram of electrochemical double layer around particle surface in an applied electric field. A part of the ions is adsorbed directly on the particle surface to form the so-called Stern layer. The rest of the ions are in thermal motion, balancing the electrical attractive force to form a diffuse double layer. The potential at the outside of the Stern layer is called the Stern potential, ψ_d. Because the structure with the Stern layer is not well known, the Stern potential is often regarded as the surface potential of particles for many engineering purposes.

The potential, ψ, in the diffuse layer around a particle of radius, a, is expressed by the Poisson-Boltzmann equation, which cannot be solved analytically. However, when the Debye-Huckel approximation that ψ is small everywhere z, ψ is given explicitly as follows:

$$\psi = \left(\frac{\psi_d a}{r}\right) \exp[-k(r-a)] \qquad 6.2$$

$$k = \left(\frac{2n_0 z^2 e^2}{\varepsilon kT}\right)^{0.5} \qquad 6.3$$

where r is the distance from the center of the particle, n_0 is the ionic concentration of the bulk solution, and ε is the permitivity of the medium. $1/k$ is a measure of the thickness of the diffuse layer. In the case of particles in an aqueous solution at 25 °C, the thickness of the diffuse layer is given by

$$\frac{1}{k} = 3 \times 10^{-10}\left(z\sqrt{C}\right)^{-1}(m) \qquad 6.4$$

where C is the electrolyte concentration (mol/dm^3). It is clear that the diffuse layer becomes thinner as values of z and C increases [Ada67]. The total charge, Q, of the particle is given by

$$Q = 4\pi\varepsilon a(1 + ka)\psi_d \qquad 6.5$$

DLVO Theory

The terms of Derjaguin and Landau in Russia [Der41] as well as Verwey and Overbeek [Ver48] in the Netherlands independently developed the fundamental criteria for colloidal stability known as DLVO theory. The relationship between the static interaction and particle stability can be explained by employing the interparticle interaction and particle stability by $F_T = -dV_T / dr$, where r is the distance between particles centers. The charge of particles in an aqueous solution makes them repulsive to each other. The repulsive force between similar particles of radius,a, is explicitly given by the following equations, when the surface potential, ψ_d, is sufficiently low ($\psi_d \leq 50$ mV) [Hun87].

$$V_R = 2\pi\varepsilon\psi_d^2 \ln\{1 + \exp[-ka(s-2)]\} \quad (\text{Ka} \geq 10) \qquad 6.6$$

$$V_R = \frac{4\pi\varepsilon\psi_d^2 \exp[-ka(s-2)]}{s} \quad (\text{Ka} \leq 5) \qquad 6.7$$

where ε is the permitivity of the medium; s, the dimensionless distance between particle centers normalized by a; $k = (2n_0)z^2e^2/\varepsilon kT)^{0.5}$; n_0, the ionic concentration of bulk solution; z, the ionic valency; e, the elementary charge; k, the Boltzmann constant; and T, the temperature. K is a measure of the electrolyte concentration.

The instantaneous dipole moment generated by the fluctuation of electrons around

an atomic nucleus polarizes the neighboring atoms and generates the attractive force between atoms. This interaction force is called the dispersion force. Permanent dipoles also generate the interaction force. The sum of these forces is called the van der Waals force. Because the contribution by the permanent dipole is small in most cases, the dispersion force is concerned to be the van der Waals force. Integrating the contribution due to all the atoms in particles, the van der Waals force between spherical particles is given by

$$V_A = \left(\frac{A}{6}\right)\left[\frac{2}{s^2-4} + \frac{2}{s^2}\ln\left(\frac{s^2-4}{s^2}\right)\right] \qquad 6.8$$

where A is the Hamaker constant as described in chapter 4. When particle surfaces are so close that the electron clouds overlap, a very strong Born repulsion force appears. It is said that the Born potential, V_{Born}, is infinitely large when the separation distance is a few angstroms and zero elsewhere. The total interaction potential, V_T, is given by the sum of these potentials:

$$V_T = V_R + V_A + V_{Born} \qquad 6.9$$

Electrophoresis and Streaming Potential

When an external electric field is applied to a suspension, charged particles will migrate toward the electrode of the opposite sign. This phenomenon is called electrophoresis [Sha69]. Measurements of the electrophoretic velocity of particles give information about their surface potential. When a particle undergoes electrophoresis, a thin layer of liquid around the Stern layer moves with the particles as if it is fixed on the

particle surface. The outer surface of this layer is called the slipping plane, and the potential there is called the zeta-potential as shown in Figure 6.1. Hence, the zeta-potential can be correlated with the electrophoretic velocity of particles. According to Henry, the electrophoretic velocity, u_E, of spherical and cylindrical particles is given as a function of the zeta-potential, ζ, as follows [Hen31]:

$$u_E = \frac{u_\infty}{E} = \frac{2\varepsilon\zeta f(ka, K)}{3\mu} \qquad 6.10$$

where u_∞ is the velocity of particles, E is the intensity of the external electric field, u is the velocity of the medium, a is the particle or cylinder radius, K is λ_p/λ_0 where λ_p and λ_0 are the electric conductivities of the particle and the medium. Respectively, and $f(ka, K)$ is the Henry function. When the particle is a nonconducting sphere ($K = 0$) and $ka \gg 1$, $f(ka, K) = 3/2$ and Equation 6.10 results in the so-called Smoluchowski equation [Smo05]. This equation is applicable to nonspherical particles also:

$$u_E = \frac{\varepsilon\zeta}{\mu} \qquad 6.11$$

If $K = 0$ and $ka \ll 1$, Equation 6.11 coincides with the Huckel equation [Huc24], where $f(ka, K) = 1$:

$$u_E = \frac{2\varepsilon\zeta}{3\mu} \qquad 6.12$$

When the double layer around a particle is relatively thick ($0.1 < ka < 100$) and the surface potential is high, the double layer cannot follow the particle migration, and the

double layer will be distorted. This distortion will decelerate the migration velocity of particles. This is called the relaxation effect. The expression of u_E, in which the relaxation effect is taken into account, is given by [Ove43]

$$u_E = \frac{2\varepsilon\zeta f(ka,\zeta)}{3\mu} \qquad 6.13$$

Equation 6.13 is valid only at relatively low zeta-potential.

The electrophoretic velocity for particles of arbitrary shape is given by the Smoluchowski equation if $ka \rangle\rangle 1$, and by the following equation on the case of $ka \langle\langle 1$:

$$u_E = \frac{Q}{f_h} \qquad 6.14$$

where f_h is the hydrodynamic friction factor. Stigter calculated the electrophoretic velocity of cylinderical particles in which the relaxation effect is taken into account [Sti78]. Figure 6.2 shows a schematic diagram of the setup of electrophoresis measurement of the particles. The principle of the streaming potential is similar to that of electrophoretic method. An electrolyte solution is forced through a capillary system. The streaming potential, u_p, resulting from the motion of ions quantitatively relates with the capillaries' zeta-potential as follows:

$$u_p = \frac{\zeta\varepsilon\varepsilon_0 QR\Delta P}{\eta L} \qquad 6.15$$

and

$$\zeta = \frac{u_p \eta L}{\Delta P \varepsilon \varepsilon_0 Q R} \qquad 6.16$$

where ε and ε_0 are permittivity of the test solution and free space, respectively. η is the dynamic viscosity of solution and R is the electrical resistance. Q and L are the cross-section and length of capillaries, respectively. ΔP is the pressure difference between inlet and outlet of capillary system. The schematic diagram of the setup of streaming potential measurement is shown in Figure 6.3.

Experimental

The porous silica particles of 200 nm in diameter with the surface porosity of 57% were synthesized as explained in chaper 3 and the nonporous silica particles of 200 nm in diameter were purchased from Geltec Co. with the same particle size as that of porous one. The bare silicon, thermal oxide (600 nm) and TEOS (1.5 μm) coated silicon and silicon nitride (110 nm) deposited wafers were used as substrates. Each substrate was cut into 5 cm × 15 cm for the streaming potential measurements and pre-cleaned before the measurements. All substrates were cleaned in the mixture of H_2SO_4 and H_2O_2 with the ratio of 4:1 between them followed by HF treatment and finally rinsed with high purity deionized (DI) water. The zeta-potentials of slurry particles and substrates have been measured by electrophoretic method and by streaming potential method, respectively, to evaluate the electrical properties of surfaces, by using a Electrokinetic Analyzer (EKA) of Anton Paar Co. The zeta-potentials of particles and substrates were measured in 10^{-3} M *KCl* and 10^{-2} M *NaCl* solutions as a function of pH, respectively. pH was controlled with *HCl* and *NaOH*.

Results and Discussion

Zeta-potentials of Particles and Substrates

The zeta-potential of slurry particles was measured by the electrophoretic method. Figure 6.4 shows the zeta-potentials of both nonporous and porous silica particles. Nonporous silica showed a higher zeta-potential values in all pH ranges of 3 through 11 compared to 57% porous silica particles but both particles do not show the isoelectric point (IEP) at which the net charge and electrophoretic mobility is zero. IEP of them may be below pH 3. At pH 3 the zeta-potentials of nonporous silica and porous silica were around -4.6 mV and -15.6 mV, respectively, whereas at pH 11 those of them were -25.1 mV and -53.2 mV, respectively. It indicates that the deviation of the zeta-potentials between nonporous silica particles and porous silica particles increases as the pH increases due to different dissolution rate between them at high pH range. It is clear that the porous silica particle causes higher surface charge since it has higher surface area compared to nonporous one. Figure 6.5 shows the zeta-potentials of the silicon, TEOS, and silicon nitride wafer surfaces which were measured by streaming potential method.. Only silicon nitride wafer surface shows the IEP around pH 5.3 while the rest of them do not show their IEPs in given pH ranges. At pH 3, the zeta-potentials of silicon, TEOS, and silicon nitride wafer surfaces shows -9.7 mV, -22.4 mV, and 34.4 mV, respectively, indicating that the zeta-potentials of both silicon and TEOS wafer surfaces are close to those of silicon and TEOS particles even though they are a slightly shift to lower negative potentials in all pH ranges. The deviation of the zeta-potentials between silicon and TEOS wafer surfaces is decreased as the pH increases. Table 6.1 represents the zeta-potentials of both particles and substrates measured by the electrophoretic and streaming potential methods, respectively.

As a consequence, all particles and both silicon and TEOS wafers surfaces do not show their IEP in the pH ranges of 3 through 11 indicating that they are strongly negatively charged in given pH ranges resulting in high repulsive force between them. It is predicted that the interaction between silica particles and silicon or TEOS wafer surface may be predominated by the repulsive force in all pH ranges above 3 due to the same surface charges, whereas that between silica particles and silicon nitride surface may present both the attractive force below pH 5.3, which is IEP of silicon nitride wafer surface, and the repulsive force above pH 5.3 due to the same surface charges between them. It indicates that the optimized pH range should be chosen carefully when the interaction between the slurry particles and the wafer surface to be polished in CMP performance is considered to control simultaneously the polishing rate and surface defects.

Table 6.1 Zeta potentials of the slurry particles and wafers.

	Zeta-Potential (mV)				
pH	Nonporous SiO_2	57 % Porous SiO_2	Si Wafer	TEOS Wafer	Si_3N_4 Wafer
3	-4.6	-15.2	-9.7	-22.4	34.4
7	-18.2	-35.6	-38.1	-62.4	-11.7
11	-25.1	-53.2	-57.5	-67.4	-41.2

Calculation of DLVO Energy

DLVO theory estimates the repulsive and attractive forces due to the overlap of electric double layers and London-van der Waals force in terms of inter particle distance, respectively. The summation of them gives the total interaction force and can be used for the interpretation of colloidal stability in terms of the nature of interaction force-distance curve. If a small interparticle separation, *H*, is assumed, van der Waals force for a sphere and substrate can be expressed as shown in Equation 4.11. However, if we consider the specific circumstance of the interaction between a spherical particle and flat

substrates in an aqueous solution, the Hamaker constant should be used as A_{132} and van der Waals force can be expressed as follows:

$$V_A = -A_{132}R / 6H \qquad 6.17$$

where, A_{132} is the Hamaker constant of two bodies 1 and 2 in dispersion medium 3 and calculated based on A_{11} value and R is the radius of a sphere. The Hamaker constants is generally defined as expressed in Equation 4.12 but that of unknown metals can be calculated based on their definition as shown below:

$$A_{11} = \pi^2 n^2 C_1 \qquad 6.18$$

where n is the number of atoms per unit volume, C_1 is $(3/4)hv_0\alpha^2$, hv_0 is ionization potential and α is polarizability [Old94]. Hamaker constants used for this study are summarized in Table 6.2. The Hamaker constants of both nonporous silica and 57% porous silica particles were calculated by measuring the refractive indices and dielectric constants as explained in chapter 4, whereas those of substrates were obtained from the reference book [Pal91].

Table 6.2 Hamaker constants of the slurry particles and wafers.

Sample	Hamaker Constant (10^{-20} J)
Nonporous SiO_2 Particle	0.67
57 % Porous SiO_2 Particle	0.26
Si Wafer	0.48
TEOS Wafer	0.83
Si_3N_4 Wafer	7.0

The calculation of interaction energy due to the overlapping of the diffuse double layer between two surfaces is complex. It must rely on numerical solutions or various approximations. Generally, Debye-Huckel (D-H) low potential approximation has been

widely used to interpret the interaction between the particle and the substrate by assuming that the particle and flat surfaces interact as two particles with different diameter. D-H low potential approximation is only applicable when the surface potential is less than 25 mV. The silicon nitride wafer surface showed the zeta-potential larger than 25 mV at low pH so that we do not use D-H low potential approximation and rather use the Overbeek's approximation in the derivation of interaction energy. The expression of diffused double layer interaction energy for unequal spherical particles in Overbeek's approximation can be written as:

$$V_R = \frac{64\pi\varepsilon a_1 k^2 T^2 \gamma_1 \gamma_2}{(a_1 + a_2)e^2 z^2} \exp[-kT] \qquad 6.19$$

where z is the counter-ion charge number, a_1 and a_2 are particle radius, k is $(8\pi n v^2 e^2/\varepsilon kT)^{0.5}$ and

$$\gamma = \frac{\exp[ze\psi_d / 2kT] - 1}{\exp[ze\psi_d / 2kT] + 1} \qquad 6.20$$

The total interaction energies of the combinations of two silica particles and three substrate surfaces were calculated using zeta-potentials of both slurry particles and substrates measured based on Overbeek's approaximation at pHs of 3, 7, and 11. Figure 6.6 shows total DLVO energy constant potential between nonporous silica particle surface and silicon wafer surface at different pHs as a function of separation distance. It presents that the nonporous silica particle-silicon wafer surface interaction energy increases as pH increases due to strong negative charges of two surfaces at high pH

ranges indicating that the repulsive force is predominant at high pH when the surface charges of two bodies are close. Figure 6.7 also shows the electrostatic force between them. At pH 3 the slop of the repulsive force curve is almost zero, whereas it increases with increasing pH. It indicates that at low pH nonporous silica particle and silicon wafer have very weak negatively charged surfaces of -4.6 and -9.7, respectively, as show in Table 6.1. This phenomena also was observed in a case of 57% porous silica particle-silicon wafer surface interaction as shown in Figures 6.8 and 6.9 for DLVO potential energy and electrostatic repulsive force, respectively, since the zeta-potential of nonporous silica particles is similar to that of porous silica particles especially at low pH even though the former is a slightly shift to higher than the latter. The trend of DLVO energy and electrostatic repulsive force between nonporous silica particle and TEOS is similar to that of nonporous silica particle-silicon wafer surface interaction and to that of 57% porous silica particle-TEOS wafer surface interaction as shown in Figures 6.10 through 6.13. It is noted that the same surface charges of two different bodies result in high total potential energy and repulsive force and they increase as pH increases due to a large deviation of the zeta-potentials of two surfaces, which have the same surface charges, at high pH ranges.

However, the silica particle-silicon nitride wafer surface interaction presents the different trends of total potential energy and repulsive force depending on pH range. Figure 6.14 shows the total DLVO potential energies of nonporous silica particle-silicon nitride surface interaction at different pH ranges as a function of separation distance. At pH 3, the silica-silicon nitride interaction is predominated by the attractive force when they are close. It indicates that the surface charges of two different bodies, nonporous silica particle and silicon nitride wafer, are opposite each other at this pH resulting in a

strong attraction as the separation distance decreases. Table 6.2 shows the zeta-potential values of both nonporous silica particle and silicon nitride wafer as -4.6 mV and 34.4 mV at pH 3 and -25.1 mV and -41.2 mV at pH 11, respectively. It is clear that the silica particle approaches the silicon nitride surface due to the van der Waals force caused by opposite charges between two surfaces at pH 3, whereas the silicon nitride surface starts repelling the silica particles at high pH from 5.3, which is an IEP of silicon nitride surface, since the surface charges of both silica particle and silicon nitride wafer become similar as pH increases. Figure 6.15 also shows the same trend of nonporous silica particle-silicon nitride wafer surface interaction in terms of the electrostatic repulsive force. It clearly presents the pH-dependent repulsive force between two surfaces, which are opposite charges each other. Figures 6.16 and 6.17 show the total potential energy and repulsive force of 57% porous silica particle-silicon nitride wafer surface interaction at different pH ranges resulting in the same phenomena as in nonporous case with silicon nitride wafer surface even though the degree of the slopes of each curve in porous silica-silicon nitride interaction is a slightly shift to higher than those in nonporous silica-silicon nitride interaction.

As a result, the interaction between two different surfaces are highly dependent of their surface charges leading to either the attractive force or repulsive force. The degree of the deviation of zeta-potentials of two surfaces having the same sign of the surface charge can determine the slope of total DLVO energy and electrostatic repulsive force curves at a short separation distance where two surface are close each other.

Effect of the Surface Porosity on Repulsive Force

To investigate the effect of the surface porosity of slurry particles on the interaction force with wafer surfaces, two different silica particles such as nonporous and

57% porous silica particles but the same particle size of 200 nm in diameter were used in this study. Figure 6.18 shows the electrostatic forces between nanoporous silica particle surface and the wafer surfaces of silicon, TEOS, and silicon nitride at pH 3 as a function of separation distance. At pH 3 the zeta-potential of nonporous silica particle was -4.6 mV while that of substrates, silicon, TEOS, and silicon nitride, was -9.7 MV, -22.4 mV, and 34.4 mV, respectively, as shown in Table 6.1. It results in the variation of nonporous silica particle-substrate surface interaction in terms of the electrostatic force as shown in Figure 6.18. Only silica-silicon nitride interaction showed the attractive force from a short separation distance around 100 nm since they have opposite signs of zeta-potentials at pH 3, whereas silica and both silicon and TEOS interactions presented the repulsive forces due to the same signs of zeta-potential between them.

The zeta-potential of 57% porous silica particle is -15.2 mV which is similar but a slightly shift to lower than that of nonporous one resulting in small deviation from the zeta-potentials of substrates. The magnitude of the zeta-potential also influences the degree of interaction force indicating that the same magnitudes of the zeta-potentials with the same signs may cause the strong repulsive force and the same magnitudes of the zeta-potentials with opposite signs may result in the strong attractive force. Figure 6.19 shows the 57% porous silica particle-substrate surface interaction at pH 3. The comparison between nonporous silica and porous silica particles in terms of the electrostatic force is shown in Figure 6.20. It is noted that the surface porosity of slurry particles influences the total interaction energy and force. In the silica particle-TEOS surface interaction the repulsive forces are predominant for both nonporous and porous silica particles but the porous silica particle-TEOS interaction showed stronger repulsive force than nonporous silica particle-TEOS interaction. However, for the case of silicon nitride wafer surface

the porous silica particle-silicon nitride interaction showed stronger attractive force than nonporous silica-silicon nitride interaction as show in Figure 6.20. This is because the deviation of the zeta-potential between silica particles and TEOS surface is small for porous silica particle compared to nonporous silica particle resulting in the presentation of strong repulsive force in porous silica particle-TEOS surface interaction, whereas the deviation of the zeta-potential between silica particles and silicon nitride surface is larger in porous silica particle-silicon nitride surface than in nonporous silica particle-silicon nitride surface leading to strong attractive force in porous silica case compared to nonporous one. It is not exactly agreed with the result of the direct force measurement of silicon nitride tip-porous silica particle surface, which was conducted in chapter 5, since there are several different parameters influencing the result of interaction force between them.

As a consequence, the surface porosity of the slurry particles affects the interaction force between slurry particles and wafer surfaces depending on the sign and magnitude of their zeta-potentials caused by the pH-dependent surface charge. In the silica-silica interaction the porous slurry particles lead to large repulsive force, whereas in the silica-silicon nitride interaction it results in strong attractive force at low pH, which may be observed in low k or STI CMP process.

Summary

Zeta-potentials of slurry particles and wafer surfaces were measured to calculate the DLVO total interaction energy between them at various pHs. Instead of the Debye-Huckel low potential approximation, Overbeek's approximation was applied to the calculation. The electrostatic force was calculated for the combined systems of two silica

particles and three wafer surfaces to investigate the effects of the zeta-potential and surface porosity of slurry particles.

The interaction force between slurry abrasives and wafer surface during CMP may be mainly determined by van der Waals attractive and/or electrostatic repulsive force. Even though van der Waals force is inherent in materials, the electrostatic force is strongly dependent on the surface potential which are strongly dependent on the pH of solutions. The surface potentials of particles and wafer surfaces in an aqueous solution can be expressed in terms of zeta-potentials. If the sign of potentials of two interacting surfaces are the same, there is a net repulsion between two surfaces and vice versa depending on the magnitude of van der Waals force.

DLVO theory can be used to calculate the interaction forces between the slurry particle and the wafer surface to be polished. The interaction forces between the particles and wafer surfaces could provide important information on the stability of slurry and the degree of particle contamination on surfaces after CMP.

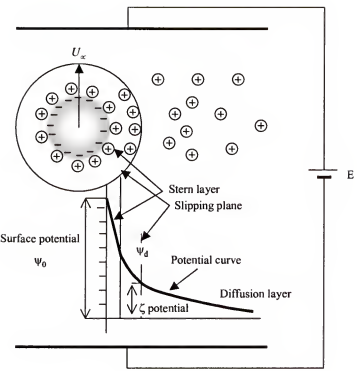

Figure 6-1 A schematic diagram of electrochemical double layer around particle surface in an applied electric field [Mye99].

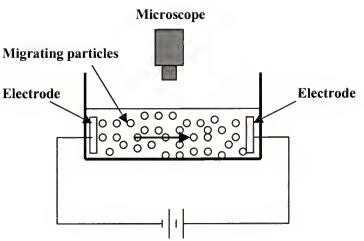

Figure 6-2 A schematic diagram of the setup of Electrophoresis measurement of the particles [Sha69].

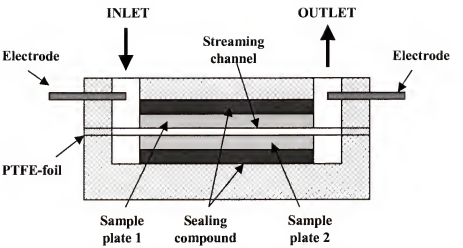

Figure 6-3 A schematic diagram of the setup of Streaming potential measurement [Sha69].

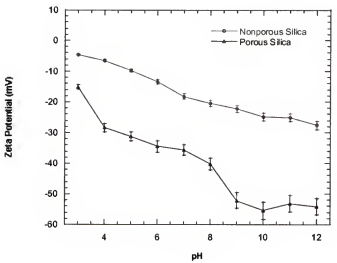

Figure 6-4 Zeta-potentials of nonporous and 57 % porous silica particles as a function of pH.

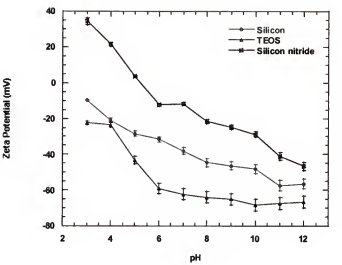

Figure 6-5 Zeta-potentials of silicon, TEOS and silicon nitride wafers as a function of pH.

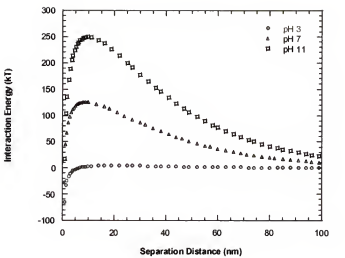

Figure 6-6 Total DLVO energy constant potential between nonporous silica particle surface and silicon wafer surface at different pHs as a function of separation distance.

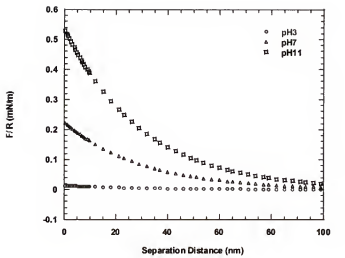

Figure 6-7 The electrostatic force between nonporous silica particle surface and silicon wafer surface at different pHs as a function of separation distance.

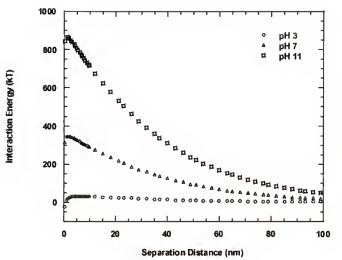

Figure 6-8 Total DLVO energy constant potential between 57% porous silica particle surface and silicon wafer surface at different pHs as a function of separation distance.

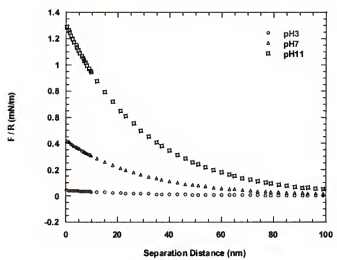

Figure 6-9 The electrostatic force between 57% porous silica particle surface and silicon wafer surface at different pHs as a function of separation distance.

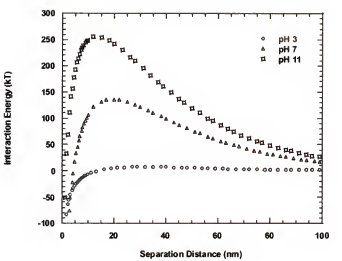

Figure 6-10 Total DLVO energy constant potential between nonporous silica particle surface and TEOS surface at different pHs as a function of separation distance.

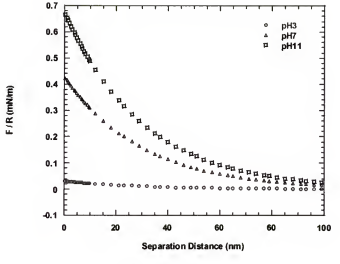

Figure 6-11 The electrostatic force between nonporous silica particle surface and TEOS surface at different pHs as a function of separation distance.

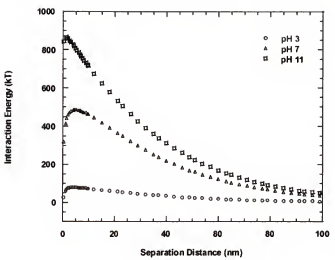

Figure 6-12 Total DLVO energy constant potential between nanoporous silica particle surface and TEOS surface at different pHs as a function of separation distance.

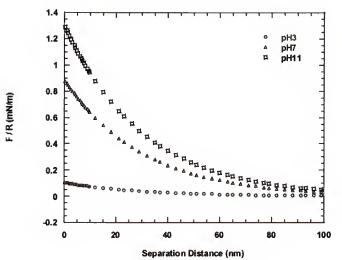

Figure 6-13 The electrostatic force between nanoporous silica particle surface and TEOS surface at different pHs as a function of separation distance.

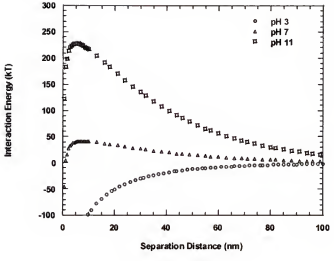

Figure 6-14 Total DLVO energy constant potential between nonporous silica particle surface and silicon nitride wafer surface at different pHs as a function of separation distance.

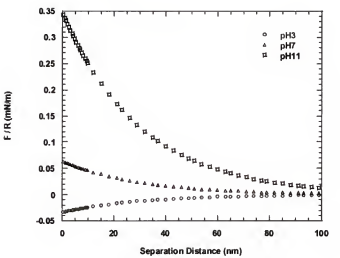

Figure 6-15 The electrostatic force between nonporous silica particle surface and silicon nitride wafer surface at different pHs as a function of separation distance.

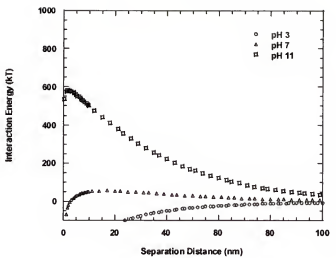

Figure 6-16 Total DLVO energy constant potential between nanoporous silica particle surface and silicon nitride wafer surface at different pHs as a function of separation distance.

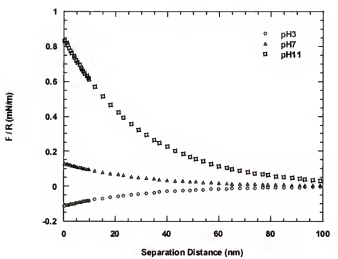

Figure 6-17 The electrostatic force between nanoporous silica particle surface and silicon nitride wafer surface at different pHs as a function of separation distance.

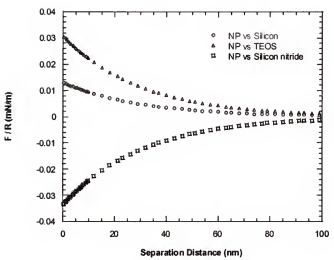

Figure 6-18 The electrostatic forces between nanoporous silica particle surface and the wafer surfaces of silicon, TEOS, and silicon nitride at pH 3 as a function of separation distance.

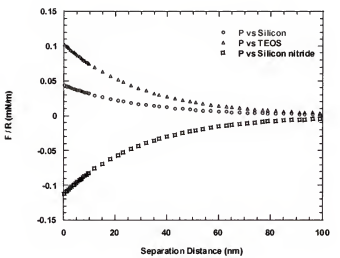

Figure 6-19 The electrostatic forces between 57% porous silica particle surface and the wafer surfaces of silicon, TEOS, and silicon nitride at pH 3 as a function of separation distance.

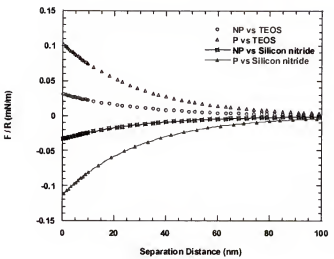

Figure 6-20 The comparison of the electrostatic forces between nonporous silica and 57% porous silica particles interacting with the wafer surfaces of silicon, TEOS, and silicon nitride at pH 3 as a function of separation distance.

CHAPTER 7
MECHANICAL PROPERTIES OF NANOPOROUS SILICA PARTICLES

Introduction

We have studied the properties of the porous silica particles by comparing to nonporous silica particles in previous chapters. It has been revealed that the porous silica particle has lower density due to large number of the surface pores resulting in lower value of the Hamaker constant, which leads to lower van der Waals force in the slurry particle-substrate interaction. However, it is also known that the hardness of the slurry particles influences the CMP performance in terms of the material removal rate and surface quality of polished wafer. The wafer surface to be polished in CMP process is typically much softer than the slurry abrasive particles so that the CMP of soft surfaces using the conventional slurry particles results in a high degree of surface defects such as microscratches, pits, craters, and the like, as described in chapter 2. The penetration depth of polished wafer surface varies linearly with the particle size and inversely with the Young's modulus of the impacting particle as shown in Equation 2.11. Thus, to reduce the depth of the particle indent and resulting scratches, the particle size as well as the Young's Modulus of the particle should be reduced [Hie97].

The soft hydrated layer caused in an aqueous CMP slurry affects polishing since it is easier to remove than the bulk material [Kal92]. An abrasive that is softer than the bulk material could conceivably remove material from a hydrated layer, but a harder

particle under the same load could penetrate farther into the layer resulting in more material removal, which may cause more surface defects. Kaller discussed both the importance of finding the unknown hardness of abrasive particles and how the abrasive should actually be softer than the material being polished [Kal92]. An important experiment would be to compare the hardness of the slurry particles influencing both the removal rate and surface quality of material being polished. For this experiment to be of the greatest utility the actual hardness of the particle must be known.

In this study, the mechanical properties of nanoporous silica particles such as the hardness and elastic modulus were measured using the nanoindentation technique of AFM as a function of the surface porosity. The effect of the surface porosity of silica particles on the particle hardness is discussed in detail.

Nanoindentation Technique

Measurement and theory of hardness testing have been developed in the field of material testing, where it has been possible to carry out hardness tests on large specimens. Until very recently, it has been difficult to characterize the hardness of small particles. However, with rapid progress in the past decade in the field of nanotesting and atomic force microscopy, detailed characterization of surfaces of even micrometer sized particles is now possible.

The measurement of hardness started with scratch testing of flat surfaces by various particles having varying degree of hardness. This method provided a quantitative indentation of resistance to plastic flow, but it was too complex for analysis to obtain quantitative results. The method of indentation hardness testing evolved by the use of well-defined indenter geometry, such as spherical, pyramidal or conical shapes. Tabor's pioneering work established the basis of understanding of the deformation processes

involved in the indentation [Tab48]. There are a number of common test methods available using different indenter shapes: Brinell, using a 10-μm sphere of steel or tungsten carbide; Vickers, using a diamond pyramid, and Rockwell, using a diamond cone with spherical tip and steel spheres. In all these tests, a load is applied to the surface under testing by slowly penetrating the indenter at a right angle onto the specimen. The hardness number is calculated from the applied load and the projected area of the impression, and by taking account of the shape of the indenter. The relevant formula for hardness numbers may be found for example from the work of Tabor [Tab70].

The above techniques can not be applied easily to the measurement of hardness of particles unless the particle is large above few millimeter. However, the recent development of nanotest methods has enabled a full characterization of mechanical properties as well as topography of fine particulate solids. Because of the small size of impression, which can be submicrometer, almost all nanoindentation methods measure the resistance of material to penetration (applied load) as a function of depth of penetration, from which an "effective" hardness can be inferred.

The device measures the movement of a calibrated diamond indenter penetrating a specimen surface at a controlled loading rate. It uses a pendulum pivoted on bearings which are essentially frictionless. A coil is mounted at the top of the pendulum so that when a coil current is present, the soil is attracted toward a permanent magnet, producing motion of the indenter toward the specimen and into the specimen surface. The displacement of the diamond is measured by means of a parallel-plate capacitor, one plate of which is attached to the diamond holder; when the diamond moves, the capacitance changes, and this change is measured by means of a capacitance bridge. The most commonly used indenter is a Berkovich diamond, a three-sided pyramid, which is

particularly suitable for nanoindentation work because it can be machined down very accurately to a very sharp tip. However, 90° trigonal and spherical indenters have also been used. The nanotest devices are typically capable of resolutions of the order of 10 μN and 0.1 nm for the load and displacement, respectively.

In a nanoindentation test, the specimen is first brought into contact with the indenter; then the load is increased at a prescribed rate until the desired maximum load is reached, and then it is decreased back to zero at the same rate. Therefore, a continuous recording of the penetration depth and the applied load is made, from which an effective hardness may be inferred at a specified strain rate by invoking a relation between the penetration depth and the indentation area. During the unloading part of the cycle, elastic deformation of the sample will recover; therefore the unloading curve is not horizontal. The maximum depth and characteristics of the unloading curve are used to calculate the hardness. However, it is also possible to evaluate the elastic modulus from the unloading curve. Two distinct regions can be observed : the initial unloading stage bearing all the features of an elastic unloading, and a highly unloading stage toward the end of unloading cycle. Reasons for this nonlinearity are complex; changes in the contact area arising from an increase in the apical angle of the impression are thought to be responsible. There are several methods for the evaluation of hardness from such data. The method described below is based on the analysis of Oliver and Pharr [Oli92, Pha92].

Figure 7.1 shows a schematic diagram of load-displacement curve. At the initiation of unloading, the elastic component of the deformation starts to recover so that contact between the material surface and the indenter is still maintained. As the load is decreased, the elastic displacement continues to recover until, at zero load, the displacement reaches a final value, h_f. At the peak load, F_{max}, the displacement is h_{max}.

The total displacement, h, can be described at any time during loading, as

$$h = h_c + h_s \tag{7.1}$$

where h_c is the contact depth corresponding to the contact size, a, and h_s is the elastic displacement of the surface at the perimeter of the contact. In this analysis, the hardness, H, can be determined by

$$H = \frac{F_{\max}}{A} \tag{7.2}$$

where A is the projected area of the impression. Now, from the geometry of the indenter,

$$A = kh_{c,\max}^2 \tag{7.3}$$

with k being the indenter shape factor, and $h_{c,\max}$ is the contact depth at $F_{\max}$. Now, to determine the contact depth from the experimental data, it can be noted that

$$h_{c,\max} = h_{\max} - h_{s,\max} \tag{7.4}$$

$h_{\max}$. is experimentally measured, and $h_{s,\max}$ can be ascertained from the unloading data by the use of an expression derived by Oliver and Phar from Sneddon's solution for the elastic contact of indenters of different shapes [Pha92, Sne65]. This equation is given by

$$h_{s,\max} = k\frac{F_{\max}}{S} \tag{7.5}$$

where S is the stiffness at load $F_{\max}$ and k is a constant which depends on indenter geometry. The value of k for a Berkovich indenter cannot be determined analytically; however, it has been shown that the Berkovich indenter behaves very much like a paraboloid of revolution for which a solution for the parameter k exists ($k = 0.75$).

In practice, the stiffness, S, is obtained by fitting the unloading data to a power-low relation of the form

$$F = \alpha\left(h - h_f\right)^m \qquad 7.6$$

where $(h\text{-}h_f)$ is the elastic displacement of the indentation during unloading; α and m are constants. The values of α, m, and h_f are all determined by a nonlinear curve fitting procedure. Equation 7.6 can then be differentiated analytically with respect to $(h\text{-}h_f)$ to obtain the value of stiffness:

$$S = \frac{dF}{d(h - h_f)} \qquad 7.7$$

which can then be evaluated at the peak load, F_{max}. Then, by first substituting the value of stiffness obtained from Equation 7.7 into Equation 7.5, the value of $h_{s,max}$ is calculated. Equations 7.4, 7.3, and 7.2 are then used to determine the hardness.

The Young's modulus can also be determined from the unloading portion of the depth-load data by the use of Sneddon's analusis. This analysis is independent of indenter geometry and is therefore applicable to results obtained with the Berkovitch indenter:

$$E_r = \frac{\sqrt{\pi}}{2}\frac{S}{\sqrt{A}} \qquad 7.8$$

where S is calculated from Equation 7.7, A is the contact area given by Equation 7.3, and E_r is the reduced modulus defined by

$$\frac{1}{E_r} = \frac{1-\nu^2}{E} + \frac{1-\nu_i^2}{E_i} \qquad 7.9$$

where E and ν are the Young's modulus and Poisson's ratio of the specimen, and E_i and ν_i are the same parameters for the diamond indenter. Because the young's modulus of the indenter is two orders of magnitude greater than that of the test materials, the reduced modulus is effectively the Young's modulus of the specimen. In conclusion, the above approach enables the determination of hardness and Young's modulus at the nanoscale level. However, great care is needed for the experimental procedure and interpretation of the data because of the scale of operation.

An indentation curve is the relationship between load, F, and displacement (or indentation depth or penetration depth), h, which is continuously monitored and recorded during indentation. Stress-strain curves, typical indentation curves, the deformed surfaces after tip removal, and residual impression of indentation for ideal elastic, rigid-perfectly plastic and elastic-perfectly plastic and real elastic-plastic solids are shown in Figure 7.2. For an elastic solid, the sample deforms elastically according to Young's modulus, and the deformation is recovered during unloading. As a result, there is no impression of the indentation after unloading. For a rigid-perfectly plastic solid, no deformation occurs until yield stress is reached, when plastic flow takes place. There is no recovery during and the impression remains unchanged. In the case of elastic-plastic solid, it deforms elastically according to Young's modulus and then it deforms plastically. The elastic deformation is recovered during unloading. In the case of an elastic-perfectly plastic solid, there is no work hardening.

Based on the work of Sneddon to predict the deflection of the surface at the

contact perimeter for a conical indenter and a paraboloid of revolution, Oliver and Pharr developed an expression for h_c at the maximum load from h_{max} (Figure 7.1), as described in Equation 7.4 [Pha92].

$$h_c = h_{\max} - \varepsilon F_{\max} / S_{\max} \qquad 7.10$$

where $\varepsilon = 0.72$ for the conical indenter, $\varepsilon = 0.75$ for the paraboloid of revolution, and $\varepsilon = 1$ for the flat punch; S_{max} is the stiffness (= 1/compliance) equal to the slope of unloading curve (dF/dh) at the maximum load [Pha92]. Oliver and Pharr assumed that behavior of Berkovich indenter is simple to that of conical indenter, since cross-sectional areas of both types of indenters varies as the square of the contact depth larger than plastic indentation depth (h_p), which is given by

$$h_p = h_{\max} - F_{\max} / S_{\max} \qquad 7.11$$

It is noted that Doerner and Nix had underestimated h_c by assuming that $h_c = h_p$ [Doe86]. Based on the finite element analysis of the indentation process, Laursen and Simo showed that h_c cannot be assumed equal to h_p for indenters which do not have flat punch geometry [Lau92]. Since the area-to-depth relationship is equivalent for both typical Berkovich and Vickers pyramids. For the real indenter used in the measurements, the normal shape described in Equation 7.3 can be expressed by an area function $F(h_c)$, which relates projected contact area of the indenter to the contact depth.

$$A^{1/2} = F\left(h_c\right) \qquad 7.12$$

The functional form must be established experimentally prior to the analysis.

Experimental

Sample Preparation for Abrasive Particles

The silica particles of 200 nm in diameter with a variation of the surface porosity, which are described in chapter 3, were used for the nanoindentation measurements to investigate the mechanical properties of the particles. The heat treatment and pressure may change the particle properties. To maintain the original properties of particles, the BUEHLER sample-kwick cold mounting material (Lake Bluff, IL) combined of polymeric powder and liquid solution was employed for the sample preparation. The porous silica particles were mixed with cold mounting powders in a ratio of about 1 to 10. The liquid hardener was added into the mixtures and then stirred for the uniform dispersion of silica particles. This gel-like mixtures were put into 0.25 inch diameter glass cylinder of 0.5 cm height and then left in the room temperature for 2 hours. The glass cylinder was broken by a small stick and the hard sample was then polished until several silica particles are exposed. It was assumed that this process do not change the particle properties. Figure 7.3 shows SEM micrographs of polished silica nanoparticle surfaces embedded into cold mounting polymer materials.

The indenter was a pyramidal Berkovich diamond being shown in Figure 7.4 that accommodates maximum loads up to about 700 mN and both 25 and 50 μN were applied to this experiment as a maximum load. This instrument applies a load by magnetic coil and the displacement of the indenter is continuously measured with a capacitance gauge. The displacement can be measured to within ± 0.04 nm and the output voltage from the loading operation to within 4 μV. The loads and displacement error was much less than 1 %.

Calibration and validation test were conducted to have a way to verify that

indentations are actually being placed on an individual particle. Figure 7.5 shows the calibration profile for 20 seconds with 25 and 50 μN. The validation test was set up to put an initial indent in the center of the particle and follow it with four more indents spaced 2 μm apart. The sample thickness should be four or ten times larger than the depth of an indent. Also, indents should be more than two times the size of any "stress deformation" that results from indentation. This prevents deformation due to neighboring indents from interacting. Most indents were approximately large for these loads. If the particles are particularly small, it might be advantageous to make arrays of indents. In this case, care must be taken to identify valid indents from invalid ones.

The nanoindenter's computer-automated system allows the user to choose the indentation experiment (loading rate, maximum load, drift correction, etc.) and location of the indent, leaving the instrument unattended as the experiment is performed. A typical experiment takes only about 15 min, but the time depends on the environment where the nanoindenter is located and the number of indents made. The first part of a test requires that the instrument settle to a user-specified ctritical drift rate. The indenter is kept in an insulated cabinet on a vibration isolation table. If the room containing the instrument has significant vibrations or temperature gradient, it may take some time for the drift rate to settle to the user-selected value. Our tests utilize the default critical drift rate of 0.05 nm/s.

Results and Discussion

Effect of the Surface Porosity on Contact Depth

The nanoindentation experiments of nanoporous silica particles embedded in the cold mounting polymeric materials, of various porosities (2.8%, 4.6%, 6.9%, 13.9%, 22.2%, 32.3%, 36.15, and 57.6%) but with approximately the same particle size of about

200 nm, were carried out using Nano Indenter II in the applied loads of 25 and 50 μN. Care was taken to ensure that the indentation response is solely that of the particle, with the deformation field of indentation confined fully within the silica particle surfaces, and that the results interpreted from such experiments are not influenced by the specific tip radius of the indenter. In this experiment a diamond Berkovich type indenter tip was forced into the material being studied under continuous conditions. The indentation depth is related to the area of contact between the indenter and the material under test. This procedure allowed the mechanical properties of the tested material to calculate the hardness and the Young's modulus. This was done by making the indentation with a well-controlled force, F, while continuously monitoring and measuring the displacement, h, of the indenter. During the entire indentation procedure, the continuous measurement of stiffness was accomplished by applying a small oscillation to the displacement signal at relatively high frequency of 45 Hz. The amplitude of the displacement oscillation was kept sufficiently small, in our case 1.5 nm, the deformation process was not affected by its addition.

The corresponding force oscillation was monitored at the excitation frequency using a two-channel phase-sensitive detector. It was thus possible to continuously measure the stiffness, S, of the contact between the specimen and the indenter and to deduce the hardness, H, and Young's modulus, E, of the material based on Equation 7.2 with Equations 7.3, 7.8, and 7.9. The projected area of the impression, A, in Equation 7.3, from the geometry of the indenter was calculated as follows:

$$A = 24.5h_c^2 + 170h_c + 94.89h_c^{0.5} + 0.89h_c^{0.25} \qquad 7.13$$

Different loading sequences were performed on the previously described structures,

where the particle surface is on the substrate. It was found that the cold mounting material has a hardness and elastic modulus of about 0.2 GPa and 3 GPa, respectively. These values are significantly lower than those of the particles being tested, so deformation of the embedding medium is a concern.

Both the hardness and elastic modulus, which are mainly discussed in this study, were calculated via the load-displacement curves. Since the load-displacement curve is of greatest interest, it is important that the particle be constrained from displacing due to the indenter loading from the top. That is, the measured displacement must be due to the motion of the indenter into the particle surface, and due to the motion of the particle. For this reason, the particles were mounted in a polymer substrate.

The load-displacement curves in nanoindentation measurements in 25 and 50 μN and SEM micrograph of porous silica particles indented with 50 μN loading are shown in Figures 7.6 through 7.13 according to the surface porosity. The load-displacement curve represents both the contact depth and the stiffness. All samples indented in 50 μN loading resulted in much deeper contact depth than in 25 μN loading but showed almost same values of the stiffness as in 25 μN loading. The contact depth in both 25 and 50 μN loadings increases as the surface porosity increases resulting in lower stiffness with increasing the surface porosity. Figures 7.14 and 7.15 show the load-displacement curves of both 25 and 50 μN loadings, respectively, presenting the evolution of the contact depth as a function of the surface porosity. As the surface porosity of silica particles increases, the contact depth is increased linearly only at low porous samples less than around 13% in both cases of 25 and 50 μN loadings but almost saturated with a slight increasing at highly porous samples over around 22% indented especially in lower load. Figure 7.16 shows the contact depth of silica particles indented in 25 and 50 μN as a function of the

surface porosity.

As a consequence, the contact depth of silica particles increases very sensitively at lower porous samples with increasing the surface porosity but shows almost constant values with a slight increasing at highly porous samples. It indicates that the nonporous or lower porous silica particles show the elastic-plastic behavior, whereas the highly porous silica particles show the elastic behavior. Regardless of the surface porosity, higher load resulted in a deeper contact depth for all samples.

Contact Stiffness of Nanoporous Silica Particles

Even though during loading a sample undergoes elastic-plastic deformation, the initial unloading is an elastic event. Therefore, the Young's modulus of elasticity or, simply, the elastic modulus of the specimen can be inferred from the initial slope of the unloading curve called stiffness. It should be noted that the contact stiffness is measured only at the maximum load, and no restrictions are placed on the unloading data being linear during any portion of the unloading. Figure 7.17 presents the contact stiffness of each sample as a function of the surface porosity obtained from the load-displacement curves by plotting the slope from the maximum load point. It indicates that the stiffness decreases with increasing the surface porosity. At lower porous samples less than around 13% the stiffness is inversely proportional to the surface porosity, whereas at highly porous samples it is independent of the surface porosity as expected in Figures 7.14 and 7.15. It indicates that the surface porosity does not influence the contact stiffness of highly porous silica particles. The stiffness of each samples conducted in lower loading is overlapped with that in high loading since it is an inverse of compliance of unloading curve indicating that the applied load does not affect the stiffness in all cases. The stiffness decreases abruptly at lower porous samples as the surface porosity increases

while at highly porous samples it does not change as much as does the contact depth of highly porous samples. It is expected that the porous silica particle may present lower hardness compared to nonporous one.

Calculation of Elastic Modulus

If the area in contact remains constant during initial unloading, an approximate elastic modulus is obtained by analyzing a flat punch whose area in contact with the specimen is equal to the projected area of the actual punch. Based on the analysis of indentation of an elastic half-space by a flat cylinderical punch Sneddon and Loubet calculated the elastic deformation of an isotropic elastic material with a flat-ended cylinderical punch [Sne65, Lou84]. They obtained an approximate relationship for compliance (dh/dF) for the Vickers (square) indenter. King solved the problem of flat-ended cylinderical quadrilateral (Vickers and Knoop), and triangular (Berkovich) punches indenting an elastic half-space [Kin87]. He found that the compliance for the indenter is approximately independent of the shape (with a variation of at most 3 %) if the projected area is fixed. Pharr also verified that compliance of a paraboloid of revolution of a smooth function is the same as that of a spherical or a flat-ended cylinderical punch [Pha92]. The relationship for the compliance, C, (inverse of stiffness, S) for an (Vickers, Knoop, and Berkovich) indenter is given as

$$C = \frac{1}{S} = \frac{dh}{dF} \approx \frac{1}{2E_r}\left(\frac{\pi}{A}\right)^{1/2} \qquad 7.14$$

where dF/dh is the slope of the unloading curve at the maximum load. In Equation 7.9, E_r, E, and E_i are the reduced modulus and elastic muduli of the specimen and the indenter, and ν and ν_i are the Poisson's ratios of the specimen and indenter. C (or S) is

the experimentally measured compliance (or stiffness) at the maximum load during unloading, and A is the projected contact area at the maximum load. The contact depth, h_c is related to the projected contact area of the indentation, A, for a real indenter by Equation 7.12. A plot of the measured compliance (dh/dF) vs. the reciprocal of the corrected indentation depth obtained from various indentation curves (one data point at maximum load for each curve) should yield a straight line with slope proportional to $1/E_r$. For a diamond indenter, $E_i = 1140$ GPa and $\nu_i = 0.07$ were given [Pha92]. In addition, the y-intercept of the compliance vs. the reciprocal indentation depth plot should give any additional compliance that is independent of the contact area.

The elastic modulus of nanoporous silica particles was calculated using Equation 7.14 with the contact stiffness and contact area. Figure 7.18 shows the elastic modulus of silica particles as a function of the surface porosity. The trend of this elastic modulus of silica particles is exactly the same as that of the contact stiffness shown in Figure 7.17 since they are proportional to each other although they have different units. The elastic modulus of silica particles decreases with increasing the surface porosity without any deviation between two different loads at lower porosity ranges less than around 20%, whereas at highly porous samples it remains constant with a slight variation.

Calculation of Hardness

It should be pointed out that the hardness measured using this definition may be different from that obtained from the more conventional definition in which the area is determined by direct measurement of the size of the residual hardness impression. The reason for the difference is that, in some materials, a small portion of the contact area under load is not plastically deformed, and, as a result, the contact area measured by observation of the residual hardness impression may be less than that at peak load

[Pha92]. However, it is known that measurements using two techniques give similar results for most materials.

Berkovich hardness HB (or HB) is defined as the load divided by the projected area of the indentation. It is the mean pressure that a material will support under load. From the indentation curve, we obtained the hardness at the maximum load as described in Equation 7.2. The contact area at the peak load was determined by the geometry of the indenter and the corresponding contact depth, h_c using Equation 7.13. SEM micrographs of silica particles indented in 50 μN with various surface porosity are shown in Figures 7.6 through 7.13 according to the surface porosity. Even though the contact area of each sample is not regular shape, it is clear and good enough to be measured. Figure 7.19 shows the contact areas of silica particles measured with each micrograph as a function of the surface porosity. The contact area increases with increasing the surface porosity and a higher load shows a larger contact area. This result agrees with that of the contact depth in terms of the trend of each curve as shown in Figure 7.16. It shows the rapid increase of the contact depth and contact area at only lower porous silica particles with increasing the surface porosity resulting in higher hardness of silica particles. The hardness of each sample calculated using Equation 7.2 with the maximum load applied is shown in Figure 7.20. The 50 μN load shows a slightly lower hardness than 25 μN in all samples but both loads show a different deviation of hardness depending on the surface porosity. This deviation decreases as the surface porosity increases indicating that at highly porous silica particles the hardness is independent of the load being applied. In both cases of applied loads the hardness decreases with increasing the surface porosity. As same as in the contact stiffness the hardness varies rapidly at lower porosity ranges, while it shows almost constant values at highly porous silica particles.

As a result, the surface porosity influences the contact area significantly resulting in lower particle hardness at high porosity ranges. Furthermore, the deviation of the particle hardness depending on the applied load decreases as the surface porosity increases indicating that the highly porous structure is required for the abrasive slurry particles to have lower hardness with a narrow deviation, which is expected to reduce the surface defects in CMP performances.

Summary

The nanoindentation measurements of nanoporous silica particles with a various surface porosities but almost same particle size of 200 nm were carried out to investigate the effect of the surface porosity on the mechanical properties such as the hardness and elastic modulus of the particles. The porous silica particles were mounted using a cold mounting polymer material since the sintering and pressing particles can alternate several properties of the particles.

The analyzing the load-displacement curves obtained this experiment provided several information about the mechanical properties of silica particles. The contact depth increases as the surface porosity increases and as does the applied load. The deviation of the contact depth becomes deeper at highly porous silica particles due to a significant elastic behavior in high porosity ranges. It implies that the porous silica particle has lower density and pore structure resulting in lower contact area and hardness.

The stiffness obtained from the load-displacement curve by plotting the slope from the maximum load point was decreased as the surface porosity increases, which leads to the same trend of elastic modulus since they are proportional to each other. However, the load applied does not affect both the stiffness and elastic modulus.

To calculate the hardness of nanoporous silica particles the contact area was

measured from the micrographs of silica particles indented. The contact area increases linearly with the surface porosity in lower porosity ranges but maintains constant values at high porosity ranges, where result in very low and uniform hardness of the particles. The deviation of the hardness of particles between two different loads depends on the surface porosity but leads to very uniform values of hardness at high porosity ranges.

As a consequence, the results of this experiment revealed that the nanoporous silica particle can be a good candidate as an abrasive slurry particle which can reduce the surface defects of polished surface since it has lower values of hardness with very narrow deviation.

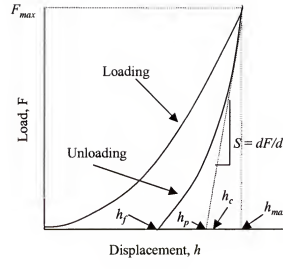

Figure 7-1 Schematics of load-displacement curve [Poi99].

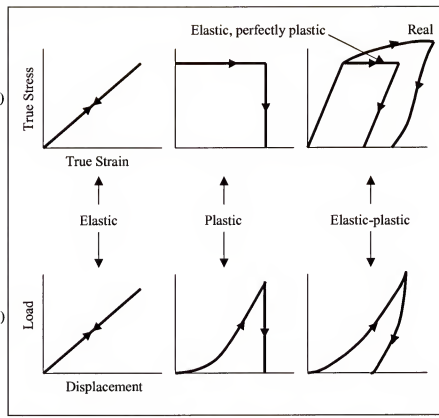

Figure 7-2 Schematics of stress-strain curves (a) and typical indentation curves (b) for ideal elastic, rigid-perfectly plastic, and elastic-plastic (ideal) and real elastic-plastic solids [Got97].

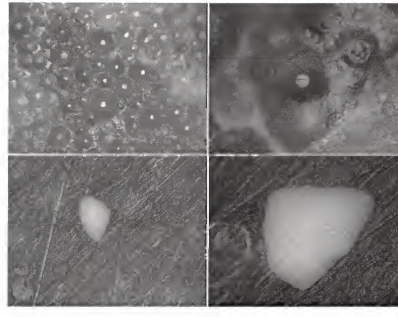

Figure 7-3 SEM micrographs of polished silica nanoparticle surface embedded into cold mounting polymer materials.

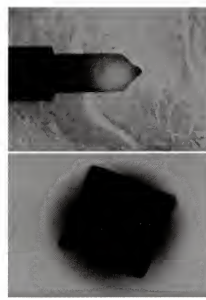

Figure 7-4 Micrographs of Berkovich indent tip.

(a)

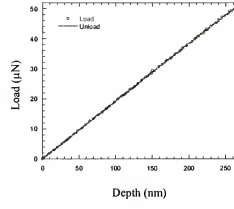

(b)

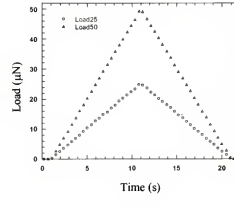

Figure 7-5 Plots of calibration of nanoindentation; (a) load-depth and (b) load-time.

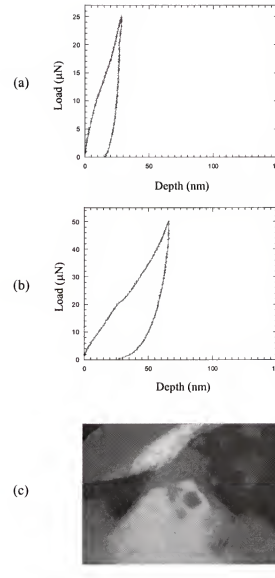

Figure 7-6 Plots of load versus depth in nanoindentation measurements with a 25 μN (a), 50 μN (b) and SEM micrographs of 2.8% porous silica nanoparticles indented with 50 μN (c).

(a)

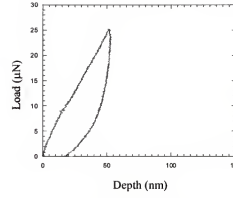

(b)

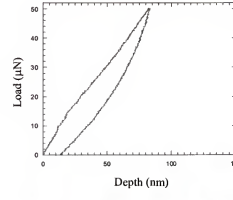

(c)

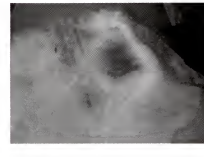

Figure 7-7 Plots of load versus depth in nanoindentation measurements with a 25 μN (a), 50 μN (b) and SEM micrographs of 4.6% porous silica nanoparticle indented with 50 μN (c).

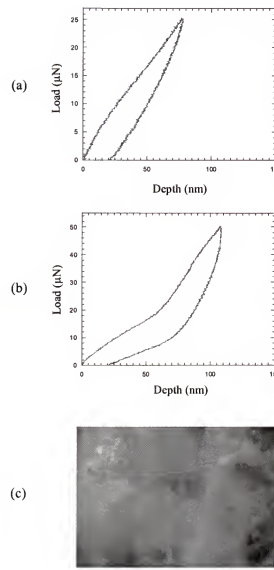

Figure 7-8 Plots of load versus depth in nanoindentation measurements with a 25 μN (a), 50 μN (b) and SEM micrographs of 6.9% porous silica nanoparticles indented with 50 μN (c).

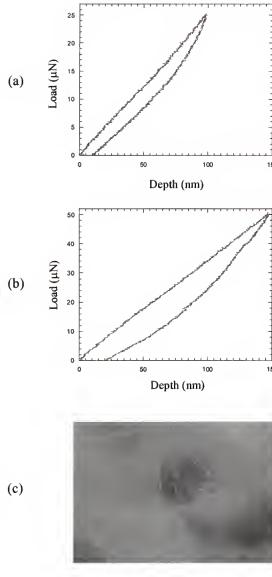

Figure 7-9 Plots of load versus depth in nanoindentation measurements with a 25 μN (a), 50 μN (b) and SEM micrographs of 13.9% porous silica nanoparticles indented with 50 μN (c).

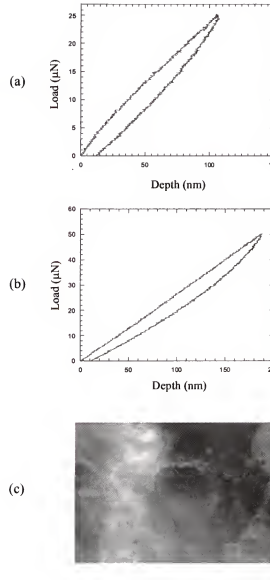

Figure 7-10 Plots of load versus depth in nanoindentation measurements with a 25 μN (a), 50 μN (b) and SEM micrographs of 22.2% porous silica nanoparticles indented with 50 μN (c).

(a)

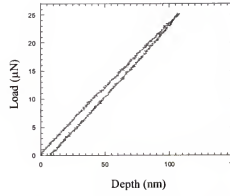

(b)

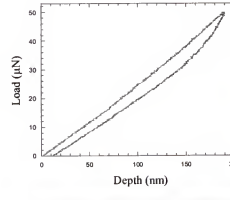

(c)

Figure 7-11 Plots of load versus depth in nanoindentation measurements with a 25 μN (a), 50 μN (b) and SEM micrographs of 32.3% porous silica nanoparticles indented with 50 μN (c).

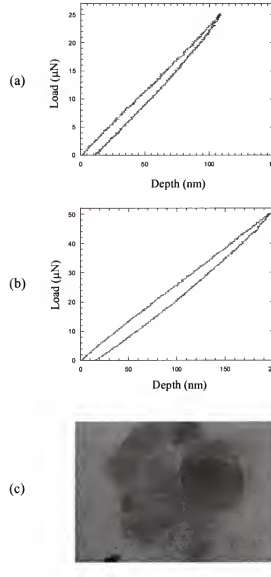

Figure 7-12 Plots of load versus depth in nanoindentation measurements with a 25 μN (a), 50 μN (b) and SEM micrographs of 36.1% porous silica nanoparticles indented with 50 μN (c).

(a)

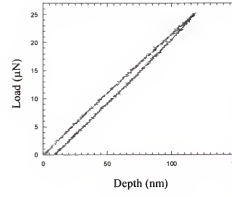

(b)

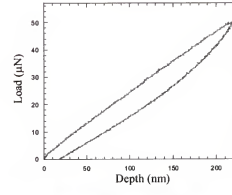

(c)

Figure 7-13 Plots of load versus depth in nanoindentation measurements with a 25 μN (a), 50 μN (b) and SEM micrographs of 57.6% porous silica nanoparticles indented with 50 μN (c).

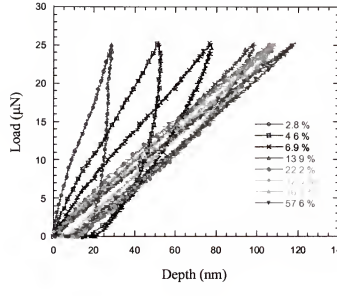

Figure 7-14 Plots of load versus depth in nanoindentation measurements of silica nanoparticle with different surface porosity at load of 25 μN.

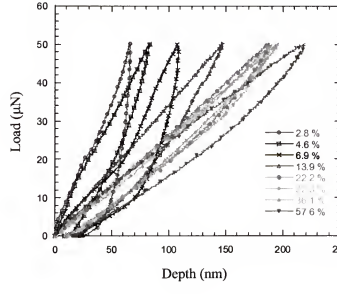

Figure 7-15 Plots of load versus depth in nanoindentation measurements of silica nanoparticle with different surface porosity at load of 50 μN.

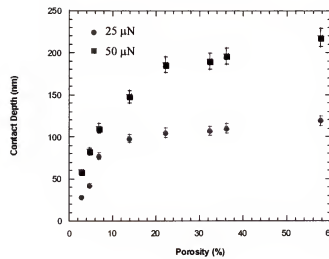

Figure 7-16 Contact depth of indented silica particles as a function of surface porosity.

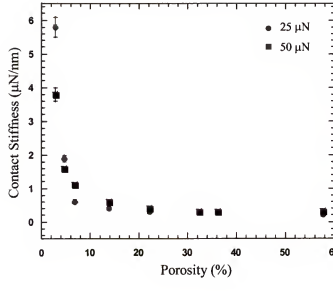

Figure 7-17 Contact stiffness of indented silica particles as a function of surface porosity.

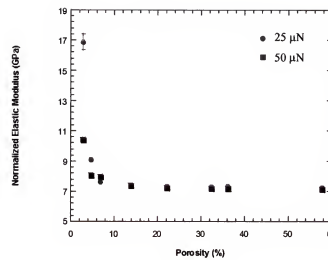

Figure 7-18 Elastic modulus of indented silica particles as a function of surface porosity.

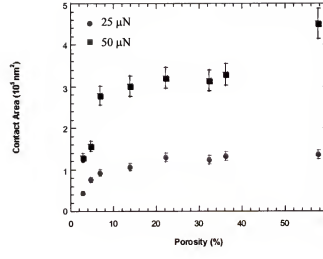

Figure 7-19 Contact area of indented silica particles as a function of surface porosity.

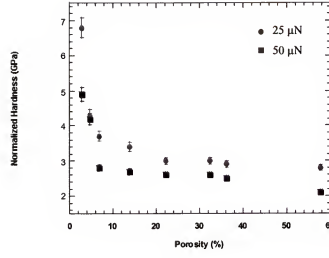

Figure 7-20 Hardness of indented silica particles as a function of surface porosity.

CHAPTER 8
INSPECTION OF THE SURFACE DEFECTS OF CMP SUBSTRATES POLISHED IN NANOPOROUS SILICA PARTICLE BASED SLURRY

Introduction

The complete CMP sequence will end with an effective cleaning process, leaving planarized surface defect and contamination free and ready for the next step in the device/circuit fabrication sequence. Planarization of dielectric films, silicon dioxide, silicon nitride, etc. by CMP is regulated and moderated by the interaction of the abrasive particles and chemicals in solution with the film surface through complex chemical and physical processes. Changes in the slurry properties have a profound effect on the polishing chemistry and relative removal rates of dielectric films. Common slurry properties include pH, temperature, abrasive particle composition, its size and shape, degree of agglomeration, and weight percent, and chemical composition [Dej96].

CMP relies on mechanical abrasion coupled with chemical activity to remove and ultimately planarize the top film or films on wafers during semiconductor processing. The mechanical variables during CMP, including table speed, down force, pad hardness, etc., are typically used to control rate, planarity, and uniformity. The chemical part of CMP is usually exploited to achieve selectivity and help address issues of pattern dependence such as erosion and polishing. However, during the CMP process the abrasive slurry particles may cause several types of the surface defects depending on the

characteristics of the abrasive particles and wafers to be polished. To reduce the surface defects the optimized slurry design is strongly required, which includes the type of the abrasive particle, particle size and distribution, particle shape, and many others.

The surface planarized by CMP may have undesirable features on or within the surface due to: (i) particles from the slurry or from the abraded surface and even from the surroundings, (ii) chemical contamination from the slurry and/or chemical cross-contamination resulting from different materials present on the surface during CMP of inlaid metal, (iii) physical damage, like scratches and pits, (iv) stress, in the polished surface, associated with the compaction of the top few atomic layers, and (v) surface inclusions formed due to reactions with abrasive particles or pad materials [Hea00].

We have characterized the nanoporous silica particles in terms of the optical, electrical, and mechanical properties by several measurements and calculations in earlier chapters. It has been theoretically proven that the nanoporous silica particles have the possibility to reduce the surface defects in the CMP process. In this study, to testify the effectiveness of the porous silica particle compared to nonporous one for lower surface defectivity the CMP tests were performed in synthesized porous silica particle based slurry systems with three wafer surfaces such as silicon, black diamond, and silicon nitride. However, the inspection of the surface defects is so complex and difficult that the specific instruments are required to detect them. Furthermore, the classification of the defect type is not simple since there are many parameters to cause the surface defect. Even with the specific instruments for this purpose, it may be not accurate and several unknown reasons will exist. We have inspected some surface defects, which can be observed by the simple instruments including the optical microscope, SEM and AFM, of wafers polished in the same slurry system and CMP condition according to the type of the

wafer. The simple defects detected in this experiment are discussed in detail in terms of surface scratches and residual slurry particles.

There are two types of defects that reside on a planarized surface: defects that are held on the surface by physical forces and defects that are held by the chemical bonding. The two types cover both on-surface and in-surface defects. Examples of the in-surface defects will be inclusions that are part of the surface that has been planarized [Rav97].

Physical Defects

The physical defects, such as the abrasive particles, their clusters, the fragments of the surface abraded by the abrasive and/or the pad, or similar contaminants including molecular or cluster of molecules in the rinsing liquid, are held on to the surface as a result of the physical, such as van der Waals attraction between the surface and the particle. In such cases, there is a lack of a true chemical bond between the two. Generally such attractions are weak compared to chemical bonding and the result of dipoles induced in molecules when present in the vicinity of other molecules which also develop dipoles [Tom99]. Assuming that the van der Waals interaction energy for the intermolecular pair, separated by a distance, r, is given by $-C/r^6$, the van der Waals interaction energy of a molecule interacting with a surface at a distance, D, which is similar to Equation 4.11 but differently expressed due to different circumstance is given by

$$V_{M/S} = -\frac{\pi C \rho}{6D^3} \qquad 8.1$$

where ρ is the density of molecules in the solid. However, for a particle of a radius, R, at a distance, D, away from the surface and for $D \ll R$, the interaction energy is given as

$$V_{P/S}\left(D\langle\langle R\right) = -\frac{\pi^2 C\rho^2 R}{6D} \qquad 8.2$$

and for $D \rangle\rangle R$

$$V_{P/S}\left(D\rangle\rangle R\right) = \frac{\pi C\rho N}{6D^3} \qquad 8.3$$

where N is the number of molecules in the particle of radius, R, and is thus equal to 4/3 $\pi R^3\rho$. Also in Equations 8.1 to 8.3 the subscripts *M/S* and *P/S* qualify the molecule-to-surface and the particle-to-surface interactions, respectively [Tom99].

It is clear from the above considerations that for $D \langle\langle R$ van der Waals interaction energy, so-called physical adhesion force, between large particles and the surface decays much more slowly with distance than between a molecule and the surface. On the other hand, at large separation, $D \rangle\rangle R$, the interaction decays very quickly with distance. Also note that the interaction energy or the adhesion force increases with the particle diameter. However, for a mechanical removal of the particle from the surface, the required acceleration decreases with increasing particle diameter because the mechanical forces depend on the mass or volume of the particles.

When the van der Waals attraction brings a particle or molecule closer to the surface, a repulsive force develops between the core electrons of the particle surface and those of the atoms in the surface. The equilibrium separation is determined by a balance between the repulsive and the attractive forces and decreases with increasing radius of the particle as described by DLVO theory in chapter 6. Note also that the dielectric constant of the medium separating the particle and the wafer surface also affects the magnitude of

van der Waals interaction energy in Equations 8.1 to 8.3, as the constant C is inversely proportional to the dielectric constant. The van der Waals attractive interaction energy is small, and thus the physisorption bonds are weak and can be easily broken, especially when cleaning in high dielectric constant liquids such as water.

Physisorption is strongly aided by the presence of mechanical defects such as scratches and surface steps on the surface. The smoother the surface, the lower will be the particulate density on the surface due to physical adsorption. The observed lower defect density on CMP surfaces is perhaps the result of a lack of so-called mechanical defects on such surfaces [Oli00].

Chemical Defects

Chemical contamination arises due to strong chemical bonding between the atoms or molecules from the slurry and pad to those on the surface being planarized. Chemical defects, on the other hand, are formed due to chemical interactions between particles or pad and the surface being planarized [Lar96]. One of examples of the latter is an abrasive Al_2O_3 and SiO_2 surface interactions. Theses surface inclusions of Al_2O_3 are associated with chemical interactions between SiO_2 and Al_2O_3 in a certain pH range. Such inclusions are also a function of the particle size, pressure, and platten rotational velocity. Excessive friction forces may tear off pad material and cause their inclusion in the surfaces being polished, especially in the softer material surface [Shi97].

Chemical contaminations arise from the interactions of slurry chemicals added to provide specific planarization behavior [Poa00]. For example, KOH or NH_4OH is added to provide chemical etch rates of SiO_2 surface, and oxidizers are added to W or Cu slurries to produce passivating surfaces that protect low areas on the surface from chemical etching. These chemicals may produce contamination on polished surfaces

leading to unwanted electrical activity (corrosion) in metals. Chemical contamination may also result from the metal surfaces exposed to polishing of SiO_2 or polymer dielectrics, from ILD surfaces to exposed metal surfaces, or from underlying diffusion barrier/adhesion promoter layers at the end of metal polishing to neighboring metal or dielectric surfaces. Some of these contaminant atoms/molecules may also be pinned into the surface being planarized due to the mechanical forces employed during polishing leading to increased compressive stress in the surface layers as in the case of *Cu* CMP. Not only contaminants can cause this pinning, the atoms of the surface being polished and removed by the abrasion can also get pinned into the surface causing increased compressive stress [Soh00].

Chemical contamination may also result due to electrochemical effects during CMP or the withdrawal of the surfaces from the slurry and during cleaning in solutions containing the impurity atoms. Thus, maintaining the purity of chemicals used in slurry formations and cleaning solutions is essential [Tom99].

CMP Defect Classification

CMP related particles are typically measured on the front side of a wafer using laser scattering instruments. While this well established technology offers reproducible and meaningful particle information, it has significant limitations. The main limitation of laser-scattering tools is that they cannot defect all particles based on their size, morphology, or location [Tom99]. For example, particles located in the edge exclusion area or on the bevel edge of the wafer cannot be identified. This type of contamination can have a deleterious impact on die yield since it can transfer to the front of the wafer during downstream processing. Another class of defects located on the front of a wafer cannot be detected using particle counters because of size or morphology considerations.

This type of contamination is easily visible with dark field microscopy, SEM, or AFM, but it is difficult to quantify. Table 8.1 shows the classification of CMP defects including the morphology techniques suitable for identification of each defect classification and typical densities per wafer [Tom99].

Table 8.1 Classification of CMP defects.

Class	Type	Typical Size	Metrology Technique	Preclean Defects/wafer
A	Scratch	Few μm – several mm	Laser scattering	< 5
B	Area defect	0.5 μm – several mm	Laser scattering	20-500
C	Large particle	≥ 0.2 μm	Laser scattering	$> 10^5$
D	Small particle	<= 0.2 μm	SEM, dark field, AFM	10^4-10^9
E	Edge particle	≥ 0.2 μm	SEM	10^5-10^9

Oxide CMP defects such as scratches are classified as Class A defects as listed in Table 8.1. These defects are a direct result of a failure of the polish and are caused by one of several problems. Any large and hard substance, such as a chunk of dried slurry, falling on the polishing pad can lead to the semicircular scratch. These defects are typically several microns wide and many millimeters long. Since Class A defects cannot be removed by any cleaning technique, they must be minimized or eliminated by proper control of polishing, environment, and pad-conditioning techniques.

Class B defects are seldom found in great numbers. On a laser-scattering particle counter, they can appear as short area defects and may be misinterpreted as small scratches. However, under SEM or dark-field microscopy many of these defects are clearly identified as slurry that appears to be smeared across the wafer surface. This type of defect can be several microns wide and tens of microns long. The density of these defects is variable but seldom very large. The slurry that forms a Class B defect is strongly bonded to the wafer surface [Zik97].

Class C defects are ubiquitous to CMP. These defects are slurry particles loosely

attached to the wafer surface. They are common to all polishing processes but are much reduced if a DI-water buff is included. These particles come in a range of sizes since they are caused by agglomeration of slurry particles. Class C defects are formed from piles of individual slurry particles. SEM analysis has shown that these agglomerates are typically around 1.0 μm across and 0.2 μm high. There can be $>10^5$ of these particles on the wafer surface before cleaning, but they are easily removed by DI water.

Class D defects are listed in Table 8.1 as being <0.2 μm. Although AFM analysis indicates such defects may reach 0.5 μm in diameter, they are difficult to detect using laser scattering because they are normally <600 Å high. The density of these defects varies greatly, ranging from 10^3 to 10^9 defects/wafer. The lower densities are often found for DI-water buff processes, while the higher concentrations are seen following a one-step CMP process. The use of a water rinse on the hard pad can significantly increase the density of Class D defects if the rinse is not implemented correctly [Tom99]. This kind of defect differs greatly from the Class C variety: Class D defects are much smaller, can have an extremely high density with $>10^9$ per wafer, and can be difficult to remove. AFM and SEM analyses indicate that these defects are composed of a small number of individual slurry particles bound together. These slurry particles are seldom more than one layer thick, which accounts for their lack of height. Class D defects are the least understood and, because of their small size, their impact on device yield is not clear; however these strongly bonded defects are readily removed using HF solution.

The Class E defects cannot be observed using standard light-scattering techniques because they are located in the edge-exclusion region of the wafer on or near the bevel edge. These defects are similar to Class C defects when viewed by SEM, yet they are not easily removed using standard cleaning techniques. Their presence or absence is strongly

dependent on the polishing equipment and process. This type of contaminant can become dislodged during subsequent processing and then transfer to the front of the wafer where it can adversely affect device yield.

Experimental

Sample Preparation

The silica and silicon nitride wafer samples used for the CMP experiments were obtained from 8 inch diameter p-type <100> silicon wafers, on which 2.0 μm thick SiO_2 films and 1.5 μm Si_3N_4 films had been deposited by plasma enhanced chemical vapor deposition (PECVD), respectively. Balck diamond wafer was obtained from Applied Matrials Inc. For all samples used for the polishing experiments, 1.0 inch x 1.0 inch squares were cut and then cleaned with an acetone in ultrasonificator to remove impurities, then rinsed with deionized water. Nonporous silica particles of four different sizes (1.5 μm, 1.0 μm, 0.2 μm, and 0.1 μm) were obtained from Geltech Inc. The porous silica particles as described in chapter 3, on the other hand, were synthesized with various surface porosities (2.8%, 22.2%, 36.1%, and 57.6%) but the same particle size of 0.2 μm for the slurry preparation. These particles are highly spherical and have a narrow size distribution, making them ideal for such a study. The size and shape of these particles were characterized by electron microscopy and particle size analysis. The particle size analysis was conducted using a Honeywell Microtrac UPA 150 particle size analyzer which utilizes the technique of dynamic light scattering. Scanning electron microscopy (JEOL JSM 6400 SEM) was used to characterize the two larger sizes of 1.5 μm and 1.0 μm, while transmission electron microscopy (JEOL 200 CX TEM) was used to characterize the 0.2 μm and 0.1 μm particles.

Slurry Preparation

The slurries for the polishing experiments were prepared by adding a 5 wt.% of the particles to deionized (DI) water without any additive. After adding the particles, the pH was fixed to 3 using *HCl* and NH_4OH to investigate the effects of particle size and the surface porosity of the particles. The particles were then dispersed by using ultrasonic energy and mechanical agitation. Bath sonicators were used for this purpose. The smaller particles were more aggregated, and took longer to disperse. Particle size analysis was used to confirm the quality of dispersion and to verify the particle size as observed by SEM.

Setup for Polishing

The setup for the CMP experiments is shown in Figure 2.1. A Struers Rotopol 31 polisher, along with a Struers Multidoser slurry feed system and a Struers Rotoforce 3 polishing head was used for conducting all the polishing experiments. The Rotopol unit has a 12 inch diameter platen on which the polishing pad is mounted. The pads used for the experiments were IC 1000/Suba IV stacked pads, obtained from Rodel Corporation. This is a standard configuration used by the CMP industry. The Multidoser unit consists of several peristaltic pumps which are used to transport the slurry to the pad. The Rotoforce unit is the polishing head in which the sample holder is mounted. Pressure is applied pneumatically, and the polishing time and pressure can be set to desired values. The sample holder is a 2.25 inch diameter stainless steel cylinder, with a height of 1.13 inches. A flat square recess (1 inch x 1 inch x 0.03 inch) is machined in the center of one of the flat surfaces. The recess constrains the wafer mechanically during polishing, preventing it from sliding out or moving. A backing material (obtained from Rodel) is mounted inside the recess. It brings the wafer slightly (0.05 inch) above the flat sample

holder surface, and is made wet before the sample is put on it, in order to hold the wafer using capillary forces. Additionally, it provides some backing flexibility to compensate for local variations in pad thickness during polishing. The experimental conditions were set as follows: the sample and pad rotation speeds were fixed at 150 rpm (translating to a linear velocity of 1.4 m/s), the downward force was set at 7.0 *Psi* (48.4 *kPa*), and the sample was offset by 3.5 inches from the center of the pad. After polishing, the samples were ultrasonicated in DI water (pH 10). This provides mechanical energy to dislodge slurry particles from the wafer surface, and the alkaline pH enhances electrostatic repulsion between the two surfaces as well.

The polishing rate was determined by measuring the thickness of the films in the central region after polishing using variable angle spectroscopic ellipsometry (VASE). The difference in thickness was used to determine the polishing rate. The surface morphology and roughness of the polished samples was characterized by atomic force microscopy (AFM).

Results and Discussion

Polishing Rate

The CMP experiments of three different wafers were conducted in the different slurry systems, which are varied by the particle size, the surface porosity of the particle, and the type of the particle in terms of its hardness and shape. Since we are interested in the effect of the characteristics of the slurry particles, the concentration of the solid loading and pH were fixed to 5% by the weight and 3, respectively. Figure 8.1 shows the comparison of the removal rates among three wafers, such as silica, silicon nitride, and black diamond, polished in the nonporous silica slurry as a function of the particle size. As reported by many people, the removal rate was decreased with decreasing the particles

size for all wafers. The silica wafers showed higher removal rates than silicon nitride and black diamond wafers in all particles size ranges, while the balck diamond showed higher removal rates than silicon nitride wafer due to the different degree of the surface reaction rate in water at pH 3 between them. The dissolution rate of the silica in water is higher than other two wafers so that the silica wafer surface can easily generate the gelation layer resulting in very soft hydroxide layer, whereas the chemical reaction of silicon nitride or black diamond wafers in water does not occure significantly as much as does silica wafer [Ada67]. The other reason for higher removal rate of silica wafer may be the difference in the hardness of each wafer surface expecting that the lowest removal rate may be obtained in the silicon nitride wafer due to higher hardness. However, even though it is known that the black diamond is softer than silica, whose hardness are approximately 2.3 GPa and 6 GPa, respectively, silica wafer showed higher polishing rate since the dissolution rate of the silica surface in water is much higher than that of the black diamond wafer indicating that the chemical reaction rate is predominant in this polishing case. For a case of the silicon nitride wafer, both chemical and mechanical reactions are not occured significantly since the silicon nitride surface has very high value of the hardness and low chemical reactivity in water compared to rest of them resulting in very low polishing rate in all particle size ranges. The large variation of the polishing rate of silica wafer depending on the particle size can be explained by the indentation mode which is described by Mahajan for large particle size range, while it can be explained by the surface contact mode for small size particle [Mah00]. The large the particle size, the deeper the impaction of the surface resulting in higher polishing rate.and the smaller the surface contact area. Typically smaller particles result in higher removal rate only when the slurry loading is ver high due to large surface contact area contributing the polishing

rate.

Figure 8.2 shows the polishing rate of three wafers polished in different slurry systems, which include the silica, alumina, and silicon nitride particles but the same particles size of 0.5 μm in diameter, to investigate the effect of particle shape or hardness. The silicon nitride particle based slurry showed higher removal rates in all wafer surfaces while the lowest polishing rates were obtained by silicon nitride wafer in all slurry systems due to very hard surfaces of both particle and wafer. The silica wafer has higher value of the removal rate than the black diamond in all three slurry systems, which is exactly agreed with the result of the particle size effect as illurstrated in Figure 8.1, since silica has higher chemical reactivity in water than black diamond even though the former is harder than the latter as described above. However, the comparison of the removal rate between silica and black diamond wafers in alumina particle based slurry system showed somewhat different result. Higher polishing rate was obtained in the black diamond wafer compared to silica wafer indicating that the mechanical polishing invloving the hardness of the wafer surfaces is predominant more than the chemical reactivity in this case, although more accurate reason for this result is unknown.

The effect of the surface porosity of the slurry particle on the removal rate of three diffrent wafers was investigeted. Figure 8.3 shows the removal rate of three wafers, such as silica, silicon nitride, and black diamond, polished in the 0.2 μm porous silica slurry of 5 wt.% loading at pH 3 as a function of the surface porosity of the silica particle. As shown in the result of the effect of the particle size, the removal rate decreases with increasing the porosity of the slurry particle for all three wafers. The polishing rate of the silica wafer decreases abruptly as the porosity increases and then maintains almost same value from around 36% to 57%. It was found in the previous chapters that the hardness

of porous silica particles and van der Waals attractive force between the porous silica particle and silica wafer surface decreases as the porosity increases. These facts attribute to the reduction of the removal rate of silica wafer in low surface porosity range and the maintainance of that in high porosity range. Silicon nitride wafer showed lower removal rate comapred to silica wafer in all porosity ranges with a slight decrease as the porosity increases, as observed in the case of the black diamond wafer, since the hardness of silicon nitride surface is predominante in this polishing process.

Aa a result, the polishing rate of the wafer surfaces depends on the particle size indicating that it is proportional to the particle size. The deviation of the polishing rates among three different wafers but in the same slurry system is dependent of the type of the reactions such as either chemical or mechanical, which may gorven the polishing rate, being occured between the abrasive particle and wafers. For a case of silica wafer, wafer surface can be easily dissolved in water resulting in easy generation of the gelation on the wafer surface by chemical reaction followed by mechanical polshing leading to higher removal rate, whereas there is no significant chemical reaction between silica particles and black diamond wafer surface resulting in lower removal rate even though the black diamond has lower hardness. It indicates that the polishing of the black diamond in silica particle based slurry system is predominated by the mechanical reaction expecting both lower removal rate and higher surface scratch, which will be discussed later. For silicon nitride case, it shows very low polishing rate since it is very hard material and even mechanical reaction does not significantly affect the polishing rate due to very low chemical reaction between silica particles and silicon nitride wafer surface.

On the other hand, the different abrasive particles, which have different particle shapes and hardness, resulted in the same phenomena as found in the different size of the

slurry systems. Both chemical and mechanical reactions between silica particle and silica wafer surface are predominant in silica CMP, while very poor chemical reaction is occured between alimina particle and silica wafer resulting in lower polishing rate. The highest removal rate of silica CMP was obtained by silicon nitride particles due to very high hardness of the silicon nitride particle and good chemical mechanical reactions between silica wafer and silicon nitride slurry particles. For a case of the black diamond wafer, the soft silica particle generated lower polishing rate, whereas higher polishing rates were obtained by both alumina and silicon nitride slurry particles since they have higher values of mechanical hardness indicating that only mechanical polishing is predominant in these cases.

The surface porosity of the slurry particle significantly affected the polishing rate resulting that the polishing rate is inversly proportional to the surface porosity since the hardness of the silica particles decreases with increasing the surface porosity as described in chapter 7. The reason that silica wafer showed higher removal rate in all the surface porosity ranges compared to silicon nitride or black diamond wafers is the same as the case of the effect of the particle size as described above, which depends on the type of reaction between the slurry particle and wafer surfaces and their hardness.

Surface Sratches

Counting the surface scratch of the three wafers polished was carried out by using the optical microscopy in the area of 10^{-2} in^2 scale. As described above the inspection of the surface defects is very complicated and it requires the specific instrument which can detect precisly all types of defects. However, even with very accurate detector, some errors may be occured. In this work only surface scratch of three wafers polished in

different slurry systems were detected and counted in terms of the number of the scratch wintin small surface area using the optical microscopy. Figure 8.4 shows the scratches of the black diamond wafer surfaces polished in the nonporous silica slurry of 5 wt.% loading at pH 3 as a function of the particle size of 1.0 μm, 0.5 μm, 0.2 μm, 0.1 μm, and 0.05 μm. The larger the particle size, the more the surface scratches for all tree wafers. The number of the surface scratch counted under the optical microscope of three wafers are shown in Figure 8.5 as a function of the particle size. The trend of these graphs are similar to that of the removal rate of three wafers as a function of the particle size as shown in Figure 8.1 in that the number of the surface scratch decreases with decreasing the particles size for all samples. However, the comparison of the number of the surface scratch between different wafers showed the different results indicating that the surface hardness of the wafer surface plays more important role to cause the surface scratch. The Black diamond generated much more surface scratches than silica or silicon nitride even though it showed lower value of the polishing rate than silica wafer.

The effect of the type of the slurry particle is shown in Figure 8.6. The silicon nitride particle generated the highest number of the surface scrach on the Black diamond wafer, while alumina particle generated lower number of the surface scratch on the Black diamond indicating that the surface scratche also depends on the hardness of the slurry particles. Figure 8.7 shows the scratches of the black diamond wafer surfaces polished in the 0.5 μm nonporous of silica, alumina, and silicon nitride particle slurries of 5 wt.% loading at pH 3. For all three slurry systems with different types of the particles the number of the surface scratch depends on the hardness of both the wafer surface and the slurry particles. For a case of the black diamond wafer all three slurry particles having different values of the hardness generated more sctaches bacause of lower hardness of the

black diamond wafer. It is clear that the generation of the surface scratch significantly depends on the reaction type between slurry particles and wafer surface indicating that both higher chemical and mechanical reactions lead to higher removal rate and lower number of the surface scratch associated with the hardness of both slurry particle and wafer surface, whereas lower chemical reaction but very high mechanical reaction including the hardness of one of them or both leads to very serious scratches on the wafer surface.

On the other hand, Figure 8.8 shows the effect of the surface porosity on the scratch generated on the black diamond wafer surface polished in 0.2 μm nonporous silica slurry of 5 wt.% loading at pH 3 as a function of the surface porosity of the particles of 2.8%, 13.9%, 36.1%, and 57.6%. The number of the surface scratch of all three wafers decreases with increasing the surface porosity as shown in Figure 8.9. The black diamond showed the large variation in the number of the surface scratch when the surface porosity changes, while silica and silicon nitride wafers resulted in a slight change depending on the surface porosity indicating that the surface scratch is dependent of the hardness of the wafer surface. It also clearly indicates that the surface scratch is inversly proportional to the surface porosity of the slurry particle especially in soft material CMP.

Surface Roughness

Figure 8.10 shows the surface roughness of the silica wafer polished in the nonporous silica slurry of 5 wt.% loading at pH 3 as a function of the particle size of 1.0 μm, 0.5 μm, 0.2 μm, 0.1 μm, and 0.05 μm. The RMS values of each wafer surface measured by AFM were presented in Figure 8.11 as a function of the particle size. These results are exactly agreed with those of counting the surface scratches as shown in Figure 8.5. The larger the particle size, the larger the number of the surface scratch and the

larger the surface roughness. The black diamond wafer surface, which has large number of the surface scratches generated by different particles such as silica, alumina, and silicon nitride, resulted in higher RMS values for all slurry particles as shown in AFM micrographs of silica wafer and the graph of RMS of all three wafers in Figures 8.12 and 8.13, respectively.

On the other hand, the effect of the surface porosity on the surface roughness of silica wafer is shown in Figure 8.14. As described in the earier section of the surface scratches, the surface becomes smoother as the surface porosity increases resulting in lower values of RMS in high surface porosity ranges above around 36%. It is meant that both van der Waals attraction force and the particle hardness, which are reduced with increasing the surface porosity as discussed in previous chapters, significantly influence the surface quality resulting in lower RMS values. Figure 8.15 shows the comparison of the surface roughness of all three wafer surfaces polished in 0.2 μm silica particle slurry as a function of the surface porosity. It indicates that the highly porous silica particle can enhance the surface quality of wafers polished in hard particle based slurry system resulting in the significant reduction of the surface defects in several CMP performances.

Residual Slurry Particles

The residual slurry particles of the silica wafer surfaces polished in the 0.2 μm nonporous silica slurry of 5 wt.% loading at pH 3 as a function of the surface porosity of the particle of 2.8%, 13.9%, 36.1%, and 57.6% were detected by SEM as shown in Figure 8.16. The area defect of the residual slurry particles classified in the earier senction was observed in the silica wafer surface polished in 2.8% porous silica particle slurry system, whereas small particles were detected in silica wafer polished in highly porous silica particle slurries. It indicates the lack of the repulsive interaction force between

nonporous silica particle and silica wafer as measured by the direct interaction force using silica particle probe technique in chapter 5 resulted in such area defect involving many particle agglomerates. The number of the residual slurry particles decreases as the surface porosity of the slurry particle increases indicating that the repulsive force between slurry particles and wafer surface is dependent of the surface porosity resulting in the reduction of van der Waals attraction force between them. Only small size of the particle aggregates were observed in silica wafer polished in 57% porous silica particle based slurry system indicating that the porous silica particle is capable to enhance the surface quality of CMP wafer to be polished, which is dependent on the surface defects genrated by several parameters during CMP process, and several investigations for the properties of porous silica particles conducted in the previous chapters have been proven by the results of CMP experiments, which showed the reduced surface defects of the wafer surface polished in porous silica particle slurry system.

Summary

The CMP experiments of three different wafers, such as silica, silicon nitride, and black diamond, were performed in the various slurry systems, which include nonporous silica particle varying the particle size, porous silica particles with various surface porosities, and different types of particles including alumina and silicon nitride in terms of the particle shape and hardness. The large particles showed higher polishing rate resulting in large number of the surface scratch and higher RMS value conducted by the optical microscopy and AFM, respectively. The variation of the removal rates between diffrent wafer surfaces implied that the type of reaction between the slurry particles and wafer surface dominates the ploishing rate leading to the variation of the surface scratches and roughness between them. Lower chemical reaction but very hard slurry particles

reacting with a hard wafer surface resulted in lower removal rate and very serious surface scratches.

On the other hand, the surface porosity of the slurry particles has proven that it is able to reduce the surface defects in terms of the surface scratches and residual slurry particles of wafer surfaces polished in higly porous silica based slurry systems since the hardness of silica particles decreases with increasing the surface porosity and the van der Waals attraction force between silica wafer and silica particles becomes smaller as the surface porosity of the slurry particles increases, which influences significantly both removal rate and surface quality of CMP wafers.

As a consequence, the inspection of the surface defects of CMP wafer polished is very complicated and it may cause some errors even with very accurate instruments since many reasons, which cause the surface defects during CMP process, are unknown yet. However, the simple experiments conducted in this work indicated that the porous silica particles can enhance the surface quality by reducing surface defect.

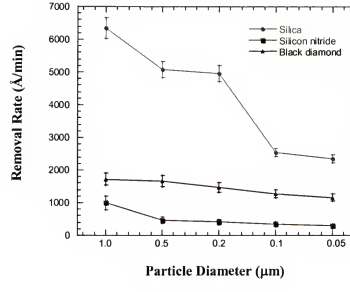

Figure 8-1 Removal rate of three wafers (silica, silicon nitride, and black diamond) polished in the nonporous silica slurry of 5 wt.% loading at pH 3 as a function of the particle size.

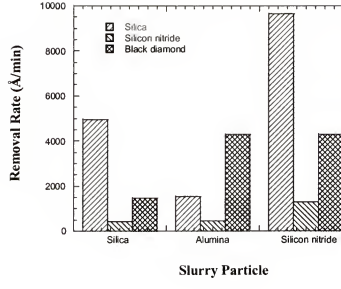

Figure 8-2 Removal rate of three wafers (silica, silicon nitride, and black diamond) polished in the 0.5 μm nonporous silica, alumina, and silicon nitride slurries of 5 wt.% loading at pH 3 as a function of the particle size.

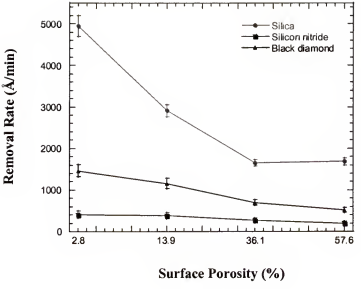

Figure 8-3 Removal rate of three wafers (silica, silicon nitride, and black diamond) polished in the 0.2 μm porous silica slurry of 5 wt.% loading at pH 3 as a function of the surface porosity of the silica particle.

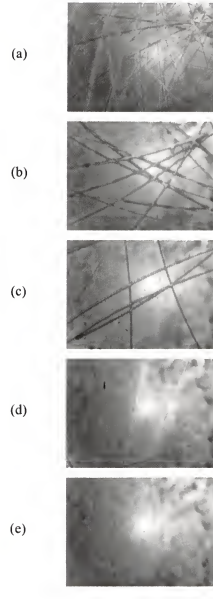

Figure 8-4 Scratches of the black diamond wafer surfaces polished in the nonporous silica slurry of 5 wt.% loading at pH 3 as a function of the particle size: (a) 1.0 μm, (b) 0.5 μm, (c) 0.2 μm, (d) 0.1 μm, and (e) 0.05 μm.

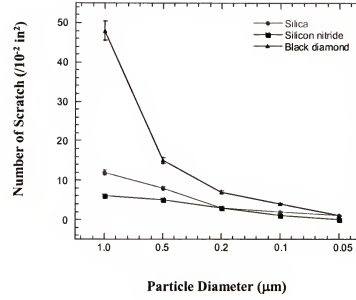

Figure 8-5 Number of scratches of the black diamond wafer surfaces polished in the nonporous silica slurry of 5 wt.% loading at pH 3 as a function of the particle size: (a) 1.0 μm, (b) 0.5 μm, (c) 0.2 μm, (d) 0.1 μm, and (e) 0.05 μm.

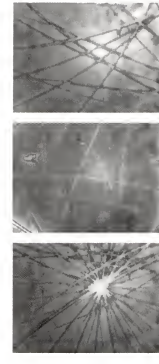

Figure 8-6 Scratches of the black diamond wafer surfaces polished in the 0.5 μm nonporous (a)SiO_2, (b) Al_2O_3, and (c)Si_3N_4 slurries of 5 wt.% loading at pH 3.

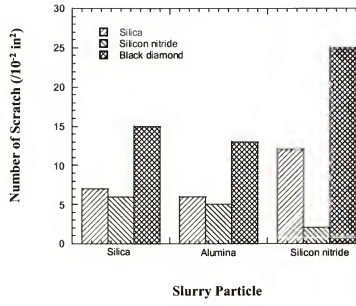

Figure 8-7 Number of scratches of the black diamond wafer surfaces polished in the 0.5 μm nonporous (a)SiO_2, (b) Al_2O_3, and (c)Si_3N_4 slurries of 5 wt.% loading at pH 3.

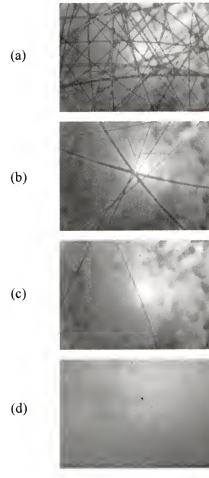

Figure 8-8 Scratches of the black diamond wafer surfaces polished in the 0.2 μm nonporous silica slurry of 5 wt.% loading at pH 3 as a function of the surface porosity of the particle: (a)2.8%, (b) 13.9%, and (c)36.1%, and (d) 57.6%.

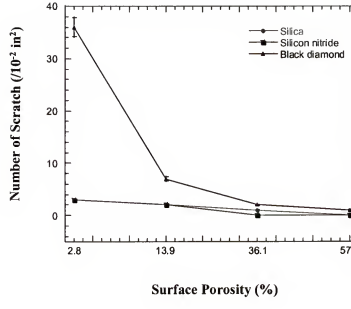

Figure 8-9 Number of scratches of the black diamond wafer surfaces polished in the 0.2 μm nonporous silica slurry of 5 wt.% loading at pH 3 as a function of the surface porosity of the particle: (a)2.8%, (b) 13.9%, and (c)36.1%, and (d) 57.6%.

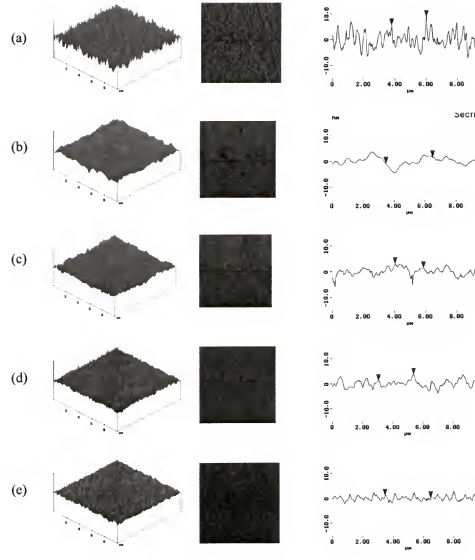

Figure 8-10 The surface roughness of the silica wafer polished in the nonporous silica slurry of 5 wt.% loading at pH 3 as a function of the particle size: (a) 1.0 μm, (b) 0.5 μm, (c) 0.2 μm, (d) 0.1 μm, and (e) 0.05 μm.

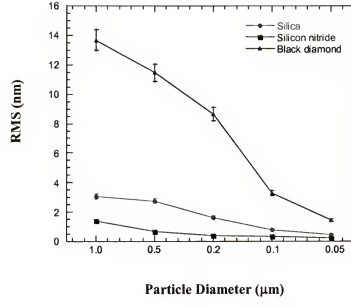

Figure 8-11 The surface roughness of the silica wafer polished in the nonporous silica slurry of 5 wt.% loading at pH 3 as a function of the particle size: (a) 1.0 μm, (b) 0.5 μm, (c) 0.2 μm, (d) 0.1 μm, and (e) 0.05 μm.

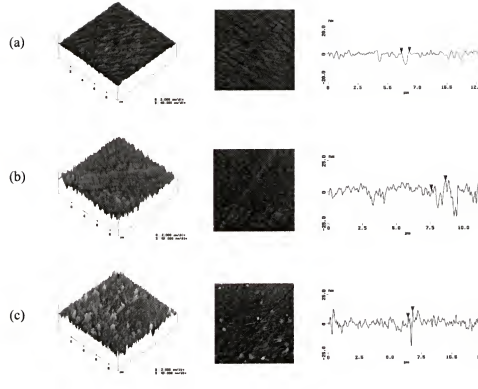

Figure 8-12 The surface roughness of the silica wafer polished in the 0.5 μm nonporous (a)SiO_2, (b) Al_2O_3, and (c)Si_3N_4 slurries of 5 wt.% loading at pH 3.

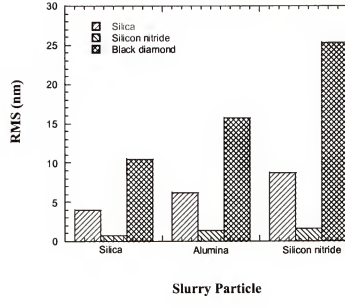

Figure 8-13 The surface roughness of the silica wafer polished in the 0.5 μm nonporous (a)SiO_2, (b) Al_2O_3, and (c)Si_3N_4 slurries of 5 wt.% loading at pH 3.

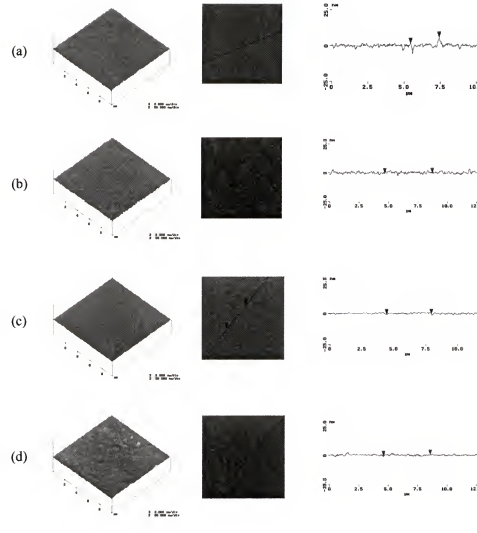

Figure 8-14 The surface roughness of the silica wafer polished in the 0.2 μm nonporous silica slurry of 5 wt.% loading at pH 3 as a function of the surface porosity of the particle: (a)2.8%, (b) 13.9%, and (c)36.1%, and (d) 57.6%.

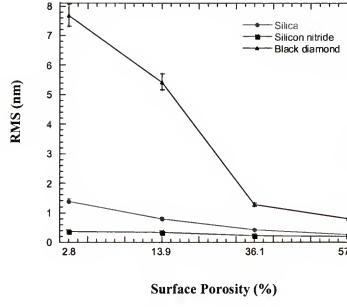

Figure 8-15 The surface roughness of the silica wafer polished in the 0.2 μm nonporous silica slurry of 5 wt.% loading at pH 3 as a function of the surface porosity of the particle: (a)2.8%, (b) 13.9%, and (c)36.1%, and (d) 57.6%.

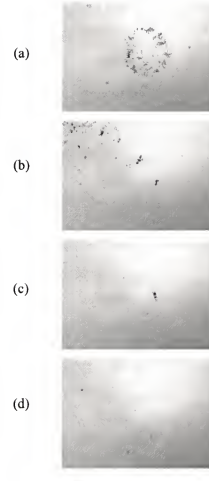

Figure 8-16 The residual particles of the silica wafer surfaces polished in the 0.2 μm nonporous silica slurry of 5 wt.% loading at pH 3 as a function of the surface porosity of the particle: (a)2.8%, (b) 13.9%, and (c)36.1%, and (d) 57.6%.

CHAPTER 9
CONCLUSION

The spherical silica particles with a very narrow particle size distribution have been synthesized by the hydrolysis reaction of TEOS in ethanol containing water and ammonia. The size and size distribution of silica nanoparticles were dependent of the ratios of the concentrations between water, ammonia, and TEOS. Spherical nanosized powders could be prepared with a perfect spherical morphology and a very narrow particle size distribution. The microporosity of silica particles with various sizes from nano- to submicro-meter could be generated by adsorption of the glycerol after simple calcination. A simple calcination was sufficient to eliminate the organic porogen and created around 50-60 % microporosity neither altering particle morphology nor favoring silica particle agglomeration. It was found that the mean particle size and size distribution increase with increasing the porogen content. This method was suitable for the preparation of uniform microporous silica particles with a very narrow particle size distribution and allowed the possibility of controlling the intraparticle porosity by varying the porogen content during the synthesis. Using glycerol, a larger mean particle size has been obtained as compared with silica spheres synthesized in the absence of any additive, indicating that particle growth is favored in this system. The particle formation was found to proceed via a particle aggregation process. In this study, we were able to tailor particle size and porosity of silica particles by playing with the chemistry of the reaction and adding chemical additives, respectively.

The optical properties of nanoporous silica particles were characterized by measuring the refractive index and dielectric constant of silica particles with a variation of the surface porosity and TEOS wafer using spectroscopic ellipsometry as a function of wavelength to be used to calculate the Hamaker constant of each sample. Tabor-Winterton approximation was employed for the Hamaker constant calculation with an assumption of two different bodies interacting in an aqueous medium of water followed by the calculation of total DLVO interaction energy and van der Waals force between silica sphere surface and TEOS flat surface using the previous result of the Hamaker constant calculated. The surface porosity of silica particles influences the refractive index and dielectric constant resulting in change of the Hamaker constant. Both the refractive index and dielectric constant of silica particles decrease with increasing the surface porosity due to the change in surface roughness. The lower Hamaker constant also was calculated in highly porous silica particles due to lower particle density compared to nonporous one. DLVO interaction energy and force between silica sphere and TEOS were obtained from the calculation of the Hamaker constant. As expected, the van der Waals attractive force decreases with increasing the surface porosity of silica particles indicating that lower adhesion force between porous abrasive slurry particles and wafer surface may be expected to be observed in CMP performance leading to lower surface defects.

The silica-silica surface and the silicon nitride-silica surface interactions were investigated using a single silica particle probe and silicon nitride tip interacting with the porous silica particle pellet surface surrounded by the cold mounting polymeric material by AFM surface force measurements. No potential barrier or "jump-in" on the attracting curves was observed in the silica-silica interaction indicating that the repulsive energy is

predominant when the silica particle probe approaches the silica flat surface for all cases of the samples. However, the degree of the repulsive force on the approaching curves depends on the surface porosity of silica particles embedded on the flat substrate surface. It means that the surface porosity influences the silica-silica interaction due to lower Hamaker constant of highly porous silica particles leading to lower van der Waals attraction force, even though it is not significant. In the retracting curves of silica-silica interaction the adhesion force was observed when the silica probe moves away from the substrate surface at short separation distance. This adhesion force was decreased with increasing the surface porosity of silica particles existing on the substrate surface and finally vanished at highly porous silica sample (57%) indicating that the van der Waals force becomes weaker as the surface porosity increases, while the repulsive force between silica-silica interaction becomes stronger depending on the surface porosity of the sample.

On the other hand, the "jump-in" on the approaching curves was observed in the silicon nitride-silica interaction for all samples indicating the strong van der Waals force was caused when the silicon nitride tip approaches the silica substrate surface since they are opposite charges each other. The reason that the position of "jump-in" is not regular by each sample is because the silica substrate surfaces, which is composed of porous silica particles, are not smooth. The surface porosity of silica particles does not affect significantly the interaction force between silicon nitride and silica except for a highly porous silica case, which does not show any attraction force. In the retracting curves of silicon nitride-silica interaction very strong adhesion forces were observed depending on the surface porosity of silica particles. The higher the surface porosity, the lower the adhesion force between silicon nitride and silica surfaces.

The zeta-potentials of slurry particles and wafer surfaces were measured to

calculate the DLVO total interaction energy between them at various pHs. Instead of the Debye-Huckel low potential approximation, Overbeek's approximation was applied to the calculation. The electrostatic force was calculated for the combined systems of two silica particles and three wafer surfaces to investigate the effects of the zeta-potential and surface porosity of slurry particles. The interaction force between slurry abrasives and wafer surface during CMP may be mainly determined by van der Waals attractive and electrostatic repulsive force. Even though van der Waals force is inherent in materials, the electrostatic forces are strongly dependent of the surface potentials which are strongly dependent of the pH of solutions. The surface potentials of particles and wafer surfaces in an aqueous solution can be expressed in terms of zeta-potentials. If the sign of potentials of two interacting surfaces are the same, there is a net repulsion of two surfaces and vice versa depending on the magnitude of van der Waals force. DLVO theory can be used to calculate the interaction forces between the slurry particle and the wafer surface to be polished. The interaction forces between the particles and wafer surfaces could provide important information on the stability of slurry and the degree of particle contamination on the surfaces after CMP.

The nanoindentation measurements of nanoporous silica particles with various surface porosities but almost same particle size of 200 nm were carried out to investigate the effect of the surface porosity on the mechanical properties such as the hardness and elastic modulus of the particles. The porous silica particles were mounted using a cold mounting polymer material since the sintering and pressing particles can alternate several properties of the particles. The analyzing the load-displacement curves obtained this experiment provided several information about the mechanical properties of silica particles. The contact depth was proportional to the surface porosity and the applied load.

The deviation of the contact depth became larger in highly porous silica particles due to a significant elastic behavior in high porosity ranges. It implies that the porous silica particle has lower density and pore structure resulting in lower contact area and hardness. To calculate the hardness of nanoporous silica particles the contact area was measured from the micrographs of silica particles indented. The contact area increased linearly with the surface porosity in lower porosity ranges but maintained constant values in high porosity ranges, where results in very low and uniform hardness of the particle. The deviation of the hardness of particles between different loads depends on the surface porosity but leads to very uniform values of hardness at high porosity ranges.

The CMP experiments of three different wafers, such as silica, silicon nitride, and black diamond, were performed in the various slurry systems, which include nonporous silica particle varying the particle size, porous silica particles with various surface porosities, and different types of particles, such as alumina and silicon nitride, in terms of the particle shape and hardness. The large particles showed the higher polishing rate resulting in large number of the surface scratch and higher RMS value conducted by the optical microscopy and AFM, respectively. The variation of the removal rates between three diffrent wafer surfaces implied that the type of raction between the slurry particles and wafer surface dominates the ploishing rate leading to the variation of the surface scratches and roughness between them. Lower chemical reaction but very hard slurry particles reacting with a hard wafer surface resulted in lower removal rate and the very serious surface scratches. The surface porosity of the slurry particles has proven that it is able to reduce the surface defects in terms of the surface scratch and residual slurry particles of wafer surface polished in higly porous silica based slurry system since the hardness of silica particle decreases with increasing the surface porosity and the van der

Waals attraction force between silica wafer and silica particles becomes smaller as the surface porosity of the slurry particles increases, which influences significantly both removal rate and surface quality of CMP wafers. The inspection of the surface defects of CMP wafer polished is very complicated and it may cause some errors even with very accurate instruments since many reasons, which cause the surface defects during CMP process, are unknown yet. However, the simple experiments conducted in this work indicated that the porous silica particles can enhance the surface quality by reducing surface defects.

APPENDIX
EFFECTS OF SURFACE POROSITY OF SILICON DIOXIDE PARTICLE ON OXIDE COATING PROCESS

Porous silica particle is a promising material with versatile potential applications in CMP process by controlling the particle size and surface porosity. It also can be applied for several coating systems for other purposes depending on the applications. Generally, it is known that the porous particles provide larger surface area and lower particle density compared to nonporous one resulting in higher sensitivity of chemical reaction alternating the surface charge or energy.

We have found that the porous silica particles are good candidate for oxide material coating process as the core particle providing large surface contact area with other materials to be coated. The ceria particles could be coated onto highly porous silica particles more than nonporous silica particles due to higher surface reactivity between them. Figure A.1 shows the zeta-potentials of 36 % porous silica particles, ceria particles, and ceria coated silica particles as a function of pH. The isoelectric points of silica and ceria particles are around 2 and close 7, respectively, while that of ceria coated silica particles is around 4.5 resulting from the chemical reaction between two different surface charges. Figure A.2 shows the evolution of the coating process of ceria particles onto porous silica particle varied by the type and concentration of the precursors and pH. By adjusting coating process parameters it was able to control the thickness of coated layer as shown in Figure A.3, which illustrates the XPS results of ceria coated silica

particles with $Ce(NO_3)_36H_2O$ system resulting in thick coated layer and $Ce(SO_4)_34H_2O$ system resulting in thin coated layer. Generally, the coating process of oxide particles is varied by the type and characteristics of both core particle and oxide particles to be coated and other environmental parameters. Figure A.4 shows TEM micrographs of coated oxide materials of MnO_2/SiO_2, TiO_2/SiO_2, and SiO_2/Al_2O_3.

(a)

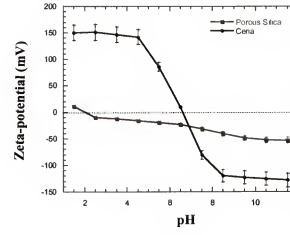

(b)

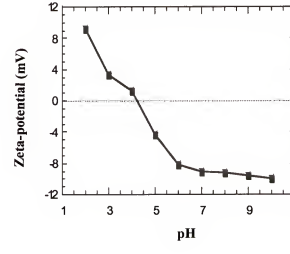

Figure A-1. Zeta-potentials of 200 nm porous silica of 36% and 20 nm ceria particles (a), and of ceria coated silica particle (b).

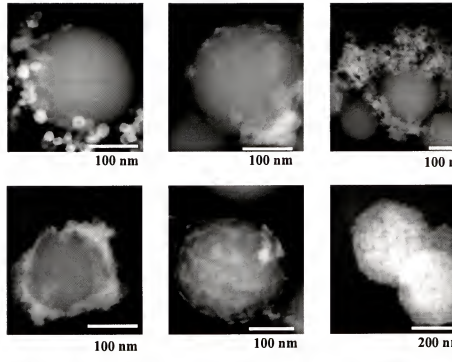

Figure A-2. Evolution of the coating process of ceria particles onto porous silica particle varied by the type and concentration of the precursors and pH.

(a)

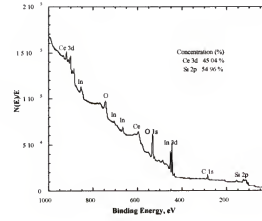

(b)

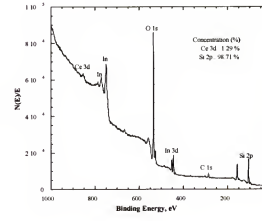

Figure A-3. XPS of ceria coated silica particles with (a) $Ce(NO_3)_36H_2O$ System resulting in thick coated layer and (b) $Ce(SO_4)_34H_2O$ System resulting in thin coated layer.

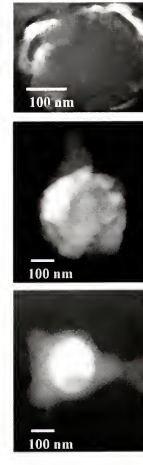

Figure A-4. TEM micrographs of coated materials: (a) MnO_2/SiO_2, (b) TiO_2/SiO_2, and (c) SiO_2/Al_2O_3.

REFERENCES

Ada67 Adamson, A. W., *Physical Chemistry of Surfaces*, 2nd Ed., Interscience Publishers, New York, 1967.

Ame00 America, W. G, Srinivasan R., and Babu, S. V., *Mat. Res. Soc. Proc.*, 566, (2000).

Arr99 Arriagada, F. J., and Osseo-Asare, K., *Journal of colloid and Interface Science* 211, 210 (1999).

Atk86 Atkins, P. W., *Physical Chemistry*, 3rd Ed., Oxford Univ. Press, New York, 1986.

Bae76 Baes, E. A., and Mesmer, H. K., *The Hydrolysis of Cations*, John Wiley & Sons, New York, 1976.

Bec92 Beck, J.S., Vartuli, J.C., Roth, W.J., Leonowicz, M.E., Kresge, C.T., Schmitt, K.D.,Chu, C.T.-W., Olson, D.H., Sheppard, E.W., McCullen, S.B., Higgins, J.B., and Schlenker, J.L., *J. Am. Chem. Soc.*, 114(27), 10834-10843 (1992).

Ber97 Bergstrom, L., *Advances in colloid and Interface Science* 70, 125 (1997).

Bha00 Bhashan, B., *Hand Book of Micro/Nano Tribology*, 2dn Ed., CRC Press, New York, 2000

Bie99 Bielmann, M., Mahajan, U. and Singh, R. K., Shar, D. O. and Palla, B. J., *Electrochem. Solid-State Lett.* 2, 148 (1999)

Bla92 Van Blaaderen, A., Van Geest, J., and Vrij, A., *J. Colloid Interface Sci.*, 154, 481-501 (1992).

Bog88 Bogush, G.H., and Zukoski, C.F., *Ultrastructure Processing of Advanced Ceramics*, Wiley, New York, 1988, p. 477.

Bog91a Bogush, G.H., and Zukoski, C.F., *J. Colloid Interface Sci.*, 142, 1-18 (1991).

Bog91b Bogush, G.H., and Zukoski, C.F., *J. Colloid Interface Sci.*, 142, 19-34 (1991).

Bon00 Boning, D., Lee, B, Tugbawa, T, and Smith, T., *Mat. Res. Soc. Proc.*, 566, (2000).

Bou98 Bourgeat-Lami, E., and Lang, J., *J.Colloid Interface Sci.*, 197, 293-308 (1998).

Bri67 Brixner, B., *Journal of The Optical Society of America,* 57, 674 (1967).

Bri90 Brinker, C. J., and Scherer, G. W., *Sol-Gel Science: The Physics and Chemistry of Sol-Gel Processing*, Harcourt Brace Jovanovich, Boston, 1990.

Bro81 Brown, N. J., Baker, P.C., Maney, R. T., *Proc. SPIE* 306 (42) (1981)

Büc98 Büchel, G., Grün, M., Unger, K., Matsumoto, A., and Tsutsumi, K., *Supramol. Sci.*, 5, 253-259 (1998).

Cha85 Chaudhury, M. K., and Good, R. J., *Langmur* 1, 673 (1985).

Cha87 Chandar, P., Somasundaran, P., and Turro, N.J., *J. Coll. Interface Sci.* 117, 31 (1987)

Chi77 Chikazawa, M., and Nakajima, W., J. *Res. Assoc. Powder Technol.* Jpn., 14, 19 (1977).

Cle93 Cleveland, J. P., Manne, S., Bocek, D., and Hansma, P. K., *Review of Scientific Instruments* 64, 403 (1993).

Cop00 Copperta, J., Rogers, C., Racz, L., Philipossian, A. and Kaufman, F. B., *J. Electrochem. Soc.* 147, 1903 (2000).

Dej96 Dejule, D., *Semiconductor International* 19, 88, (1996).

Der41 Derjaguin, B. V., and Landar, L. D., *Acta Phys. Chim.*, USSR., 14, 633, (1941).

Dru96 Drummond, C. J., Georgaklis, G., and Chan, D. Y. C., *Langmur* 12, 2617 (1996).

Duc91 Ducker, W. A., Senden, T. J., and Pashley, R. M., *Nature* 353, 239 (1991).

Dzy61 Dzyaloshinskii, I. E., Lifshitz, E. M., and Pitaevskii, L. P., *Advances in Physics* 10, 165 (1961).

Els83 Elson, J. M., and Rahn, J. P., *Applied optics* 22, (1983).

Esu98 Esumi, K., Iitaka, M., and Koide, Y., *J. Coll. Interface Sci.* 208, 178 (1998)

Fan01 Fan, H., Swol, F, V., and Brinker, C. J., *Journal of Non-Crystalline solids* 285, 71 (2001).

Fle86 Fleming, B.A., *J. Colloid Interface Sci.*, 110, 40-64 (1986).

Fro99 Froberg, J. C., Rojas, O. J., and Claesson, P. M., *International Journal of Mineral Processing* 56, 1 (199).

Fur99 Fury, M., *Solid State Technol..*, 42 (7) (1999).

Gee89 Gee, M. L., Healy, T. W., and White, L. R., *Journal of Colloid and Interface Science* 131, 18 (1989).

Got97 Gotoh, K., Iinoya, K., and Higashitani, K, *Powder Technology Handbook*, 2nd Ed., Marcel Dekker, New York, 1997.

Ham37 Hamaker, H. C., *Physica* 4, 1058 (1937).

Hea00 Heaton, M., and Ge, L., *MICRO* 18, 2 (2000).

Hie97 Hiemez, P.C., and Rajagopalan, R., *Principles of Colloid and Surface Chemistry*, Marcel Dekker, Inc., New York, 1997.

Hol00 Holgado, M., and Meseguer, F., *Journal of Colloid and Interface Science* 229, 6, (2000).

Hor90 Horn, R. G., *Journal of The American Ceramic Society* 73, 1117 (1990).

Hou80 Hough, D. B., and White, L. R., *Advances in Colloid and Interface Science* 14, 3 (1980).

Hsu88 Hse, W. P., Ronnquist, L., and Matijevic, E., *Langmuir* 4, 31, (1988).

Isr97 Israelachvili, J. N., *Intermolecular and Surface Forces*, 2nd Ed., Academic Press, London, 1997.

Jai96 Jairath, R., Pant, A., and Mallon, T., *Solid State Technology* 39, (1996).

Jel92 Jelinek, L., Dong, P., Rojas-Pazos, C., Taïbi, H., and sz. Kováts, E., *Langmuir* 8(9), 2152-2164 (1992).

Jel94 Jelinek, L., and sz. Kováts, E., *Langmuir* 10(11), 4225-4231 (1994).

Kel98 Kelsall, A., *Glass Technol.*, 39(1),6-9 (1998).

Kim90 Kim, S., and Zukoski, C.F., *J. Colloid Interface Sci.*, 139, 198-212 (1990).

Kim00 Kim, K. H., and Hah, S. R., *Mat. Res. Soc. Proc.*, 566, (2000).

Kol56 Kolbe, G., *Das komplexchemische Verhalten der Kieselsäure*, Ph.D. thesis, Jena,Germany, (1956).

Kre92 Kresge, C.T., Leonowicz, M.E., Roth, W.J., Vartuli, J.C., and Beck, J.S., *Nature*, 359, 710-712 (1992).

Laa01 Laarz, E., and Berstrom, L., *Journal of American Ceramic Society,* 84, 1675, (2001).

Lan92 Landis, H., Burke, P., Cote, W., Hill, W., Hoffman, C., Kaanta, C., Koburger, C., Lange, W. and Luce, S., *Thin Solid Films* 220, 1 (1992)

Lar96 Larios, J. M, and Ravkin, M. A., *Semiconductor International* 19, 121, (1996).

Lev98 Levine, S., Bowen, B.D., and Partridge, S.J.,*Colloids Surf.*, **38**, 325-343 (198 9)

Lie95 Liebert, L. D., and Prieve, D. C., *Biophysical Journal* 69, 19 (1995).

Lif56 Lifshitz, E. M., *Soviet Physics JETP* 2, 73 (1956).

Lou94 Louder, D. R., and Parkinson, B. A., *Analytical Chemistry* 66, 84R (1994).

Mah76 Mahanty, J., and Ninham, B. W., *Dispersion Forces*, Academic Press, London, 1976.

Mai01 G. Maier, *Prog. Polym. Sci.* 26, 3 (2001)

Mal65 Malitson, I. H., *Journal of The Optical Society of America* 55, 1205 (1965).

Mar80 Mark, H. F., Othmer, D. F., Overberger, C. G., Seaborg, G. T., *Encyclopedia of Chemical Technology*, Wiley, New York, 1980.

Mat81 Matijevic, E., *Acc. Chem. Res.*, 14, 22-29 (1981).

Mat91 Matsoukas, T., and Gulari, E., *J. Colloid Interface Sci.*, 145(2), 557-562 (1991).

Mer50 La Mer, V.K., and Dinegar, R.H., J. *Am. Ceram. Soc.*, 72, 4847 (1950).

Mer52 La Mer, V.K., *Ind. Eng. Chem.*, 44(6), 1270- 1277 (1952).

Meu97 Meurk, A., Luckham, P. F., and Bergstrom, L., *Langmur* 13, 3896 (1997).

Mil96 Milling, A., Mulvaney, P., and Larson, L., *Journal of Colloid and Interface Science* 180, 460 (1996).

Mur96 Murarka, *S., Solid State Technol..*, 39(3), 83 (1996)

Mur00 S.P. Murarka, I.V. Verner, R.J. Gutmann, *Copper-Fundamental Mechanisms for Microelectronic Applications*, John Wiley & Sons, NY 2000

Mur00a Muraka, S., *Mat. Res. Soc. Symp. Proc.*, 566, (2000).

Mye99 Myers, D., *Surfaces, Interfaces, and Colloids*, 2nd Ed., John Wiley & Sons, New York, 1999.

Myk92 Mykura, H., and Mykura, N., *Composites Science and Technology* 92, 266 (1992).

Old94 Oldham, K. B., Myland, J. C., *Fundamentals of Electrochemical Science*, Academic Press, New York, 1994.

Oli92 Oliver, W. C., and Pharr, G. M., *Journal of Materials Research* 7, 1564, (1992).

Oli00 Oliver, M. R., *Mat. Res. Soc. Symp. Proc.*,566, (2000).

Ono01 Ono, M., and Yoshii, K., *High Pressure Research*, 20, 307, (2001).

Ott98 Otterstedt, J. E., and Brandreth, D. A., *Small Particles Technology*, Plenum Press, New York, 1998.

Pal85 Palik, E. D., *Handbook of Optical constants of Solids*, Academic Press, Orlando, 1985.

Pal91 Palik, E. D., *Handbook of Optical constants of Soids II*, Academic Press, New York, 1991.

Pal00 Palla, B. J. and Shar, D. O., *J. Coll. Interface Sci.* 223, No1, (2000)

Par69 Parsegian, V. A., and Ninham, B. W., *Nature* 224, 12197 (1969).

Par00 Park, J. G, and Jeong, H. D., *Mat. Res. Soc. Symp. Proc.*, 566, (2000).

Pet98 Peter, L., *Semiconductor International*, Sep. (1998)

Pha92 Pharr, G. M, and Oliver, W. C., *Materials Research Bull.* 17, 28, (1992).

Plu00 Plummer, J. D., Deal, M. D., and Griffin, P. B., *Silicon VLSI Technology*, Prentice Hall, 2000.

Poa00 Poag, F., *MICRO* 18, 7 (2000).

Poi99 Poilane, C, and Delobelle, P., *Materials Science and Engineering A* 262, 101 (1999).

Pri87 Prieve, D. C., Luo, F., and Lanni, F., *Faraday Discussions* 83, 297 (1987).

Rav97 Ravkin, M. A., and Zhang, J. X., *Semiconductor International CMP-MIC, Proc.*, (1997).

Rus91 Russel, W.B., Saville, D.A., and Schowalter, W.R., *Colloidal Dispersions*, Oxford Univ. Press, Oxford, 1991.

Rya95 Ryan, J. G., Geffken, R. M., Poulin, N. R. and Gutmann, J. R., *CMP of Microelectronic Materials*, John Wiley and Sons Inc (1997)

Sen95 Senden, T. J., and Drummond, C. J., *Colloids and surfaces A: Physicochemical and Engineering Aspects* 94, 29 (1995).

Sha69 Shaw, D. J., *Electrophoresis*, Academic Press, New York, 1969.

Sho00 Shon-Roy, L., *Solid State Technol.* 43 (6) (2000).

Shi97 Shih, Y. S., and Wang, J. F., *ISMIC* 237, (19997).

Soh00 Sohn, I. S., Moudgil, B. M., Singh, R. K., and Park, C. W., *Mat. Res. Soc. Symp. Proc.*, 566, (2000).

Ste97 Steigerwald, J. M., Murarka, S. P. and Gutmann, R. J., *CMP of Microelectronic Materials*, John Wiley and Sons Inc (1997)

Stö68 Stöber, W., Fink, A., and Bohn, E., *J. Colloid Interface Sci.*, 26, 62-69 (1968).

Sur99 Suresh, S., Nieh, T. G., and Choi, B. W., *Scripta Materialia,* 41, 951, (1999).

Tab77 Tabor, D., *J. Colloid Interf. Sci.* 58, 2 (1977).

Tom97 Tomozawa, M., *Solid State Technol.* 40(7), 170-17(1997).

Tom99 Tomlinson, W., and Lakhani, F., *SPIE*, 306, (1999).

Tsu99 Tsui, T. Y., and Pharr, G. M., *Journal of Materials Research*, 14, 1, (1999).

Vac98 Vacassy, R., Scholz, S.M., Dutta, J., Plummer, C.J.G., Houriet, R., and Hofmann, H., *J. Am. Ceram. Soc.*, 81(10), 2699-2705 (1998).

Vac00 Vacassy, R., Flatt, R. J., Hofmann, H., Choi, K. S. and Singh, R. K., *J. Colloid Interface Sci.* 227, 302-315 (2000).

Vel98 Velv, O. D., Jede, T. A., and Lenhoff, A. M., *Nanostructured Materials, Proc.* 203, (1998).

Ver48 Verwey, E. J., and Overbeek, J. Th. G., *Elsevier*, Amsterdam, (1948).

Zha99 Zhang, C. J., Jin, J., and Wang, H. P., *Journal of Dispersion Science and Technology* 20, 1485 (1999).

Zik97 Zika, S., and Bains, G.,*KLA Yield Management Seminar*, Geneva, Switzerland, April, (1997).

BIOGRAPHICAL SKETCH

Kyo-Se Choi was born on the 5th day of December, 1969, in Seosan, Korea. After completing his primary education in Seosan, he attended the Department of Materials Science and Engineering at Chungnam National University, Taejeon, Korea, where he received his Bachelor of Science degree in March, 1992. He entered graduate school at the University of Florida in September, 1998. He received his Master of Science degree in August, 2001.

I certify that I have read this study and that in my opinion it conforms to acceptable standards of scholarly presentation and is fully adequate, in scope and quality, as a dissertation for the degree of Doctor of Philosophy.

Rajiv K. Singh, Chair
Professor of Materials
Science and Engineering

I certify that I have read this study and that in my opinion it conforms to acceptable standards of scholarly presentation and is fully adequate, in scope and quality, as a dissertation for the degree of Doctor of Philosophy.

Abbas A. Zaman
Associate Professor of Materials
Science and Engineering

I certify that I have read this study and that in my opinion it conforms to acceptable standards of scholarly presentation and is fully adequate, in scope and quality, as a dissertation for the degree of Doctor of Philosophy.

Hassan El-Shall
Associate Professor of Materials
Science and Engineering

I certify that I have read this study and that in my opinion it conforms to acceptable standards of scholarly presentation and is fully adequate, in scope and quality, as a dissertation for the degree of Doctor of Philosophy.

Stephen J. Pearton
Professor of Materials
Science and Engineering

I certify that I have read this study and that in my opinion it conforms to acceptable standards of scholarly presentation and is fully adequate, in scope and quality, as a dissertation for the degree of Doctor of Philosophy.

Dinesh O. Shah
Professor of Chemical Engineering

This dissertation was submitted to the Graduate Faculty of the College of Engineering and to the Graduate School and was accepted as partial fulfillment of the requirements for the degree of Doctor of Philosophy.

December 2002

Pramod P. Khargonekar
Dean, College of Engineering

Winfred M. Phillips
Dean, Graduate School